ANALYSIS AND MODELING OF MACHINING AND SURFACE INTEGRITY CHARACTERISTICS UNDER VARIOUS TURNING ENVIRONMENTS

by

Mahshad JAVIDIKIA

MANUSCRIPT-BASED THESIS PRESENTED TO ÉCOLE DE TECHNOLOGIE SUPÉRIEURE IN PARTIAL FULFILLMENT FOR THE DEGREE OF DOCTOR OF PHILOSOPHY
Ph.D.

MONTRÉAL, NOVEMBER 23, 2020

ÉCOLE DE TECHNOLOGIE SUPÉRIEURE
UNIVERSITÉ DU QUÉBEC

BOARD OF EXAMINERS

THIS THESIS HAS BEEN EVALUATED

BY THE FOLLOWING BOARD OF EXAMINERS

Prof. Victor Songmene, Thesis Supervisor
Department of Mechanical Engineering at École de technologie supérieure

Prof. Mohammad Jahazi, Thesis Co-Supervisor
Department of Mechanical Engineering at École de technologie supérieure

Prof. Michel Rioux, President of the Board of Examiners
Department of Automated Production at École de technologie supérieure

Prof. Zhaoheng Liu, Member of the jury
Department of Mechanical Engineering at École de technologie supérieure

Prof. Marek Balazinski, External Evaluator
Department of Mechanical Engineering at École Polytechnique Montréal

THIS THESIS WAS PRESENTED AND DEFENDED

IN THE PRESENCE OF A BOARD OF EXAMINERS AND PUBLIC

ON NOVEMBER 16, 2020

AT ÉCOLE DE TECHNOLOGIE SUPÉRIEURE

ACKNOWLEDGMENT

First, I would like to thank my supervisor, Professor Victor Songmene, for his encouragement, valuable guidance, and continuous technical and financial supports throughout my research at École de Technologie Supérieure. It has been a great honor for me to work as his doctoral student for several years. In addition, my sincere gratitude and deep appreciation to my Co-supervisor, Professor Mohammad Jahazi, for his technical support during my Ph.D. project. Conducting research under their supervisions was an invaluable experience for me.

Moreover, I would like to extend my appreciation to my thesis committee members, Professors Michel Rioux, Zhaoheng Liu, and Marek Balazinski for having accepted to evaluate my thesis and for providing useful suggestions and constructive comments.

I am also grateful to Dr. Morteza Sadeghifar for all priceless comments and discussions, helpful guidance, indispensable advice, technical help, and support during my PhD project.

I would like to thank Aluminum Research Centre (REGAL) for financial support since I have started my Ph.D.

Finally, and most importantly, special thanks to my family. Words cannot express how grateful I am to my beloved mother, father, and sister for their affection, endless love and encouragement. They have always been incenting me to strive towards my goal and been supporting me, unconditionally and continuously, throughout my life.

Analyse et modélisation des caractéristiques de l'usinage et de l'intégrité de surface en fonction de l'environnement du tournage

Mahshad JAVIDIKIA

RÉSUMÉ

Les pièces d'avion et aérospatiales sont souvent produites en alliages d'aluminium car ces alliages possèdent des résistances spécifiques et formabilités convenables ainsi que d'excellentes résistances à la corrosion. Les caractéristiques de l'intégrité de surface de ces alliages, dont la rugosité de surface et les contraintes résiduelles sont fonction des paramètres d'usinage, dont la température et les efforts transmis aux pièces lors des opérations d'usinage. Les fluides d'usinage apportent une lubrification et un refroidissement nécessaires pour la qualité des pièces produites. L'utilisation d'un fluide peut améliorer la résistance en fatigue et la résistance à la corrosion.

Le but de cette étude était de développer des modèles par éléments finis (EF) en deux et en trois dimensions afin de simuler l'usinage par tournage de l'alliage AA6061-T6. Ainsi, il a été possible de prévoir les contraintes résiduelles pour plusieurs environnements. Cette étude avait aussi comme objectif l'analyse d'une campagne expérimentale, ainsi qu'une modélisation prédictive par régression et une optimisation multicritère des contraintes résiduelles et des paramètres de rugosité, et ce pour une variété d'environnements de tournage.

Cette étude a été divisée en trois phases consécutives.

D'abord, un modèle par éléments finis en deux dimensions a été développé et validé expérimentalement pour plusieurs paramètres d'usinage. Le modèle a servi à simuler les interactions entre le rayon du bord de coupe de l'outil et la vitesse de coupe, l'avance et l'angle de coupe. Ainsi, l'influence de la géométrie de l'outil et des paramètres de coupe sur les efforts de coupe, la température, et l'épaisseur du copeau a été évaluée pour le tournage de l'alliage AA6061-T6. Ensuite, les résultats de l'usinage conventionnel ont été comparés avec les résultats de l'usinage à grande vitesse (UGV).

Deuxièmement, des essais de tournage ont été complétés selon un plan d'expériences composite centré pour trois environnements d'usinage. Les paramètres d'usinage au meilleur rendement ont été identifiés par analyse de variance (ANOVA) pour chaque environnement. L'importance de la vitesse de coupe, de l'avance, et de la profondeur de coupe sur la rugosité de surface et les contraintes résiduelles a été étudiée pour l'usinage à sec (DRY), à lubrification à quantité minimale (MQL), et lubrifié (WET). La méthode des surfaces de réponse a été appliquée pour prévoir des modèles ajustés efficaces pour chaque environnement de tournage pour la rugosité de surface, la hauteur des sommets par rapport aux vallées, les contraintes résiduelles axiales en surface, et les contraintes résiduelles circonférentielles en surface. Par la suite, à l'aide des modèles ajustés prédictifs, une étude multi-performance a été complétée afin

d'identifier les paramètres de tournage optimaux pour l'intégrité de surface en tournage à basse vitesse (LST) et à grande vitesse (HST) de l'alliage AA6061-T6 pour chaque environnement.

De plus, un modèle par éléments finis en trois dimensions a été développé pour simuler et prévoir la température d'usinage, les efforts, et les contraintes résiduelles axiales pour plusieurs environnements et paramètres d'usinage. Les environnements considérés étaient les modes d'usinage à sec, à MQL et lubrifié. Les paramètres d'usinage considérés étaient les paramètres de coupe, dont la vitesse de coupe, l'avance, et la profondeur de coupe, et les paramètres géométriques de l'outil, dont le rayon du bord de coupe, l'angle de coupe secondaire, et l'angle de dépouille secondaire. Une attention particulière a été accordée à la simulation de contraintes résiduelles en tournage de l'alliage AA6061-T6 avec le logiciel DEFORM-3D^{TM}. Le modèle par EF à trois dimensions a été validé en comparant les efforts de coupe et les contraintes résiduelles axiales en surface avec les mesures expérimentales correspondantes. Les effets de la vitesse de coupe, l'avance, et la profondeur de coupe sur les contraintes résiduelles axiales ont été étudiés expérimentalement pour trois environnements de tournage. L'influence de la géométrie de l'outil de coupe, dont le rayon du bord de coupe, l'angle de coupe secondaire, et l'angle de dépouille secondaire a été étudié à l'aide du modèle par EF en trois dimensions pour le tournage en condition d'usinage lubrifié.

Les modèles ajustés issues de la modélisation par EF en deux et en trois dimensions sont capables de prévisions fiables pour des applications industrielles. Elles peuvent contribuer à l'amélioration et l'optimisation de l'usinage et de l'intégrité de surface pour plusieurs environnements de tournage et paramètres.

Mots clés : Environnements et paramètres de tournage ; Caractéristiques d'usinage ; Intégrité de surface ; Modèles FE 2D/3D ; Modèles ajustés ; Optimisation multicritère ; AA6061-T6.

Analysis and modeling of machining and surface integrity characteristics under various turning environments

Mahshad JAVIDIKIA

ABSTRACT

Aluminum alloys are widely used in aerospace components and aircraft and due to their high strength to weight ratio, good workability, and high resistance to corrosion. Surface integrity of Al alloys including surface roughness and residual stresses are dependent on machining characteristics including cutting temperature and machining forces in machining operations. Cutting fluids as coolant and/or lubrication can be utilized to affect the machining characteristics and possibly improve the part quality of components. This can increase fatigue and corrosion resistance of Al alloys.

This research study was aimed at developing 2D and 3D finite element models to simulate machining characteristics and predict residual stresses in turning of AA6061-T6 for various environments. Moreover, another objective of the study was to conduct an experimental analysis, predictive regression modeling, and multi-criteria optimization of residual stresses and surface roughness parameters under various turning environments.

This research work is divided into three consecutive phases.

First, a 2D finite element model was developed and experimentally validated for different machining parameters. The FE model was utilized to simulate the interactions between cutting edge radius and cutting speed, feed rate, and rake angle and investigate the influences of the above-mentioned tool geometry and cutting conditions on machining forces, cutting temperature, and chip thickness in orthogonal turning of AA6061-T6. Finally, the results of conventional machining (CM) and high speed machining (HSM) were compared.

Secondly, turning tests were conducted using a Design of Experiment (DoE) based on Central Composite Design (CCD) under the three turning environments. The most efficient turning parameters were determined for each environment using Analysis of Variance (ANOVA). The impact of turning parameters including cutting speed, feed rate and depth of cut was investigated under DRY, MQL, and WET modes and their effect on surface roughness and residual stresses were analyzed. Response Surface Method (RSM) was used to predict effective regression models for each turning environment for the average arithmetic surface roughness, the height peak from the valley, the axial surface residual stress, and the hoop surface residual stress. Then, using the predictive regression models, a multi-performance optimization study was carried out to identify optimal turning parameters in each environmental mode to improve surface integrity in Low Speed Turning (LST) and High Speed Turning (HST) of AA6061-T6.

Finally, a 3D finite element model was developed to simulate and predict machining temperature (MT), machining forces (MFs), and axial surface residual stress (ASRS) for various turning environments and parameters. Turning environments consist of DRY, MQL, and WET modes, and turning parameters include both cutting conditions and tool geometry such as cutting speed, feed rate, depth of cut, tool nose radius, side cutting edge angle (SCEA), back rake angle (BRA). Special attention was devoted to simulating residual stresses in turning of AA6061-T6 alloys using the DEFORM-3D^{TM} software. The 3D FE model was validated by comparing the predicted MFs and ASRS with the corresponding experimental measurements. The effect of cutting conditions including cutting speed, feed rate, depth of cut on axial residual stress was experimentally investigated for three turning environments and the influence of tool geometry consisting of tool nose radius, side cutting edge angle, and back rake angle was numerically studied using the 3D FE model of WET turning.

The 2D/3D finite element and regression models can be utilized as predictive reliable tools for industrial applications to improve and optimize machining and surface integrity characteristics for various turning environments and parameters.

Keywords: Turning Environments and Parameters; Machining Characteristics; Surface Integrity; 2D/3D FE Models; Regression Model; Multi-criteria Optimization; AA6061-T6.

TABLE OF CONTENTS

Page

LIST OF TABLES

Page

LIST OF FIGURES

Page

LIST OF ABBREVIATIONS

AA	Aluminum Alloy
ANOVA	Analysis of Variance
ASRS	Axial Surface Residual Stress
BRA	Back Rake Angle
BC	Boundary Condition
BBD	Box-Behnken Design
CCD	Central Composite Design
CF	Constraint Function
CM	Conventional Machining
DoE	Design of Experiment
E	Eulerian
FE	Finite Element
FEM	Finite Element Method
GA	Genetic Algorithm
GRA	Grey Relational Analysis
HSM	High Speed Machining
HSRS	Hoop Surface Residual Stress
HSS	High Speed Steel
HST	High Speed Turning
J-C	Johnson-Cook
LST	Low Speed Turning
MFs	Machining Forces
MQC	Minimum Quantity Coolant
MQL	Minimum Quantity Lubrication
MRR	Material Removal Rate
MT	Machining Temperature

OF	Objective Function
OM	Orthogonal Machining
PCBN	Polycrystalline Cubic Boron Nitride
PCD	Polycrystalline Diamond
PL	pure Lagrangian
RQL	Reduced Quantity Lubricant
RS	Residual Stress
RSM	Response Surface Method
SCEA	Side Cutting Edge Angle
SEM	Scanning Electron Microscopy
SQP	Sequential Quadratic Programming
UL	updated Lagrangian
XRD	X-Ray Diffraction

LIST OF SYMBOLS

A	Initial yield strength in J-C model (MPa)
a_0 to a_9	Regression coefficients
B	Hardening modulus in J-C model (MPa)
b_0	Intercept
b_i, b_{ij}, and b_{ii}	Unknown regression coefficients
C	Strain rate sensitivity coefficient in J-C model
C_d	Damping matrix ($N.s/\mathrm{m}$)
C_T	Volumetric heat capacity matrix ($J/\ ^oC$)
c	Specific heat capacity ($J/kg\ ^oC$)
D	Depth of Cut (mm)
D_L	Lower bound of depth of cut (mm)
D_U	Upper bound of depth of cut (mm)
d	Lattice spacing of crystal planes (μm)
d_0	Lattice spacing of stress-free state of material (μm)
E	Young's modulus of elasticity (GPa)
F_c	Cutting force (N)
F_f	Feed force (N)
F_r	Radial force (N)
F_t	Thrust force (N)
f	Feed rate (mm/rev)
f_L	Lower bound of feed rate (mm/rev)
f_U	Upper bound of feed rate (mm/rev)
$f(X)$	Optimization response
$g_j(X)$	Optimization constraints
h	Convection heat transfer coefficient ($kW/(m^2°\mathrm{C})$)

h_{int}	Thermal conductance coefficient ($kW/(m^2$°C))
i	Number of independent variables
K_s	Stiffness matrix (Kg/s^2)
K_T	Thermal conduction matrix ($W/\ ^oC$)
k	Thermal conductivity ($W/m\ ^oC$); Number of parameters
l_p	Length of sticking region (mm)
l_c	Tool-chip contact length (mm)
M	Mass matrix (Kg)
m	Thermal softening coefficient in J-C model ; Shear friction factor
n	Hardening coefficient in J-C model ; Number of design points
p	Penalty parameter
$\dot{Q}_g$	Heat generation in machining process (W)
R_a	Arithmetic average surface roughness (μm)
R_{ext}	External force vector (N)
R_{int}	Internal force vector (N)
R_t	Maximum height of the profile (μm)
R^2	Coefficient of determination
r	Nose radius (mm)
r_β	Edge radius (mm)
T	Temperature (^oC)
T_a	Ambient temperature (^oC)
T_m	Melting temperature (^oC)
T_{room}	Room temperature (^oC)
T_{wp}	Workpiece temperature (^oC)
t	Time (s) ; Tool
t_c	Chip thickness (mm)
$\dot{T}$	Temperature rate ($^oC/s$)

U	Material displacement vector (m)
$\dot{U}$	Material velocity vector (m/s)
$\ddot{U}$	Material acceleration vector (m/s^2)
V	Cutting speed (m/min)
V_L	Lower bound of cutting speed (m/min)
V_U	Upper bound of cutting speed (m/min)
V_{ch}	Chip velocity along the tool-chip interface (m/min)
wp	Workpiece
X	Design matrix
y	True response
$\hat{y}_i$	Approximate response computed from RSM
$\bar{y}$	Average of true response
α	Thermal expansion coefficient $(1/\,^oC)$
α_0	Clearance angle (deg)
γ_0	Rake angle (deg)
ϵ	Experimental error
ε	Plastic strain ; error between true response and its approximation
$\dot{\varepsilon}$,$\dot{\varepsilon}_p$	Effective Plastic strain rate $(1/s)$
$\dot{\varepsilon}_0$	Reference plastic strain rate $(1/s)$
θ	Diffraction angle (deg)
θ_0	Diffraction angle of stress-free state of material (deg)
λ	Wavelength of X-Ray beams (μm)
μ	Coulomb friction coefficient
υ	Poisson's ratio
ρ	Density (kg/m^3)
$\bar{\sigma}$	Flow stress (MPa)
σ_a	Axial surface residual stress (MPa)

σ_h	Hoop surface residual stress (MPa)
σ_n	Normal compressive stress (MPa)
τ	Frictional shear stress at the tool-chip contact face (MPa)
τ_Y	Shear flow stress (MPa)

INTRODUCTION

In the following, a short description of the main terminologies used in the present thesis is provided below for clarification and minimize repetitions throughout the text:

0.1 Turning processes

In turning processes, a cutting insert with a single cutting nose is used to cut the material from a rotating sample to generate a cylindrical shape. In orthogonal turning, the tool cutting edge is perpendicular to cutting speed. Orthogonal cutting is a fundamental cutting process which can help to understand most machining operations such as milling, turning, and drilling (Sadeghifar, 2017). In turning processes, the cutting tool is three-dimensional and complex in terms of geometry. Hence, the two dimensional orthogonal turning is used to better display the mechanism of the machining process (Daoud, 2016).

0.2 High speed machining

High speed machining (HSM) is commonly used in manufacturing of aluminum components for the automotive and aeronautical industries due to its many merits over conventional machining (Markopoulos, 2012). HSM may provide the following advantages (Swift et Booker, 2013):

- Increased productivity, reduced lead time and machining costs;
- Increased machining accuracy;
- Reduced burr formation;
- Provided better chip disposal;
- Caused a higher stability in cutting;

0.3 Aluminum alloy 6061-T6

Aluminum alloy 6061 (AA6061) is one of the most widespread of the 6000-series aluminum alloys. It has high strength, good workability, and high resistance to corrosion. It is commonly used in aircraft and aerospace components. The T6 heat treatment is corresponding to a solution heat treatment and an artificial aging. The beneficial properties of T6 temper are obtained through the solution treatment process involving high temperature heating and rapid cooling of material, leading to a stronger material (Khan *et al.*, 2017).

0.4 Turning environment

Dry turning is frequently conducted due to the environmental and health regulations and reduction in the turning costs. However, it can produce high cutting temperature. In wet turning, cutting fluids are used during turning to reduce the generated temperature in both workpiece and tool and the friction at the tool-workpiece interface. However, cutting fluids with high flow rates not only are hazardous to the machinist health and the environment but also increase the turning costs. To avoid having all of these problems, another lubrication mode such as minimum quantity lubricant (MQL) is recommended. This method assists to have clean turning and eliminate the serious problems associated with traditional dry and wet turning operations. The most significant advantage of MQL system is that the lubricant with small flow rates is applied directly to the contact area, avoiding the thermal shocking of the cutting tool and increasing the surface integrity and quality. Figure 0.1 displays a turning operation using MQL system.

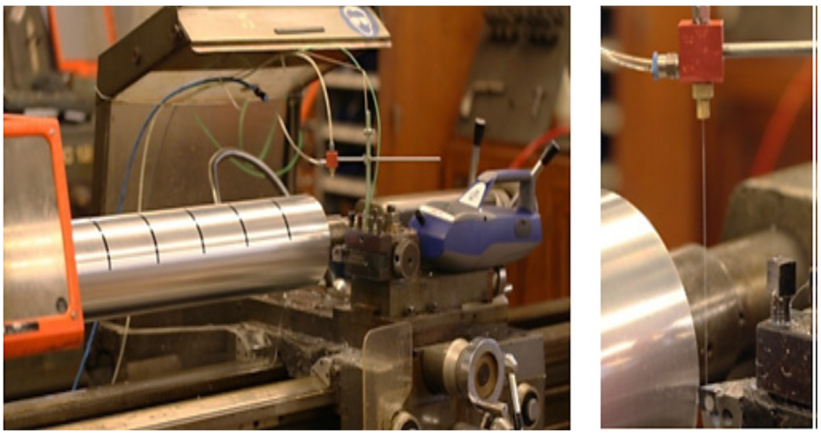

Figure 0.1 Applying MQL during a turning process (Jalali, 2013)

0.5 Machining and surface integrity characteristics

Metal turning generates high machining forces and temperatures, which lead to residual stresses. It is recognized that high temperature causes inaccuracies in the dimensions of the component. High machining forces increase the power consumption and cause an excessive deflection of the tool, and as a result, tool breakage. In addition, both high machining temperatures and forces result in large tool wear, and consequently, high surface roughness. Moreover, tensile residual stresses induced by turning processes have harmful influences on the samples due to opening tiny cracks, which subsequently decrease the resistance to fatigue and corrosion (Sadeghifar, 2017). Therefore, the analysis and optimization of machining characteristics including machining temperature and forces and surface integrity characteristics consisting of residual stresses and surface roughness parameters are required.

0.6 Finite element method

Numerical modeling of machining operations can be traced back to the early seventies when in-house finite element models were developed. With the advent of high-performance advanced computers and the development of new methods to model high strain rate and plastic deformations processes, turning operations can be simulated using the available software

packages such as DEFORM™, Abaqus®, and AdvantEdge™ to predict machining characteristics and surface integrity accurately. The developed FE models are reliable tools which enable manufacturers to predict machining and surface integrity characteristics while avoid conducting a large number of expensive, time-consuming experimental tests.

CHAPTER 1

PROBLEM STATEMENT, RESEARCH OBJECTIVES, AND THESIS OUTLINE

1.1 Problem statement and research objectives

Machining processes affect surface integrity including surface roughness and residual stresses of workpiece materials due to high temperature, large strain, and high strain rate induced by plastic deformation occurring during machining. Appropriate surface quality can be achieved by choosing the appropriate cutting condition, tool geometry parameters, and cutting environment. High temperature induced by frictional and plastic works during machining can affect surface integrity of workpiece materials. Hence, coolant and lubrication can be used to decrease the cutting temperature and friction and change the machining forces, and as a result, they may improve the part quality of machined components. This can lead to increasing fatigue and corrosion resistances of the workpiece material.

The overall objective of this research study is to improve surface quality generated by turning of AA6061-T6.

The specific objectives of the present research work are:

- ☑ To develop a 2D finite element model in order to analyze the effect of tool geometry including tool edge radius and rake angle and cutting conditions consisting of cutting speed and feed rate on machining characteristics including machining temperature, forces, and chip thickness.

- ☑ To experimentally study, model, and optimize turning conditions including cutting speed, feed rate, and depth of cut to improve surface integrity characteristics including surface roughness and residual stresses for various turning environments.

- ☑ To develop 3D finite element models in order to simulate the turning process, machining characteristics, and axial surface residual stresses for different turning environments and investigate the effect of tool geometry parameters consisting of tool nose radius, side cutting edge angle (SCEA), and back rake angle (BRA).

1.2 Thesis outline

This PhD thesis comprises six chapters which are briefly described below:

Chapter 1 explains the research objectives of the present thesis and outlines the thesis scope.

Chapter 2 summarizes the main published experimental and numerical research works on machining and surface integrity characteristics in turning processes, with a special focus on turning environment, machining characteristics, and surface integrity. Moreover, it briefly explains the finite element and optimization studies performed on surface integrity induced by turning processes.

Chapter 3 describes the methodology of experimental works and finite element modeling of machining characteristics and residual stresses.

Chapter 4 presents the first published journal article. This article aimed to analyze the interactions between cutting edge radius and cutting speed, feed rate and rake angle and investigate the influences of tool geometry and cutting conditions on machining forces, cutting temperature, and chip thickness in orthogonal turning of AA6061-T6. The results of conventional machining (CM) and high speed machining (HSM) were compared. A 2D finite element model was developed and experimentally validated for different machining parameters and was utilized to simulate the above interactions.

Chapter 5 presents the second submitted journal article. In this article, the influences of turning environments and parameters on surface integrity induced by turning of AA6061-T6

were studied. The impact of turning parameters including cutting speed, feed rate, and depth of cut was investigated under DRY, MQL, and WET modes and their effect on surface roughness and residual stresses were analyzed. Machining tests were conducted using a Design of Experiment (DoE) based on Central Composite Design (CCD) method under the three turning environments. The most efficient turning parameters were determined for each environment using Analysis of Variance (ANOVA). Response Surface Method (RSM) was used to predict effective regression models for each turning environment for the average arithmetic surface roughness, the height peak from the valley, the axial surface residual stress, and the hoop surface residual stress. Then, using the predictive regression models, a multi-performance optimization study was carried out to identify optimal turning parameters in each environmental mode for improved surface integrity in Low Speed Turning (LST) and High Speed Turning (HST) of AA6061-T6.

Finally, **Chapter 6** presents the third submitted journal article. In this article, the effects of turning environments and parameters on machining temperature (MT), machining forces (MFs), and axial surface residual stress (ASRS) induced by turning AA6061-T6 were investigated. Turning environments consisted of DRY, MQL, and WET modes, and turning parameters included both cutting conditions and tool geometry such as cutting speed, feed rate, depth of cut, tool nose radius, SCEA, and BRA. A 3D FE model was developed and validated by comparing the predicted MFs and ASRS with the corresponding experimental measurements. The 3D model was then utilized to simulate and predict MT, MFs, and ASRS for various turning environments and parameters.

The conclusions drawn from the present research work and some recommendations for future works in this field of study are provided at the end of this Ph.D. dissertation.

CHAPTER 2

LITERATURE REVIEW

2.1 Introduction

The first section (2.2) of this chapter provides a review of the surface integrity characteristics including surface roughness and residual stresses and relevant research works on the effects of turning environments and parameters on surface integrity. Section 2.3 describes a review of regression modeling and analysis and also optimization of surface integrity characteristics. The third section (2.4) presents an overview of finite element simulation and prediction of machining forces, temperature, chip thickness, and residual stresses. Finally, this chapter ends with the main gaps that have not yet covered and require further investigation.

2.2 Surface integrity

In manufacturing processes, the improvement of surface quality is one of the major issues of interest for customers. Surface integrity refers to surface roughness and residual stress, which are used for evaluating the quality of final products. Mostly, fatigue, creep, crack, and corrosion invariably start at the surface of components and affect the quality of the surface. Therefore, it is important to understand residual stresses and their tensile or compressive nature induced by machining processes (Ji *et al.*, 2014).

Machining processes affect surface integrity characteristics due to non-uniform changes between the bulk material and the machined surface layers (Touazine *et al.*, 2014). Therefore, it is required to obtain optimal turning parameters to improve surface integrity under various turning environments.

- Surface roughness

The surface finish includes the topography and defects of the component surface after machining. The surface roughness parameters are good indicators for the machined surface quality (Jomaa, 2015). On the other hand, Suraratchai *et al.* (2008) mentioned that surface roughness can generate local stress concentration. Moreover, experimental observations showed that fatigue cracks initiate from the surface (Javidi *et al.,* 2008). As a result, surface roughness is important for analyzing surface quality of machined components.

- Residual stress

Three important mechanisms lead to residual stresses formation (Daoud, 2016):

- Thermal shock: Thermal plastic deformation due to thermal gradient;
- Mechanical shock: Mechanical plastic deformation because of machining forces;
- Metallurgical change: Volume alternations from transformation of phases.

Mostly, thermal and mechanical deformation occur in metal cutting processes. Also, phase transformation does not occur in some metals including Al alloys.

2.2.1 Effects of turning environments and parameters on surface roughness

Although the effect of turning parameters on surface roughness was investigated by many researchers, a small number of research works studied and compared surface roughness parameters for different turning environments. Boulahmi (2015) conducted experimental research on the effect of feed rate and tool's nose radius on surface roughness parameters in turning AA2024-T4, AA6061-T6, and AA7075-T651 for various environments such as dry, MQL and wet. The results showed that MQL turning provided the smallest surface roughness parameters. However, the influences of cutting speed and depth of cut on surface roughness were not studied. Moreover, the optimization of overall surface integrity was not conducted.

Sreejith (2008) analyzed the influence of various environmental modes including dry, MQL, and wet, and cutting speed on surface roughness in turning of AA6061. As shown in Figure 2.1, for all the cutting speeds, applying coolant/lubricant improved surface roughness. Furthermore, average surface roughness rose at a larger cutting speed for all the environmental modes. The results also demonstrated that MQL mode was a good alternative to wet mode. However, the effects of high cutting speed, feed rate, and depth of cut on surface roughness were not studied under different turning environments. Moreover, residual stresses were not studied and optimized under different turning parameters and environments.

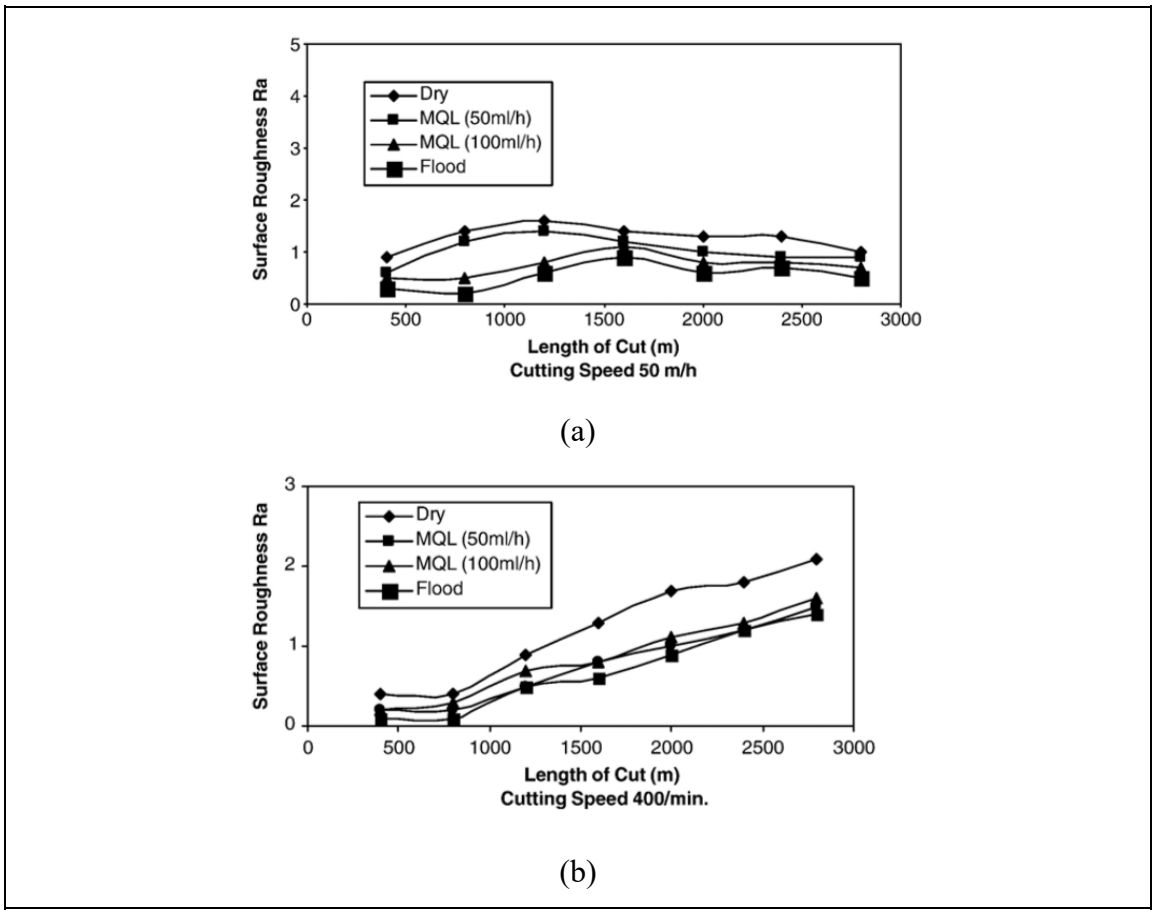

Figure 2.1 Variation of surface roughness with length of cut for different turning environments for the cutting speed of (a) 50 m/min and (b) 400 m/min (Sreejith, 2008)

Kouam *et al.* (2015) made a comparison of the impact of feed rate on surface roughness induced by turning AA7075-T6 for two turning environments of dry and MQL with two flow

rates. The results revealed that a lower flow rate of MQL could provide better surface roughness compared to larger flow rate of MQL and dry modes. In addition, the surface roughness parameters increased with feed rate for both modes (Figure 2.2). Çakır *et al.* (2016) analyzed the effect of cutting speed and feed rate on surface roughness induced by turning AA2024 and AA7075 for dry and MQL with different flow rates. They concluded that raising flow rate reduced surface roughness and positively affected surface quality, whereas increasing feed rate and cutting speed led surface roughness parameters to increase (Figure 2.3). However, the impact of wet mode on surface roughness was not investigated and compared and optimization was not carried out. Moreover, the impact of turning parameters and environments on residual stresses were not studied. Garcia *et al.* (2019) investigated the influence of cutting speed, feed rate, and depth of cut on surface roughness parameters in turning of AA6082-T6 under dry and reduced quantity lubricant (RQL) modes. They found that applying RQL mode and lower feed rate eliminated the waviness, which took placed in dry turning. It needs mentioning that the effect of wet mode was not studied and compared with dry and RQL modes. In addition, the effect of turning parameters and environments on residual stresses were not investigated and optimization of overall surface integrity was not performed.

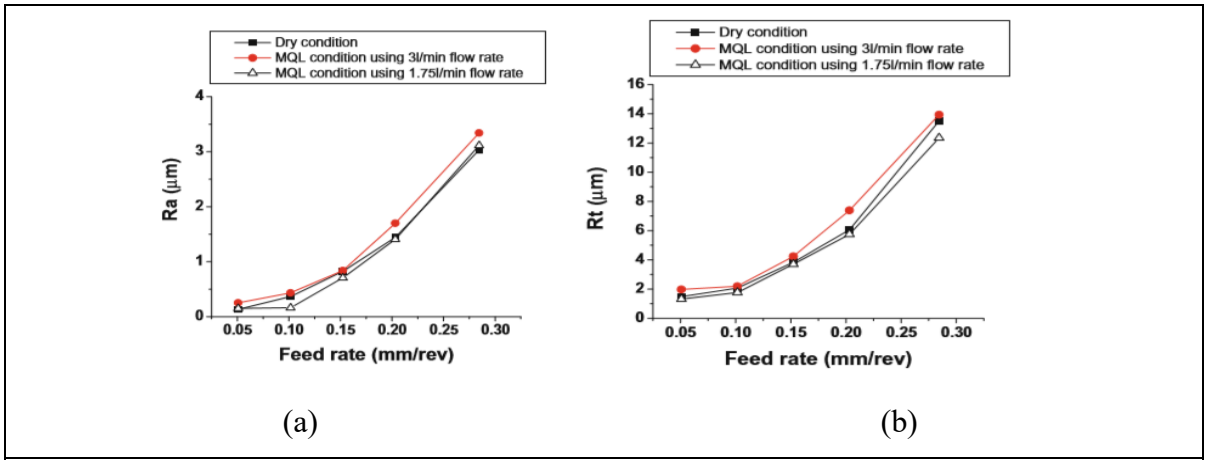

Figure 2.2 Variation of surface roughness with feed rate for dry and MQL with two flow rates (Kouam *et al.*, 2015)

Davim *et al.* (2007) carried out turning of brass for wet and MQL with various flow rates to study the effect of feed rate and cutting speed on surface roughness. The results showed that feed rate increased surface roughness. Moreover, they concluded that wet mode can be replaced by MQL mode due to its better or comparable results. Kamata et Obikawa (2007) compared the influences of MQL, dry and wet modes and cutting speed on surface roughness induced by turning of Inconel 718. They concluded that the best surface finish was obtained for MQL turning in comparison with wet and dry modes. They also concluded that the surface finish was not improved by raising the flow rate of the cutting fluid. It needs mentioning that in these two research studies, the effect of turning environment and parameters on residual stresses was not investigated and optimization was not conducted.

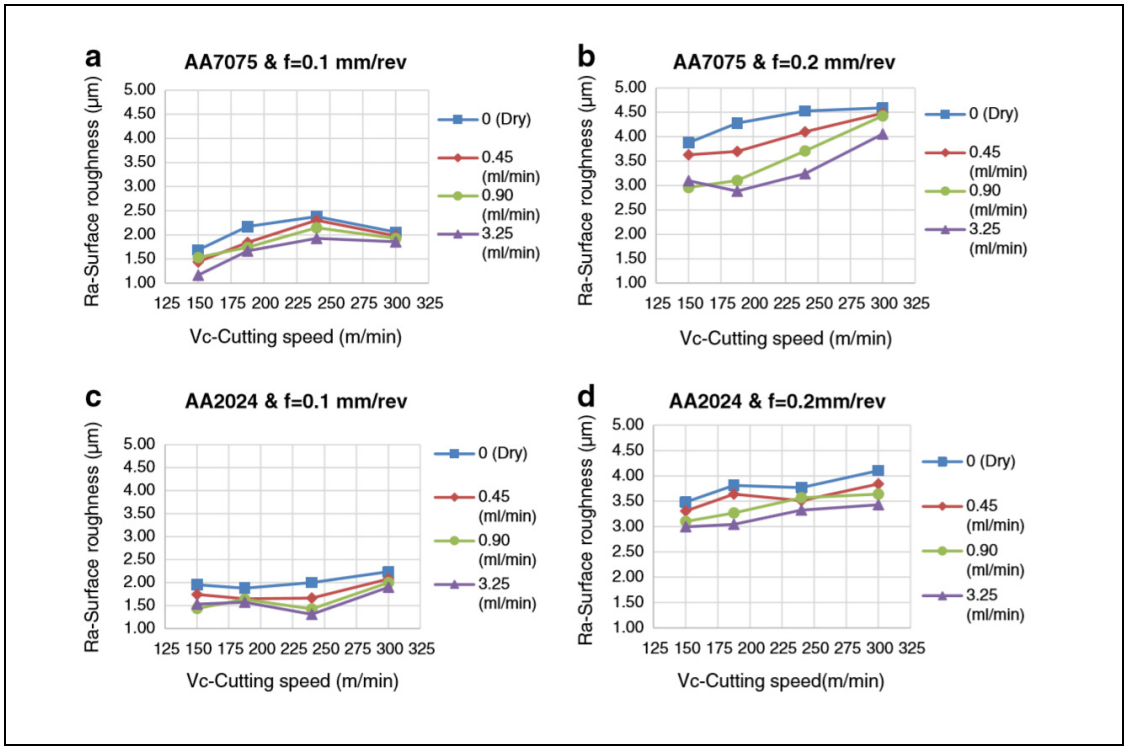

Figure 2.3 Variation of surface roughness with cutting speed for two different aluminum materials, feed rates, and turning environments (Çakır *et al.*, 2016)

Khan *et al.* (2009) studied the impact of MQL, dry, and wet modes on surface roughness of AISI 9310 steel in turning operations. The results showed that MQL considerably improved surface roughness. Leppert (2011) performed dry, MQL, and wet turning of AISI 1045 steel to

study the impact of cutting speed and feed rate on surface roughness and found that MQL turning improved it remarkably. However, in these two research works, the effect of turning environment and parameters on residual stresses was not investigated numerically and experimentally and optimization was not carried out. Senevirathne et Punchihewa (2018) studied the impact of dry, wet, and MQL with some flow rates on surface roughness induced by turning processes of AISI P20 and D2 steels. The results displayed that MQL turning significantly improved surface finish in comparison with wet and dry modes. However, very little data is available on comparative studies of wet, dry and MQL turning of aluminum alloys and their impact on surface roughness.

2.2.2 Effects of turning environments and parameters on residual stresses

The influence of turning parameters on residual stress characteristics for different turning environments was studied in a small number of research works. Leppert et Peng (2012) analyzed the effects of dry, MQL, and wet modes, cutting speed, and feed rate on residual stresses after turning AISI 316L steel. As shown in Figure 2.4 for dry mode, significant differences were observed between axial and hoop residual stresses specifically at low feed rates and cutting speeds. Regarding MQL mode, the results revealed that a larger cutting speed resulted in higher hoop and axial residual stresses. Moreover, clear tendency was not observed about the effect of feed rate on residual stresses in hoop direction, which showed a complex relation between thermal and mechanical factors on the residual stresses. For wet mode, the axial residual stresses were smaller than the hoop residual stresses and their magnitudes rose significantly with increasing feed rate. As a conclusion, they reported that residual stresses induced by dry and MQL modes could be smaller or comparable to those generated by wet turning. However, in this research study, the effect of turning parameters and environment on surface roughness was not studied and optimization of overall surface integrity was not carried out.

Ji *et al.* (2014) studied the impact of dry, wet, and MQL with different flow rates on residual stresses generated by orthogonal turning of AISI 4130 steel. The results showed that surface

residual stress decreased with applying cutting fluids and wet (flood) mode led to lower tensile residual stresses. (Figure 2.5). Boulahmi (2015) performed an experimental study on the effect of feed rate and tool's nose radius on residual stress in turning of AA2024-T4, AA6061-T6, and AA7075-T651 for environments including dry, MQL and wet. They found that residual stresses induced by MQL and wet turning were lower than those generated in dry environment. However, the optimization of overall surface integrity was not conducted and only residual stress in one direction was studied. Moreover, the influences of cutting speed and depth of cut on residual stresses were not investigated.

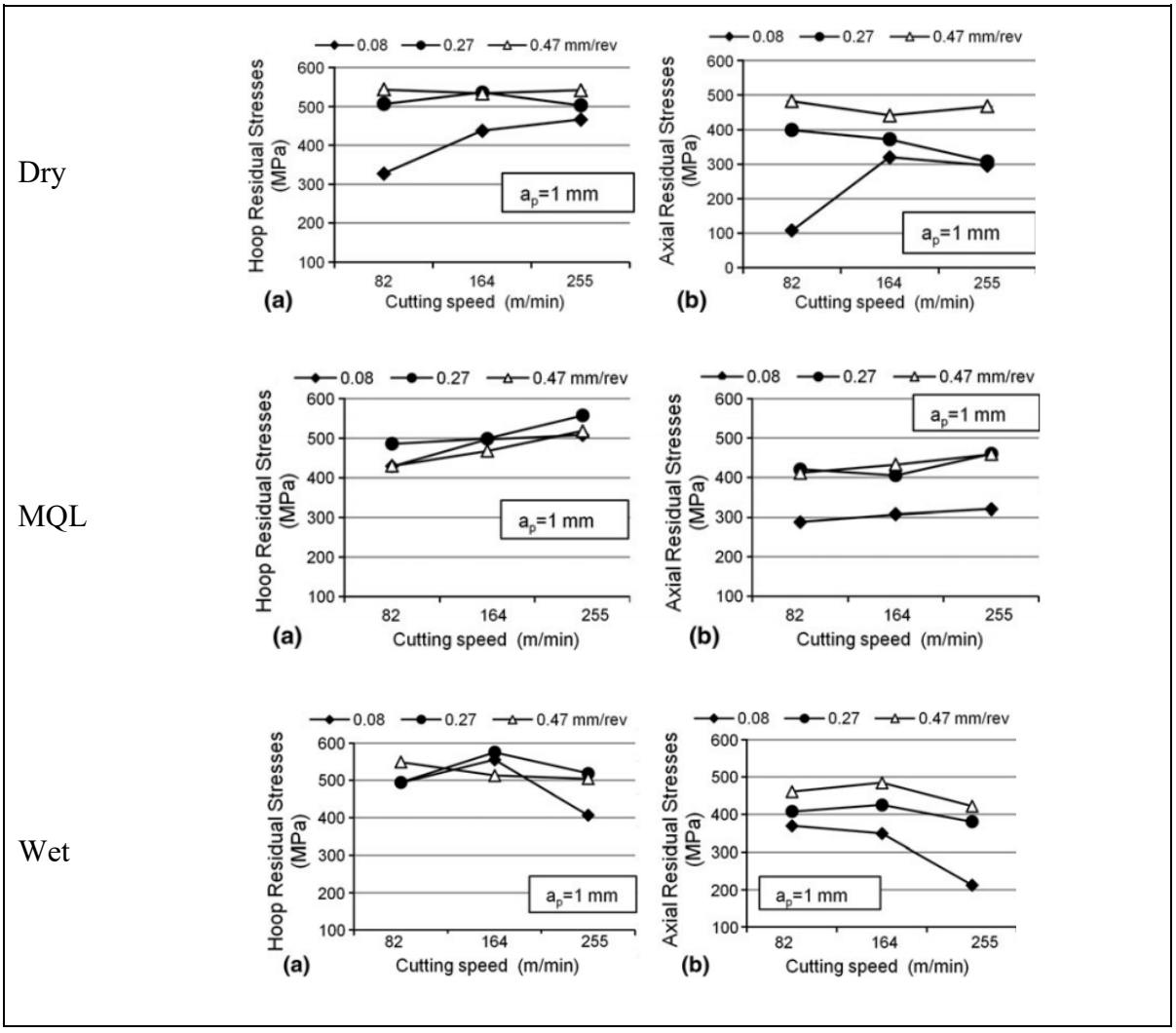

Figure 2.4 Variation of hoop and axial residual stresses with cutting speed and feed rate under different turning environments (Leppert et Peng, 2012)

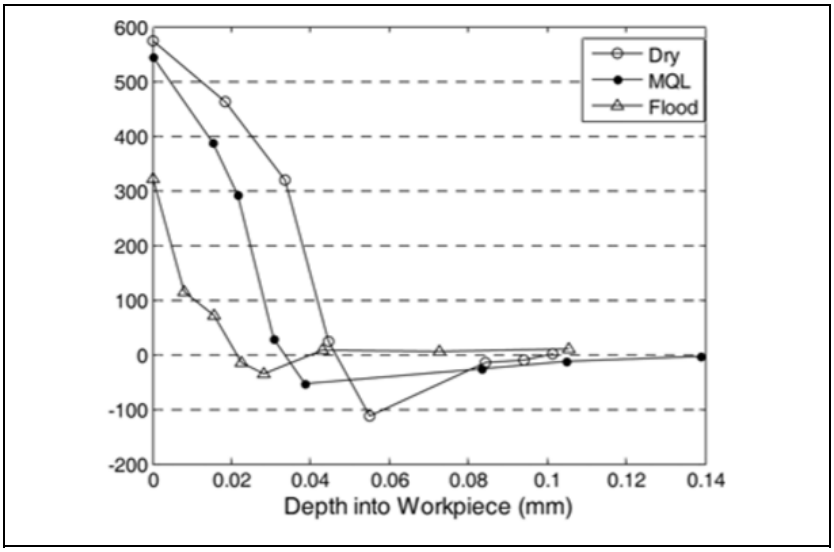

Figure 2.5 Comparison of residual stress distribution for various turning environments (Ji *et al.*, 2014)

2.3 Regression modeling and optimization of surface integrity characteristics

Regression modeling and optimization studies of surface integrity induced by turning processes of metals were investigated by some researchers. Kirby *et al.* (2006) carried out research on AA6061-T6 to obtain the optimal dry turning parameters including spindle speed, feed rate, depth of cut, and tool nose radius in order to reduce surface finish using a Taguchi's L9 orthogonal array experimental design approach. The results demonstrated that feed rate and tool nose radius were the most efficient parameters on surface roughness. Horváth and Drégelyi-Kiss (2015) studied the impact of cutting speed, feed rate, depth of cut, and tool's cutting edge shape on surface roughness of aluminum alloys. CCD, RSM, and multi-performance optimization were used and cutting speed and feed rate were found to be the most influential parameters. Camposeco-Negrete (2015) performed a research work on rough turning of AA6061-T6 in wet environment using CCD and RSM and concluded that feed rate was the most influential parameter for reducing surface roughness. However, the influence of turning environment and parameters on residual stresses was not investigated numerically and experimentally and optimization was not performed.

Jafarian *et al.* (2015) conducted an experimental study to investigate the influence of cutting speed, depth of cut, and feed rate on residual stress induced by wet turning of Inconel 718. An optimization study was performed using Artificial Neural Network and Genetic Algorithm techniques to find optimal values of machining parameters. The results showed that measured residual stresses were tensile and strongly changed by cutting conditions as shown in Figure 2.6, Figure 2.7, and Figure 2.8. However, the impact of turning environment on residual stresses and surface roughness was not studied and the optimization of overall surface integrity was not carried out.

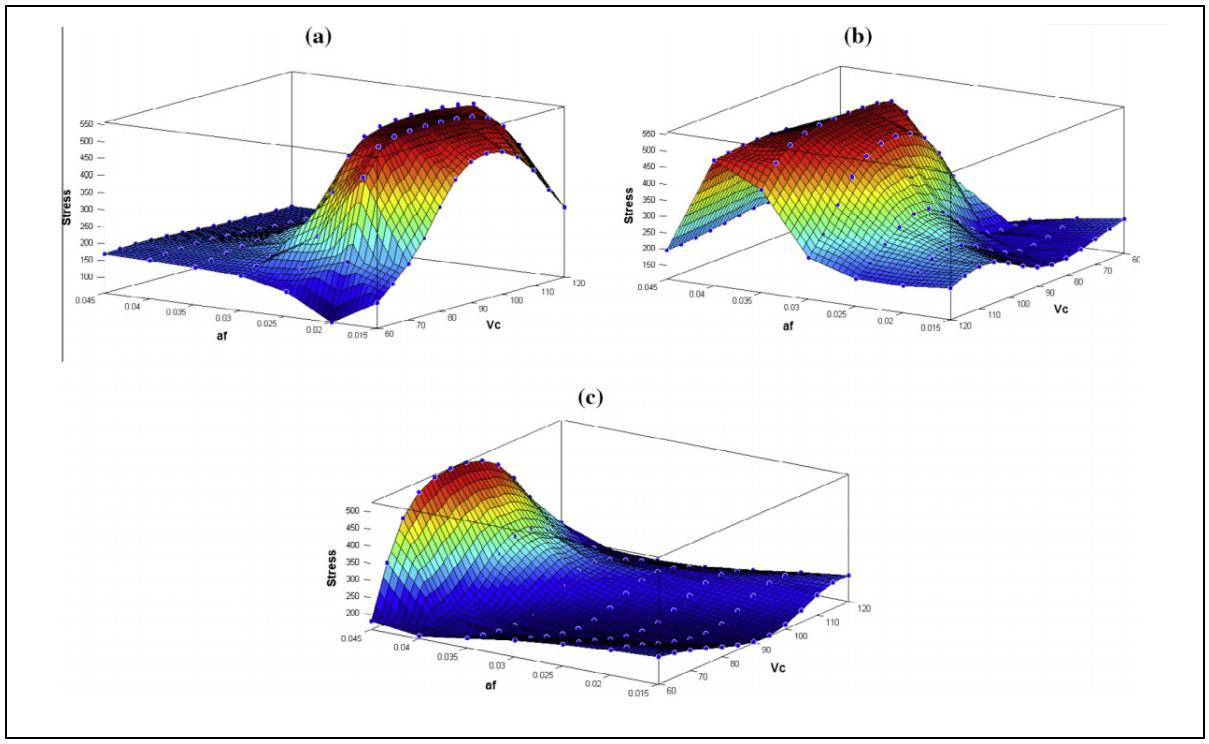

Figure 2.6 Effect of cutting speed (Vc) and feed rate (af) on residual stress in the depths of cut (a) 0.3, (b) 0.45 and (c) 0.6 mm (Jafarian *et al.*, 2015)

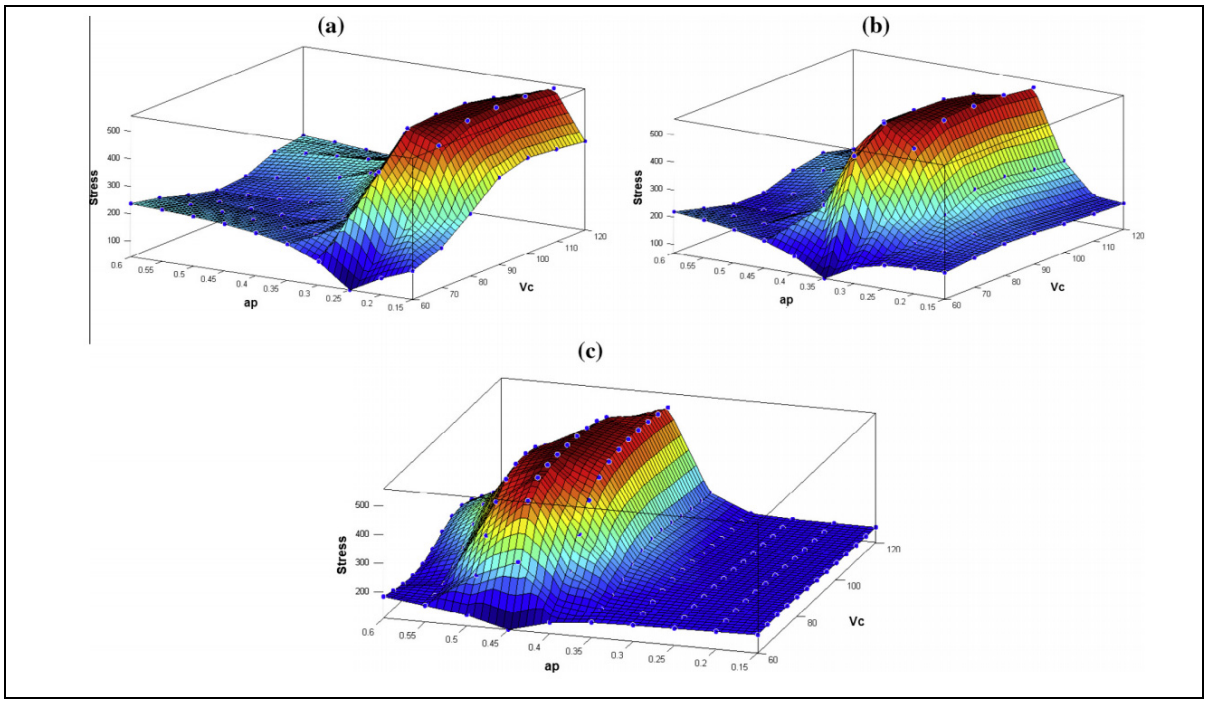

Figure 2.7 Effect of cutting speed (Vc) and depths of cut (ap) on induced residual stress at the feed rate (a) 0.015, (b) 0.025 and (c) 0.035 mm/rev (Jafarian *et al.*, 2015)

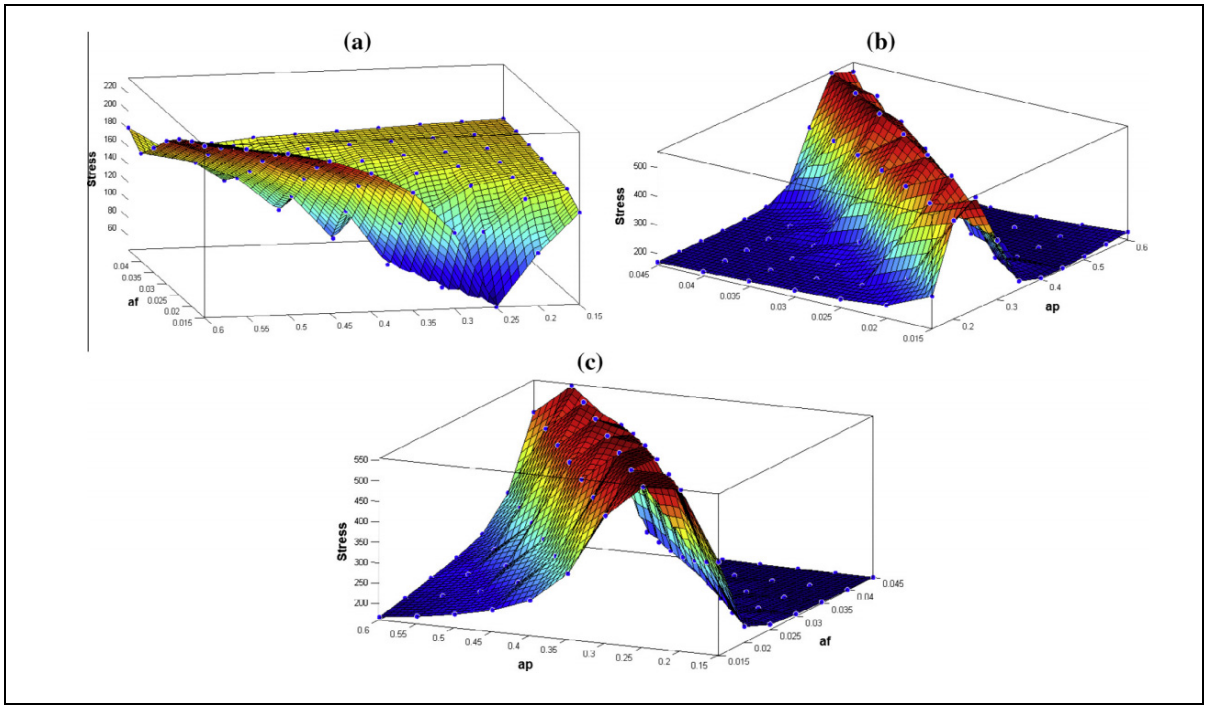

Figure 2.8 Effect of feed rate (af) and depths of cut (Vc) on induced residual stress at the cutting speed (a) 60, (b) 80 and (c) 100 m/min (Jafarian *et al.*, 2015)

Priyadarshi et Sharma (2016) investigated the influence of cutting speed, feed rate, and depth of cut on average arithmetic surface roughness and cutting forces in dry turning of Al-6061-SiC-Gr hybrid nanocomposites. CCD, RSM, and multi-objective optimization were performed to improve the responses. The results showed that feed rate and depth of cut considerably affected surface roughness and cutting forces. The optimization results demonstrated that all the cutting conditions approached the upper bounds in the design space (Figure 2.9).

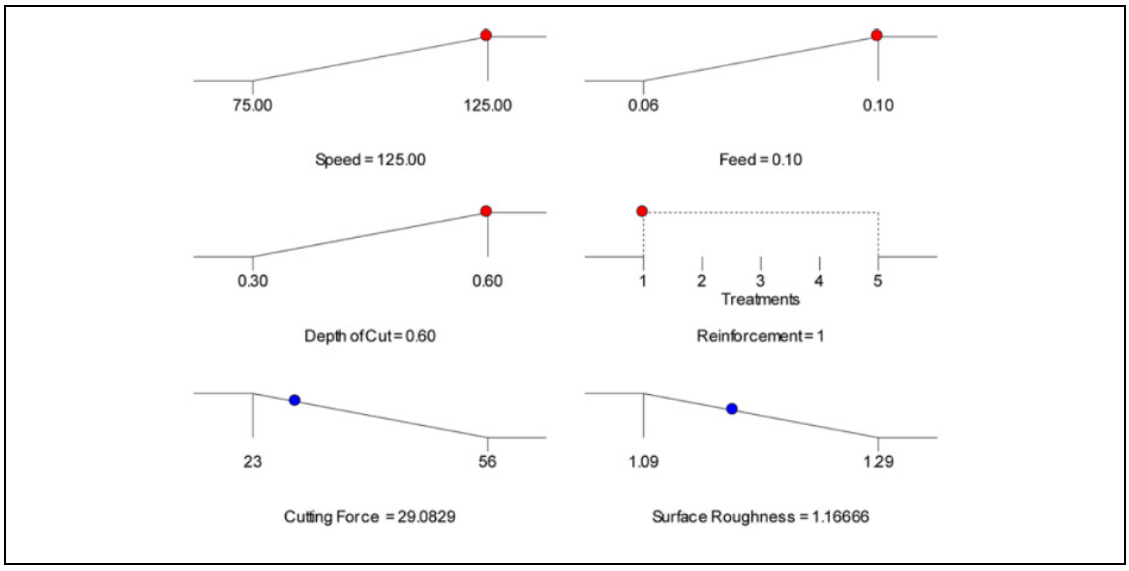

Figure 2.9 Multi-objective optimization results of dry turning of Al-6061-SiC-Gr hybrid nanocomposites (Priyadarshi et Sharma, 2016)

Deepak et Rajendra (2016) carried out an optimization study to improve the arithmetic average surface roughness induced by dry turning of AA6061 using RSM and a Taguchi L9 orthogonal array experimental design method. They concluded that feed rate was the most efficient cutting parameter on surface roughness. Saravanakumar *et al.* (2018) performed an optimization of cutting speed, feed rate, and depth of cut generated by dry turning of AA6063 using RSM and a Taguchi's L27 orthogonal array experimental design method to reduce surface roughness. The results revealed that surface roughness was considerably affected by feed rate and then by cutting speed (Figure 2.10). However, in these two research works, the influence of turning parameters and environments on residual stresses was not investigated and optimization of surface integrity was not performed.

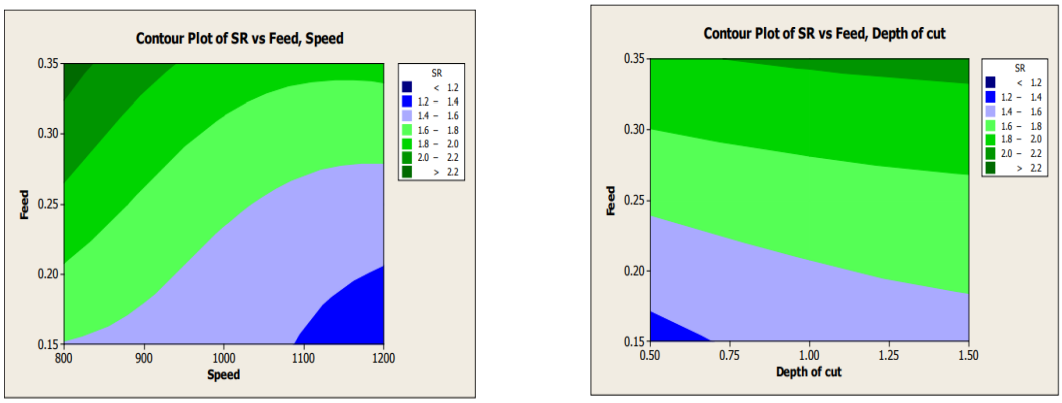

(a) (b)

Figure 2.10 Optimization results of dry turning of AA6063: (a) Surface roughness Vs speed, feed and (b) surface roughness Vs depth of cut, feed (Saravanakumar *et al.*, 2018)

Sateesh *et al.* (2018) obtained the optimum values of spindle speed, feed rate, and depth of cut to improve the surface roughness of the component in dry turning of Al6063-T6 using a Taguchi L9 orthogonal array and the Grey relational analysis. The optimum value of the arithmetic average surface roughness was captured for the highest spindle speed and depth of cut and the smallest feed rate in the design space. Warsi *et al.* (2019) found the optimal cutting speed, feed rate, and depth of cut during dry high-speed turning of AA6061-T6 alloy to decrease surface roughness. RSM, the Taguchi's L18 orthogonal array design method and the Grey relational analysis were used to identify optimal values. The ANOVA results demonstrated that feed rate was the most influential factor affecting surface roughness, followed by cutting speed and depth of cut.

For residual stresses generated by turning of metals, a few research works studied the impacts of turning parameters using regression modeling. Moreover, few studies determining regression models and conducting the optimization of surface integrity parameters in turning of aluminum alloys under various environments were found in the literature. Ajaja *et al.* (2019) carried out a multi-performance optimization to obtain the optimal values of cutting insert, cutting speed, feed rate, and depth of cut in order to reduce residual stresses and surface

roughness parameters induced by wet turning of 300M steel. They applied RSM and three different approaches named the single-response Taguchi method, the multi-response Grey relational analysis, and the proportion quality loss reduction method. However, the impact of different turning environments on surface integrity was not studied and analyzed.

Leppert et Peng (2012) experimentally analyzed the impact of dry, MQL, and wet modes and cutting speed, feed rate, and depth of cut on residual stresses induced by turning AISI 316L steel using regression modeling. They concluded that optimal residual stresses in dry and MQL modes could be lower or comparable to those generated in wet turning. Boulahmi (2015) carried out an optimization of feed rate and tool's nose radius to minimize surface roughness parameters and residual stress in turning AA2024-T4, AA6061-T6, and AA7075-T651 under dry, MQL and wet modes using DoE and RSM. They found that MQL turning led to the best results for all single-criterion optimizations. It was found that surface roughness rose with increasing feed rate and compressive residual stresses occurred for the smallest feed rates. However, the influence of cutting speed and depth of cut on surface roughness and residual stress were not studied and the responses were not optimized simultaneously.

2.4 2D/3D finite element prediction of machining characteristics and residual stresses

Since last decades, FE modeling and simulation of machining operations have attracted many researchers' attention. There are a small number of software including DEFORM™, Abaqus®, ANSYS, and AdvantEdge™ for modeling of machining operations using FEM. The developed FE models are reliable tools which enable manufacturers to improve both the productivity (material removal rate, tool life, etc.), part surface integrity (residual stresses, microstructural alterations), and fatigue life and corrosion resistance (Jomaa *et al.*, 2017). To validate the developed FE models, experimental results of machining characteristics and surface integrity should be utilized. In the following, an overview on the latest FE research works on machining characteristics and surface integrity induced by turning processes, with a particular focus on aluminum alloys is provided.

Guo et Liu (2002) investigated the effect of cutting parameters on machining characteristics and residual stresses in turning of AISI 1020 using Abaqus® software. The results showed that compressive residual stresses were generated by reducing uncut chip thickness to below a threshold value in the second sequential cutting pass. Yen *et al.* (2004) analyzed the influence of various tool edge parameters on cutting parameters using simulations of orthogonal cutting of AISI 1020 with DEFORM-2D™ software. They revealed that tool wear was directly dependent on machining temperature, stresses on the tool, and chip velocity

Hua *et al.* (2005) developed a numerical model to simulate residual stresses and study the influence of tool edge geometry, workmaterial hardness, feed rate, and cutting speed in turning of AISI 52100 steel. A hardness-based constitutive material model was implemented into a FE model using DEFORM-2D™ software. They found that the best residual stresses were obtained using a chamfered tool with a medium value of hone radius.

Filice et al. (2006) used a combined method of analytical and pure thermal FE models using DEFORM-3D™ software to model turning of AISI 1045 steel. There was good agreement between the predicted and experimental results. Outeiro *et al.* (2006) experimentally and numerically studied the impact of machining parameters on residual stresses generated by orthogonal cutting of AISI 316L steel using DEFORM-2D™ software. The results demonstrated that residual stresses were more dependent on uncut chip thickness and sequential cutting passes.

Umbrello (2008) analyzed the behavior of Ti6Al4V in high speed and conventional orthogonal cutting based on different Johnson-Cook models using DEFORM-2D™ software. The results showed that accurate prediction of machining characteristics was realized only by using the constant of Johnson-Cook model obtained at high strains, strain rates, and temperatures. Arrazola and Özel (2008) developed a 3D finite element model for hard turning of AISI 4340 to predict cutting temperature, Von Mises stresses and contact pressure for one cutting condition using Abaqus/Explicit®. The results showed good agreement between FE model predictions and experimental results reported in the literature. Özel et Ulutan (2012) developed

a 3D FE model using the DEFORM™ software to investigate the influence of various tool geometry parameters and coatings on residual stresses induced by dry turning of Ti-6Al-4V and IN100 alloys. The simulation results showed that increasing cutting edge radius led to more compressive residual stresses and also the presence of coating caused more tensile stresses on the surface of machined component.

Abboud *et al.* (2013) developed a FE model using DEFORM-2D™ software to predict residual stress induced by orthogonal machining of Ti6Al4V. In their study, the influence of cutting tool radius and cutting speed on residual stress was investigated. It was found that increasing feed rate led to compressive residual stresses and increasing edge radius or cutting speed caused less compressive residual stresses. Davoudinejad *et al.* (2015) developed a 2D finite element model to investigate the effect of dry and cryogenic turning of Ti6Al4V on chip formation and machining forces using AdvantEdge™ software. It was concluded that using cryogenic conditions led to increasing machining forces and reducing chip segmentation and thickness.

Akram *et al.* (2016) developed a 2D FE model to study the influence of cutting speed and feed rate on the chip thickness of AA6061-T6 induced by orthogonal turning using Abaqus®/Explicit software. The results showed that the chip thickness diminished and increased with increasing cutting speed and feed rate, respectively. Korkmaz and Günay (2018) conducted 2D/3D FE simulations to predict and model the effect of cutting speed, depth of cut, and feed rate on power consumption and cutting forces in turning of AISI 420 steel using AdvantEdge™ software. Moreover, ANOVA and optimization were performed based on FE results to recognize and obtain the most influential factors and optimum solutions, respectively. The results showed that depth of cut was the most effective factor on both cutting forces and power consumption. In addition, the optimal values of cutting conditions reduced cutting forces and power consumption significantly.

Emamian (2018) developed a 2D FE model of orthogonal turning of AISI 1045 steel using Abaqus®/Explicit software. The results revealed that machining forces raised with feed rate for

different edge radii. Patel (2018) developed a 2D FE model of orthogonal turning of aluminum alloy AA2024-T351 using the Abaqus® software to investigate the effect of cutting speed, feed rate, and rake angle on machining forces. The results displayed that machining forces increased with raising feed rate and decreasing rake angle. Moreover, machining forces slightly decreased with increasing cutting speed. Mali *et al.* (2019) conducted a 3D finite element analysis to predict machining forces induced by dry turning of AA7075 using DEFORM-3D™ software. The results demonstrated that finite element prediction of cutting and feed forces were in agreement with the experimental results.

Liu *et al.* (2020) developed a 2D finite element model using AdvantEdge™ software to predict machining forces generated by orthogonal turning of Inconel 718 under high-pressure cooling environment. The predicted results demonstrated good agreement with the experimental ones. Jiang *et al.* (2020) developed a 3D finite element model to predict the distribution of radial residual stresses of machined surfaces in turning of high strength alloy steel (40CrMnMo) using DEFORM-3D™ software. The research results displayed that the simulation and experimental results both had the same variation of RS and were in good agreement.

However, the above overview of the previous studies shows that the interactions between cutting conditions and tool geometry on machining characteristics induced by low speed and high speed turning of AA6061-T6 were not investigated using 2D FE models. Regarding 3D FE models, the machining characteristics and residual stresses were not predicted and compared for different turning environments and parameters.

2.5 Summary and conclusive remarks

The review of the literature reveals:

- There are few studies which numerically and experimentally investigated the influence of turning environment (cutting fluids) and turning parameters (cutting conditions and tool geometry) on machining characteristics including machining forces and

temperature and surface integrity consisting of surface roughness and residual stresses induced by low and high speed turning of AA6061-T6.

- The effect of turning environment on residual stresses generated by turning of AA6061-T6 was not analyzed for various turning parameters by the previous studies.

- The turning parameters were not optimized to improve the overall residual stress and surface roughness parameters in turning of AA6061-T6 under different environments.

- 2D FE model was not developed for orthogonal turning of AA6061-T6 to investigate the interaction between the edge radius and cutting speed, feed rate, and rake angle and their effects on machining characteristics including machining forces, temperature, and chip thickness, especially in the range of high speed machining of aluminum alloys.

- 3D FE models were not developed and compared for turning of AA6061-T6 under three environments including DRY, MQL, and WET.

Accordingly, more numerical and experimental models and studies on machining and surface integrity characteristics are highly required in turning of AA6061-T6 to cover these critical gaps in order to assist the industry to optimally select turning environment and parameters and improve the surface quality of machined components.

CHAPTER 3

METHODOLOGY

3.1 Experimental measurements

The principles of measurements of machining and surface integrity characteristics are described as below:

3.1.1 Machining force and chip shape measurements and observation

A Kistler (type 9121) three-component piezoelectric dynamometer was used to measure machining forces in two and three directions for orthogonal turning and turning operations, respectively. LabVIEW software was used to capture the acquisition of force signals and MATLAB codes were also utilized to conduct the data treatment. Moreover, a digital micrometer was used to obtain chip thickness by averaging the values of the chip thickness at three different locations far enough from the two ends of the chip. To determine the chip shape, a piece of chip was first mounted using Struers hot mounting machine, then polished with a NANO 2000T polisher, and finally observed using a HITACHI TM3000 Scanning Electron Microscope (SEM), as shown in Figure 3.1.

(a) (b) (c)

Figure 3.1(a) Struers hot mounting machine, (b) NANO 2000T polisher and (c) HITACHI TM3000 SEM

3.1.2 Surface roughness measurement

Non-contact or contact type instruments can be used to measure surface roughness. In non-contact types including Laser microscope, without contacting the sample, light is emitted from and reflected back to the machine to measure the roughness. This instrument does not scratch the sample surface, and therefore, can be used for roughness measurements in soft materials. In the contact-type machine such as profilometer or perthometer, the tip of stylus directly touches the surface of the sample and registers the vertical positions of the points on the surface as it moves. The stylus moves on the sample surface, and consequently, the produced R-profile is reliable (Sadeghifar, 2017). In the present work, a Mitutoyo SJ-400 profilometer was used because it measures roughness with high accuracy and it is also faster and less expensive in comparison with a laser microscope. All the surface roughness parameters were obtained and recorded. The theoretical arithmetic average surface roughness R_a and the maximum height of the profile R_t as the most common roughness parameters to show the surface quality were used and analyzed in this research study. An example of extracted R_a and R_t from surface roughness profile is illustrated in Figure 3.2.

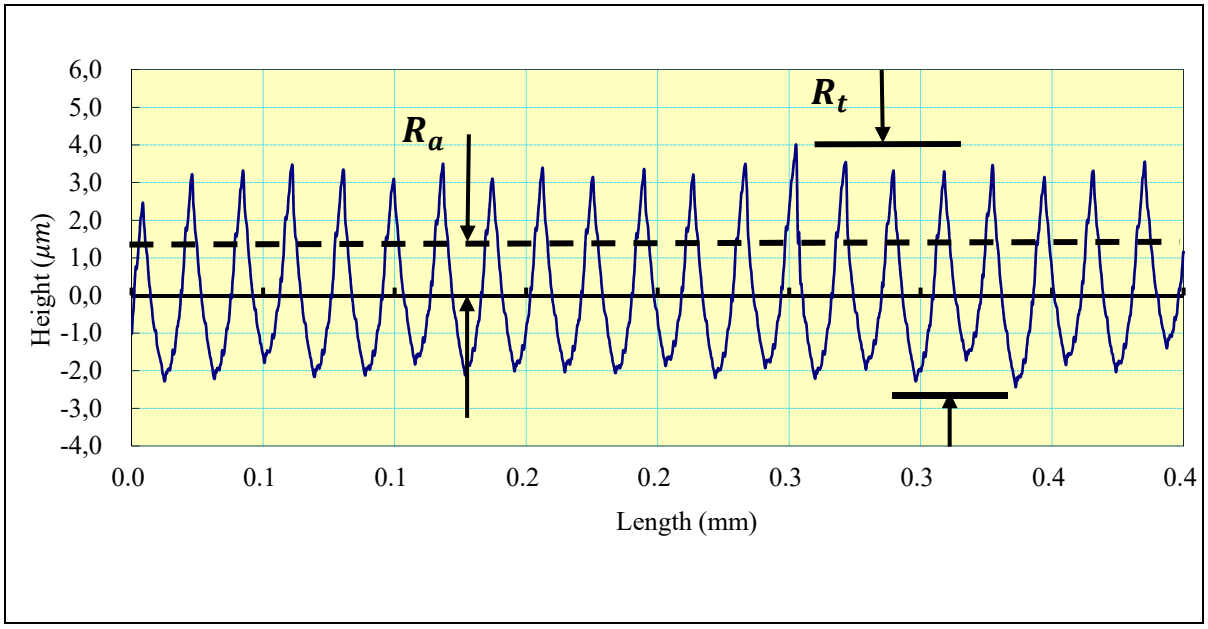

Figure 3.2 Definition of R_a and R_t

3.1.3 Residual stresses measurement

X-Ray Diffraction (XRD) is a non-destructive technique for measuring residual stresses in crystalline materials using lattice spacing or d-spacing as a strain gage. When the X-Ray waves enter the specimen, the waves scattered by the atoms in the specimen interfere.

The spacing d between atomic planes inside the specimen material is measured and calculated using Bragg's law, which shows the difference in the path length between incident and diffracted beams must be an integer multiple of wavelength (Sadeghifar, 2017), as demonstrated in Figure 3.3. Therefore, Bragg's formula is given as:

$$AB + BC = n\lambda \tag{3.1}$$

which results in:

$$2d\sin\theta = n\lambda \tag{3.2}$$

where n is an integer indicating the order of diffraction, λ is the X-Ray beam wavelength, d is crystal planes lattice spacing, and θ is the diffraction angle.

When the lattice spacing changes, a corresponding shift of a few increments of degree in the diffraction angle 2θ occures. It is displayed by differentiating the Bragg's formula (Sadeghifar, 2017):

$$\frac{\Delta d}{d} = -\Delta\theta\cot\theta \tag{3.3}$$

where $\Delta d = d - d_0$ and $\Delta\theta = \theta - \theta_0$, where d_0 and θ_0 are the lattice spacing and diffraction angle of the stress-free material. Eq. (3.3) as a function of $\Delta 2\theta$ becomes:

$$\frac{\Delta d}{d} = -\frac{\Delta 2\theta}{2}\cot\theta \tag{3.4}$$

where $\Delta 2\theta = 2\Delta\theta$.

XRD is used to measure elastic strains which change the mean lattice spacing (Prevéy, 1986; Sadeghifar, 2017). The inelastic strains result in dislocation motion and formation of micro-stresses occurring locally. Furthermore, these strains never affect macroscopic stresses which form over grains in the material. Accordingly, although residual stresses are created because of non-uniform plastic deformation, all macro residual stresses are created elastically (Prevéy, 1986; Sadeghifar, 2017).

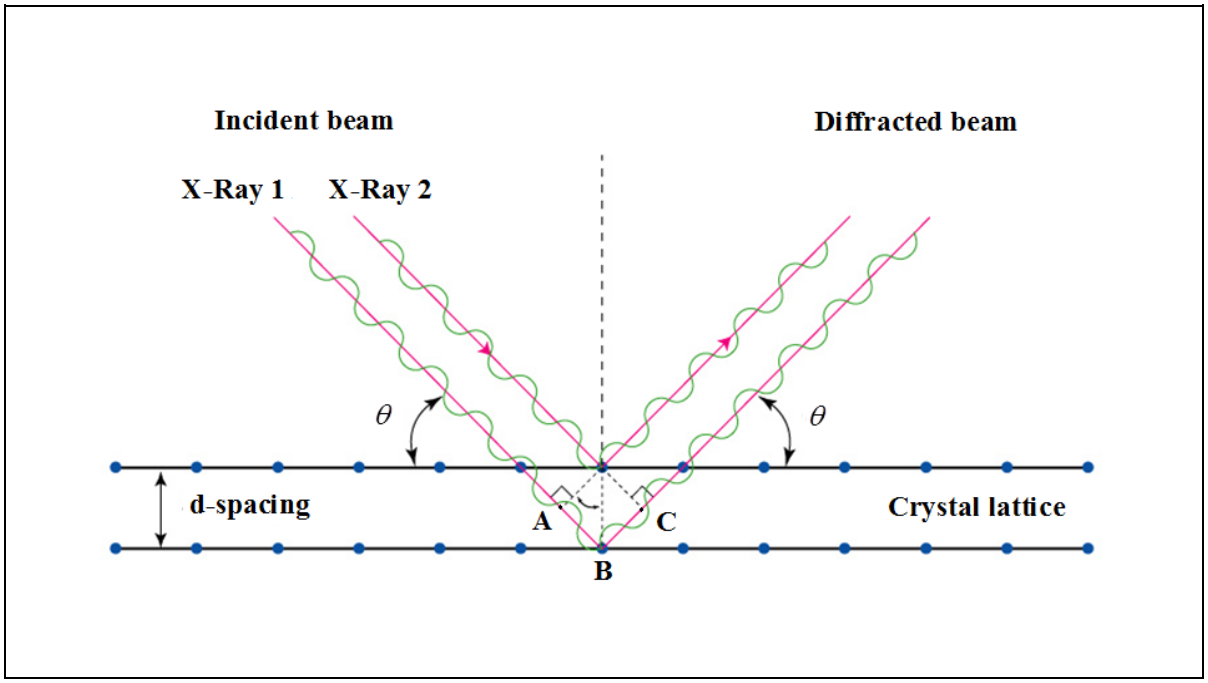

Figure 3.3 Bragg's law (Barth, 2007)

In our laboratory, residual stresses can be measured using two types of XRD machines. The first one is called Pulstec μ-X360n machine which first gathers the full diffracted cone known as Debye-Scherrer ring using a two-dimensional detector for a single incident angle of X-Rays (Figure 3.4(a)) and then computes residual stresses using Cos α method. The second machine is named Proto iXRD machine that collects the beams from the diffracted cone on two opposite sides using two detectors for multi incident angle of X-Rays (Figure 3.4(b)) and then computes residual stresses through $Sin^2\Psi$ method (Sadeghifar, 2017). The measurement time is around 2 and 10 minutes for Pulstec and Proto machines, respectively, revealing that the measurement of residual stress using Pulstec machine is faster compared with Proto machine. It can be attributed to the fact that the Pulstec machine utilizes a single exposure of X-Ray beams on the sample, whereas multiple exposures are used for the Proto machine (Sadeghifar, 2017). In the present research study, Pulstec μ-X360n machine was used to measure residual stresses.

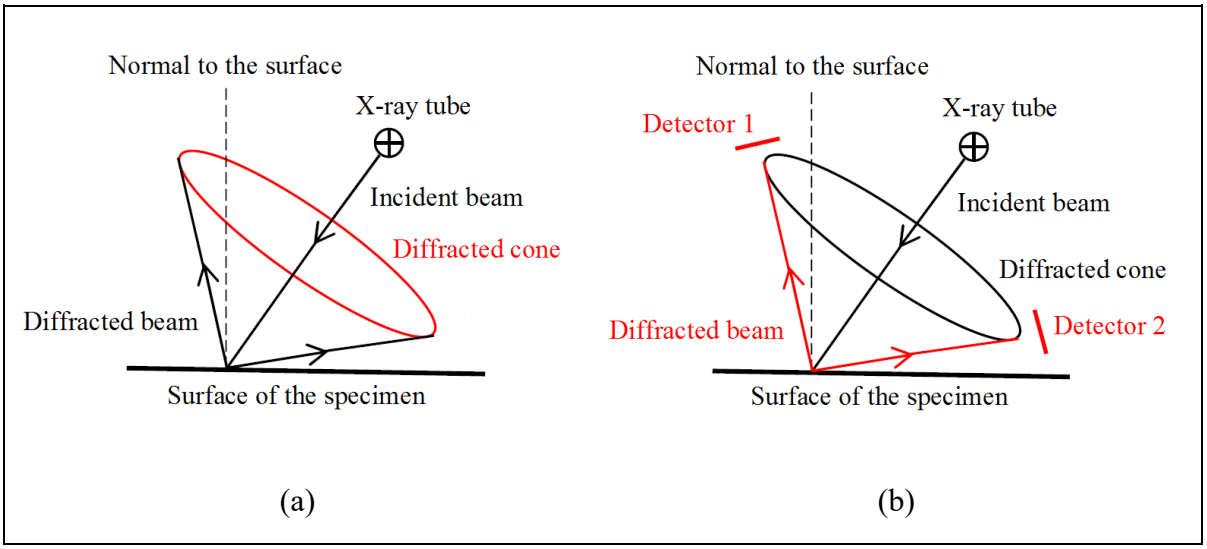

Figure 3.4 (a) Pulstec μ-X360n equipment versus (b) Proto iXRD apparatus (Sadeghifar, 2017)

3.2 Design of Experiment, Analysis of Variance, Response Surface Method, and optimization processes

Design of Experiment (DoE) is a statistical method to maximize the information gain while minimizing the number of time-consuming and expensive experiments. DoE can be divided into two main categories called physical and computer experiments. Full or fractional factorial designs, Central Composite Design (CCD), and Box-Behnken Design (BBD) are some of physical/classical DoEs, which contain some stochastic noise. On the other hand, Point Exchange, D optimal, and IV-optimal are a number of computer-based DoEs, which lack any noise as repeated computer simulations with the same inputs always result in identical outputs (Gianchandani, 1998; Sadeghifar, 2017). Among the physical DoEs, CCD is the most well-known commonly used DoE being suitable for regression modeling and optimization processes. In the present research work, DoE based on CCD was used to conduct turning experiments.

Analysis of Variance (ANOVA) is a statistical method to determine significant differences between models, check the adequate precision of the models, verify the statistical significance of the individual terms of the model and calculate the regression coefficients (Jumare *et al.*, 2019).

RSM is a combination of statistical techniques and mathematical theory which quantifies the relationship between the controllable independent parameters as input and the obtained dependent response surfaces as output (Kosaraju et Anne, 2013). The formulation of the second-order polynomial models including linear, quadratic and interaction terms can be presented as follows:

$$y = b_0 + \sum_{i=1}^{k} b_i x_i + \sum_{i<j} \sum b_{ij} x_i x_j + \sum_{i=1}^{k} b_{ii} x_i^2 + \epsilon \qquad (3.5)$$

where b_0 is the intercept, b_i, b_{ij}, and b_{ii} are the unknown regression coefficients, k indicates the number of parameters, and ϵ is an experimental error.

An optimization problem is performed to maximize or minimize response functions as objectives by systematically choosing the best values of input parameters within an allowable range according to some optimal solution criteria. There are different types of optimization methods including Genetic Algorithms (GA), Neural Networks, Sequential Quadratic Programming (SQP), Grey Relational Analysis (GRA), and Hill Climbing Technique, etc. Hill climbing technique, which was used in this study, is an iterative algorithm that starts with an arbitrary solution, provides a hill to climb if the optimization goes in an undesirable direction, then attempts to obtain a better solution by applying an incremental change to the solution.

3.3 Finite element modeling

Machining operations are nonlinear, coupled thermo-mechanical dynamic processes. Because of their complexity, selecting proper geometrical, mechanical, thermal, material, frictional, and chip formation models and parameters is significant to have a successful finite element model for simulations and predictions. Two different FE models are developed in DEFORM^{TM} software to simulate the cutting and stress relaxation processes. First, dynamic thermo-mechanical simulation is carried out to simulate the cutting process using the relative motion of the tool and workpiece as the first step. Thereafter, a thermo-mechanical analysis is conducted to model the stress relaxation process by cooling the workpiece and tool as the second step.

It is known that the material constitutive models utilized in FE modeling of machining operations cannot be determined using quasi-static tests. This is attributed to the fact that the workpiece undergoes high temperature, strain rate, and strain during the cutting process. As summarized in Table 3.1, various material equations were frequently used in finite element simulation of cutting processes. The Johnson-Cook constitutive model has been commonly

used in simulation of machining processes as it showed to be suitable and reliable in metal cutting simulations.

Mostly, in commercial FE codes, two methods utilized to show chip formation during metal cutting processes which are called pure deformation and chip separation criterion methods. Chip separation criterion is divided into two main methods named geometrical and physical. The main problem of the chip separation method is predefining the chip formation which may not be accurate. To overcome the drawbacks of chip separation criterion method, pure deformation method based on automatic remeshing method was developed. In automatic remeshing method, when mesh distortion is detected, new mesh is generated to simulate the chip formation. DEFORM^{TM} software uses pure deformation method for machining simulations.

Different formulations have been utilized in FE modeling of machining processes, consisting of pure Lagrangian (PL), updated Lagrangian (UL), and Eulerian (E) formulations. In the updated Lagrangian and pure methods, the mesh follows the material and the cutting process can be simulated to reach to the steady state condition. Accordingly, without the need to have a predefined chip shape, the chip formation can be modeled. It should be mentioned that the PL formulation needs a physical or geometrical criterion for simulating chip separation, which is different from the UL formulation as it uses a remeshing scheme. On the other hand, in the Eulerian formulation, the mesh is fixed while the material moves along the mesh, omitting the element distortion and decreasing the computational time significantly. However, the Eulerian formulation requires a predefined chip shape and therefore residual stresses cannot be simulated as the elasticity of the work material is not considered (Sadeghifar, 2017). Therefore, the UL formulation is more useful, practical than the E formulation in machining processes. In DEFORM^{TM} software, the UL formulation is used for machining processes.

The geometrical, mechanical, thermal, and frictional models and boundary conditions of 2D/3D FE models are explained in detail in the following chapters.

Table 3.1 Material constitutive models utilized in FE modeling of machining operations

Model	Constitutive Equation	Constants
Johnson-Cook	$\sigma = (A + B\varepsilon^n)\left(1 + C\ln\left(\frac{\dot{\varepsilon}}{\dot{\varepsilon}_0}\right)\right)\left[1 - \left(\frac{T - T_0}{T_{melting} - T_0}\right)^m\right]$	A, B, n, C, m
Power law	$\sigma = \sigma_0 \left(\frac{\varepsilon}{\varepsilon_0}\right)^n \left(\frac{\dot{\varepsilon}}{\dot{\varepsilon}_0}\right)^m \left(\frac{T}{T_0}\right)^p$	σ_0, n, m, p
Zerilli-Armstrong	$\sigma = C_0 + C_1\exp\left[-C_3 T + C_4 T \ln\left(\frac{\dot{\varepsilon}}{\dot{\varepsilon}_0}\right)\right] + C_5\varepsilon^n$ for bcc crystal structures $\sigma = C_0 + C_2\varepsilon^n\exp\left[-C_3 T + C_4 T \ln\left(\frac{\dot{\varepsilon}}{\dot{\varepsilon}_0}\right)\right]$ for fcc crystal structures	C_0, C_1, C_3, C_4, C_5
Usei-Maekawa-Shirakashi	$\sigma = \sigma_0(T, \dot{\varepsilon})\left(\int_{path} e^{\frac{K}{n}T}\dot{\varepsilon}^{-\frac{m}{n}} d\varepsilon\right)^n$	K, n, m
Oxley	$\sigma = \sigma_0(T, \dot{\varepsilon})\, \varepsilon^{n(T,\dot{\varepsilon})}$	-
Marusich	$\left(1 + \frac{\dot{\varepsilon}_p}{\dot{\varepsilon}_0}\right) = \left(\frac{\sigma}{g(\varepsilon_p)}\right)^{m_1}$ if $\dot{\varepsilon}_p < \dot{\varepsilon}_t$ $\left(1 + \frac{\dot{\varepsilon}_p}{\dot{\varepsilon}_0}\right)\left(1 + \frac{\dot{\varepsilon}_t}{\dot{\varepsilon}_0}\right)^{\frac{m_2}{m_1}-1} = \left(\frac{\sigma}{g(\varepsilon_p)}\right)^{m_2}$ if $\dot{\varepsilon}_p > \dot{\varepsilon}_t$ $g(\varepsilon_p) = [1 - \alpha(T - T_0)]\,\sigma_0\left(1 + \frac{\varepsilon_p}{\varepsilon_0}\right)^{\frac{1}{n}}$	$m_1, m_2, \alpha, \sigma_0, n$

CHAPTER 4

ON THE IMPACTS OF TOOL GEOMETRY AND CUTTING CONDITIONS IN STRAIGHT TURNING OF ALUMINUM ALLOYS 6061-T6: AN EXPERIMENTALLY VALIDATED NUMERICAL STUDY

Mahshad Javidikia[1], Morteza Sadeghifar[2], Victor Songmene[1], Mohammad Jahazi[1]

[1]Department of Mechanical Engineering, École de Technologie Supérieure, 1100 Notre-Dame Ouest, Montréal, Québec, Canada H3C 1K3
[2]Department of Mechanical, Industrial and Aerospace Engineering, Concordia University, 1455 Boulevard de Maisonneuve O, Montréal, Québec, Canada H3G 1M8

This article is published in "International Journal of Advanced Manufacturing Technology", Volume 106, January 2020, Pages 4547-4565
DOI 10.1007/s00170-020-04945-3

4.1 Abstract

Aluminum alloys 6061-T6 are widely utilized in the automotive, aerospace and marine industries due to high corrosion resistance, high strength, and good workability and machinability. The machining performance of these alloys depend on several factors including tool's material, coating and geometry. Cutting tool edge radius is one of the most effective factors in cutting forces, energy requirement and chip formation during metal cutting. The present article aims to study the interactions between the cutting edge radius and cutting speed, feed rate and rake angle and examine the impacts of the aforementioned tool geometry and cutting conditions on machining forces, cutting temperature, and chip thickness in cutting an aluminum alloy 6061-T6. Special attention is devoted to examining the influence of the cutting edge radius on machining variables and comparing the results of conventional machining (CM) and high speed machining (HSM). A finite element model was developed to simulate the above interactions and was experimentally validated for different machining parameters. The results demonstrate that although increasing the cutting edge radius clearly raises the machining forces, it has a slight influence on the chip thickness. It is also found that the maximum cutting

temperatures remain nearly constant with changes in the tool edge radius, while the average temperatures of the tool tip increase, especially in HSM. Furthermore, it was found that the location at which the maximum cutting temperature occurs depends more on cutting conditions and tool geometry than workpiece and tool materials.

Keywords: AA6061-T6; Straight Turning; Tool Edge Radius; Finite Element Method

4.2 Introduction

Machining of metals is often accompanied by non-uniform cutting temperatures and machining forces, producing residual stresses. These temperatures and forces may lead to inaccuracies in component dimensions, raise the power consumption of machine tools, cause tool wear and damage, result in an excessive deflection and breakage of the tool.

In orthogonal machining, various factors including cutting conditions (cutting speed and feed rate) and tool geometry (rake angle and edge radius) can affect machining characteristics and surface quality. In recent years, with the advent of HSM equipment, the aerospace industry is adopting HSM due to its merits over CM processes. However, in order to minimize the trial and error approach and mitigate the investment risks, it is of high importance to quantify the impact of various HSM processing on critical machining variables. Using FE models enables manufacturers to address the above concerns and predict the influence of machining conditions on characteristics such as cutting forces, temperature and chip morphology.

Yen *et al.* (2004) performed a finite element analysis based on an updated Lagrangian formulation using the DEFORM^{TM} software to examine the effect of tool edge geometry on machining characteristics in orthogonal machining of AISI 1020 steels. They found that increasing cutting edge radius slightly increased the chip thickness, whereas it had almost no effect on the magnitude of the maximum tool temperatures near the tool tip. Özel (2009) carried out FE simulations of orthogonal turning of Inconel 718 based on the modified Johnson-Cook material model using the DEFORM^{TM} software. They found that a larger tool edge radius

produced higher specific cutting forces and temperatures and a smaller edge radius with neutral rake angle resulted in lower forces and temperatures.

Wyen et Wegener (2010) experimentally studied the influence of cutting edge radius on cutting forces in machining titanium alloys and reported that the cutting and feed forces increased with raising cutting edge radius. Daoud *et al.* (2015) conducted research on the influence of the rake angle on cutting process parameters of Al2024-T3 alloy induced by orthogonal machining using the DEFORM^{TM} software. They reported that the cutting forces decreased by 55% with changing the rake angle from −8° to +8°.

Cheng *et al.* (2016) conducted a numerical study of orthogonal cutting Fe-Cr-Ni stainless steel using the AdvantEdge^{TM} software to analyze the machining characteristics in the workpiece and tool for different cutting edge and rake angle values. The results showed that the cutting edge radius had little and great effects on temperature and stress, respectively. In addition, the highest temperature in the tool gradually increased and the tool stress first decreased and then increased with the increase of the rake angle. Akram *et al.* (2016) numerically and experimentally investigated the effect of cutting speed and feed rate on the chip thickness of aluminum alloys 6061 produced by orthogonal machining operations. They concluded that the chip thickness diminished and increased with increasing cutting speed and feed rate, respectively.

Zhuang *et al.* (2018) developed a finite element model to study the influences of the chamfer length, chamfer angle and feed rate (uncut chip thickness) on the cutting forces in orthogonal cutting of Ti6Al4V and Inconel 718 using the AdvantEdge^{TM} software. A new calibration model for the edge coefficients was used to consider the effect of the chamfered edge and length to predict the edge force components. The results demonstrated that the chamfered length and angle had a considerable effect on the cutting forces. Reddy *et al.* (2018) conducted the FE simulation of the orthogonal turning of Ti6Al4V alloy using the AdvantEdge^{TM} software. The results showed that the tool edge radius had a considerable effect on cutting

forces and temperature. They also reported that when the cutting tool edge radius decreased, high thermal stress was observed on the cutting tool.

Emamian (2018) developed a FE model of orthogonal turning of AISI 1045 steel based on an updated Lagrangian approach using the Abaqus®/Explicit software. They found that the machining forces increased with the feed rate for various edge radii. Moreover, increasing the cutting edge radius led to a larger maximum cutting temperature except for the lowest feed rate. Patel (2018) carried out a numerical research on FE modeling of orthogonal turning of aluminum alloy AA2024-T351 using the Abaqus® software. The Johnson-Cook damage model and the Hillerborg's fracture model were used to consider damage initiation and damage evolution in the workpiece material, respectively. The results displayed that the average cutting force increased with increasing the feed rate (uncut chip thickness) and decreasing the tool rake angle. Moreover, the average cutting force decreased slightly with increase in the cutting speed. The cutting temperature in primary and secondary shear zones diminished when the tool rake angle was increased. It needs mentioning that the effect of tool cutting edge radius was not investigated in this study and the model was validated using the data available in the open literature.

Mir *et al.* (2018) performed the FE simulations in single point diamond turning of silicon based on the smoothed particle hydrodynamics approach and the Drucker-Prager material constitutive model using the Abaqus® software. The results indicated that the cutting force ratio first increased and then decreased for the rake angles from -25º to -30º and from -35º to -40º, respectively. Jiang et Wang (2019) carried out the finite element simulation to examine the performance of various wiper tool edge geometries in orthogonal machining of AISI 4340 steel. The cutting process was simulated based on Arbitrary- Lagrangian-Eulerian approach using the AdvantEdge™ software. The results demonstrated that the wiper tool reduced the temperature of the tool's flank face compared with the hone conventional tool, while it increased the temperature of the rake face and the cutting force.

The above overview of the previous studies shows that the impact of cutting edge radius on machining characteristics depend highly on work materials, cutting conditions, and tool geometry. Furthermore, little data is available on the interaction between the edge radius and cutting speed, rake angle, and feed rate and their influences on machining characteristics, especially in the range of high speed machining of aluminum alloys (Sadeghifar *et al.,* 2018a).

The main objective of the present research study is to assess the interaction between the cutting edge radius and cutting speed, rake angle, and feed rate and their impacts on machining characteristics in orthogonal high speed turning of aluminum alloy 6061-T6. Particularly, the influence of the cutting edge radius on the location and magnitude of maximum cutting temperature and chip thickness in high speed machining of aluminum alloy 6061-T6 will be studied. The influence of tool edge radius on machining performance between conventional machining and high speed machining will also be investigated in the present work to better illustrate the differences between the two techniques. To achieve these, the cutting speeds of 361, 650, 950 and 1250 m/min, the feed rates of 0.1, 0.16 and 0.2 mm/rev, the rake angles of -8^{o}, 0^{o,} and +8^{o}, and the cutting edge radii of 0.005, 0.01, 0.02, 0.03 and 0.04 mm will be considered. The first two cutting speeds lead to CM and the second two ones result in HSM.

4.3 Experimental tests

Dry orthogonal straight turning tests were carried out on a MAZAK CNC machine. The workpiece was a 150-mm diameter and 120-mm length cylinder made of aluminum alloy 6061-T6 and the tool was uncoated carbide (ISO CCGX 120408-AL H10). A right-hand tool holder of SCLCR 2020 K12 was employed to hold the inserts, as shown in Figure 4.1(a). A new insert was used for each machining experiment to provide similar conditions for all the tests. The workpiece components were groove machined to form tube-shaped samples with 4-mm thickness. The machining tests were carried out for the cutting conditions listed in Table 4.1 with the tool geometry including the edge radius of r_β=0.02 mm, the rake angle of γ_0= 17.5 degrees, and the clearance angle of α_0 = 7 degrees. Machining forces were measured using a Kistler (type 9121) three-component piezoelectric dynamometer. The acquisition of

force signals was conducted with a LabVIEW software and data treatment was performed using MATLAB codes. The chip thickness was measured using a digital micrometer by averaging the values of the chip thickness at three different locations far enough from the two ends of the chip. A HITACHI TM3000 Scanning Electron Microscope (SEM) was utilized to observe the chip shape. The experimental set-up of the orthogonal straight turning tests is displayed in Figure 4.1(b).

4.4 Finite element modeling

In the present study, Finite Element Method (FEM) was utilized to simulate the orthogonal straight turning of aluminum alloys 6061-T6 using the DEFORM^{TM} software. The mathematical formulation of the analysis is based on an updated Lagrangian formulation and implicit integration method for large plastic deformation analysis. In the present section, these formulations together with the characteristics of the developed FE model are described.

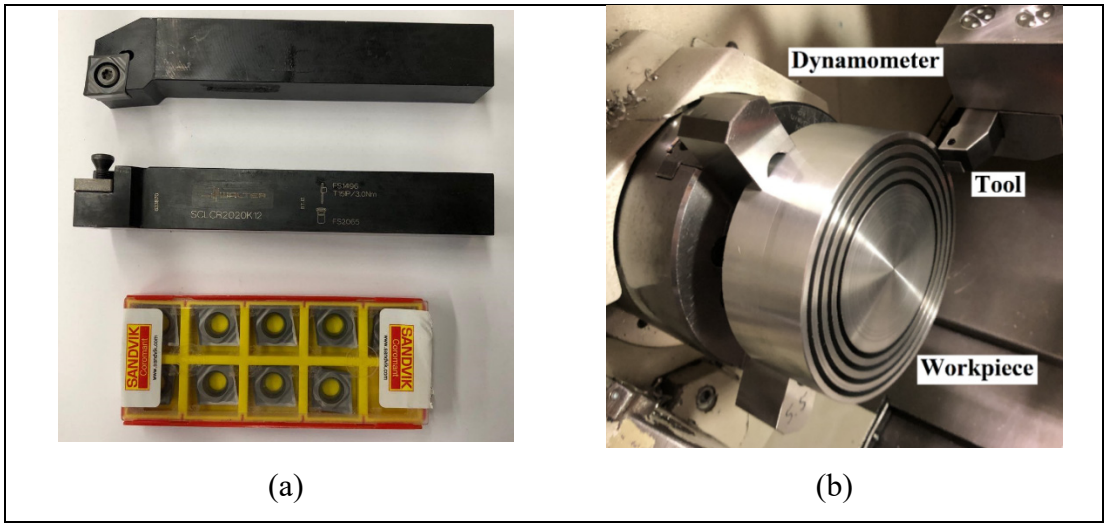

Figure 4.1 (a) The insert and toolholder and (b) the experimental set-up of orthogonal machining

Table 4.1 Cutting conditions for tool geometry including r_β=0.02 mm, γ_0=17.5°, and α_0=7°

Test No.	$V(m/\text{min})$	$f(mm/rev)$
1	361	0.16
2	650	0.16
3	950	0.16
4	1250	0.16
5	950	0.1
6	950	0.2

The equations of motion during cutting may be expressed at a specific instant of time as (Sadeghifar *et al.,* 2018b):

$$[M]\{\ddot{U}\} + \{R_{\text{int}}\} = \{R_{ext}\} \tag{4.1}$$

where $[M]$ is the mass matrix, $\{\ddot{U}\}$ is the acceleration vector ($\{U\}$ is the displacement), and $\{R_{\text{int}}\}$ and $\{R_{ext}\}$ are the vectors of internal and external forces, respectively. The effect of damping is ignored, and consequently, $\{R_{\text{int}}\}$ is equal to:

$$\{R_{\text{int}}\} = [C_d]\{\dot{U}\} + [K_s]\{U\} \cong [K_s]\{U\} \text{ where } [C_d] \cong 0 \tag{4.2}$$

where $[C_d]$ and $[K_s]$ are the damping and stiffness matrices, respectively. In addition, $\{R_{ext}\}$ involves the external forces applied during cutting including the reaction forces at the supports.

Heat transfer occurring during the machining process is described as (Sadeghifar *et al.,* 2018b):

$$[C_T]\{\dot{T}\} + [K_T]\{T\} = \{\dot{Q}_g\} \tag{4.3}$$

in which $[C_T]$ and $[K_T]$ are the volumetric heat capacitance and thermal conduction matrices, respectively. Also, $\{\dot{Q}_g\}$ is the total heat generation in the machining process.

The thermal contact between the tool and workpiece is defined using the heat conduction through the tool-chip contact face from the chip to the tool during the cutting process which is calculated as:

$$Q = h_{\text{int}} (T_{wp} - T_t) \tag{4.4}$$

where h_{int} is heat transfer coefficient, T_{wp} and T_t are the workpiece and tool's temperature at the tool-chip interface. In the current research, a heat transfer coefficient of 10^7 $W/m^2\ ^oC$ was calibrated for modeling and an initial temperature of 20 °C (room temperature) was applied to both tool and workpiece.

The convection heat transfer takes place between the workpiece surface and the ambient according to the following formulae (Sadeghifar *et al.,* 2018b):

$$Q = h\ (T_{wp} - T_a) \tag{4.5}$$

in which h is convection heat transfer coefficient, and T_{wp} and T_a are the workpiece and ambient (room) temperature. In the present work, h was chosen as 20 $W/m^2\ ^oC$.

It is known that the material models used in finite element modeling of machining processes cannot be identified using quasi-static tests. This is because the workpiece material undergoes high strain, strain rate, and temperature during machining. Several material constitutive models were commonly used in FE simulations of cutting such as Johnson-Cook, Zerilli-Armstrong, and Marusich models. The Johnson-Cook material constitutive model has been extensively used in machining simulations and it was proved to be appropriate in modeling the machining processes (Miguélez *et al.,* 2013; Chen *et al.,* 2015).

In addition, the Johnson-Cook constitutive equation was used for modeling plastic deformation of the workpiece material as follows:

$$\bar{\sigma} = [A + B(\varepsilon)^n]\left[1 + C\ln\left(\frac{\dot{\varepsilon}}{\dot{\varepsilon}_0}\right)\right]\left[1 - \left(\frac{T - T_{room}}{T_{melt} - T_{room}}\right)^m\right] \quad (4.6)$$

where ε is the plastic strain, $\dot{\varepsilon}$ the plastic strain rate (s^{-1}), $\dot{\varepsilon}_0$ the reference plastic strain rate (s^{-1}), $T(^oC)$ the workpiece temperature, $T_{melt}(^oC)$ the melting temperature of the workpiece, and $T_{room}(^oC)$ the room temperature. Also, $A\ (MPa)$ is the initial yield strength, $B\ (MPa)$ the hardening modulus, C the strain rate sensitivity coefficient, n the hardening coefficient, and m the thermal softening coefficient. Table 4.2 lists the Johnson-Cook constants of aluminum alloy 6061-T6.

Table 4.2 The constants of Johnson-Cook material model of aluminum alloy 6061-T6 (Daoud *et al*., 2014)

$A\ (MPa)$	$B\ (MPa)$	n	C	m	$\dot{\varepsilon}_0\ (1/s)$	$T_{melt}(^oC)$	$T_{room}(^oC)$
250	79.70	0.499	0.0249	1.499	1	652	20

Modeling of frictional behavior at the tool-workpiece contact areas is a great challenge in finite element simulations of metal cutting processes. Three main frictional models commonly used in FE modeling of machining processes are presented in Table 4.3. The Coulomb friction model represents the relation between frictional stress τ and normal stress σ_n. The constant shear friction model assumes that the frictional stress on the rake face of the tool is proportional to the shear yield stress of the workpiece. The Zorev model estimates the friction at the tool-chip interface using constant shear friction model in sticking region and constant Coulomb friction model in sliding region.

Previous research shows that aluminum alloys are prone to adhering to the tool at the tool-chip interface during cutting (Roy *et al.*, 2009), which indicates a sticking zone. The Coulomb and Zorev models are not capable of predicting precisely since there is no relative sliding at the tool-chip interface. As a result, the shear friction model with a constant coefficient between 0.8 and 0.9 was utilized in the present research study. Based on the difficulty and inaccuracy of friction coefficient measurements, this coefficient was often determined by calibrating the

FE model based on comparing and matching the FE results with the corresponding experimental ones.

Table 4.3 Friction models frequently employed in FE simulations of machining processes (Sadeghifar *et al.*, 2013)

Model	Formulae[1]
Coulomb friction model: Constant Coulomb friction coefficient at the entire tool-chip interface	$\tau = \mu\sigma_n$
Shear friction model: Constant shear friction coefficient at the entire tool-chip interface	$\tau = m\tau_Y$
Zorev model: Constant shear friction coefficient in sticking region and constant Coulomb friction coefficient in sliding region	$\tau = \tau_Y$ when $\mu\sigma_n \geq \tau_Y, 0 < x \leq l_p$ $\tau = \mu\sigma_n$ when $\mu\sigma_n < \tau_Y, l_p < x \leq l_c$

[1] τ is shear stress, m shear friction factor, μ Coulomb friction coefficient, σ_n normal compressive stress, τ_Y shear flow stress, l_p and $l_c - l_p$ are the lengths of the sticking and sliding regions

For the simulation purposes, a 4.75 mm × 1.12 mm rectangle workpiece with an elastic-plastic behavior was considered. The workpiece was meshed with 6000 linear quadrilateral elements. The tool material was considered as a rigid body and was meshed with 1700 elements. Figure 4.2 illustrates the tool and workpiece's geometries. The workpiece and tool's material properties are given in Table 4.4. Figure 4.3 shows the boundary conditions (BCs) defined for the workpiece and the tool. In both horizontal and

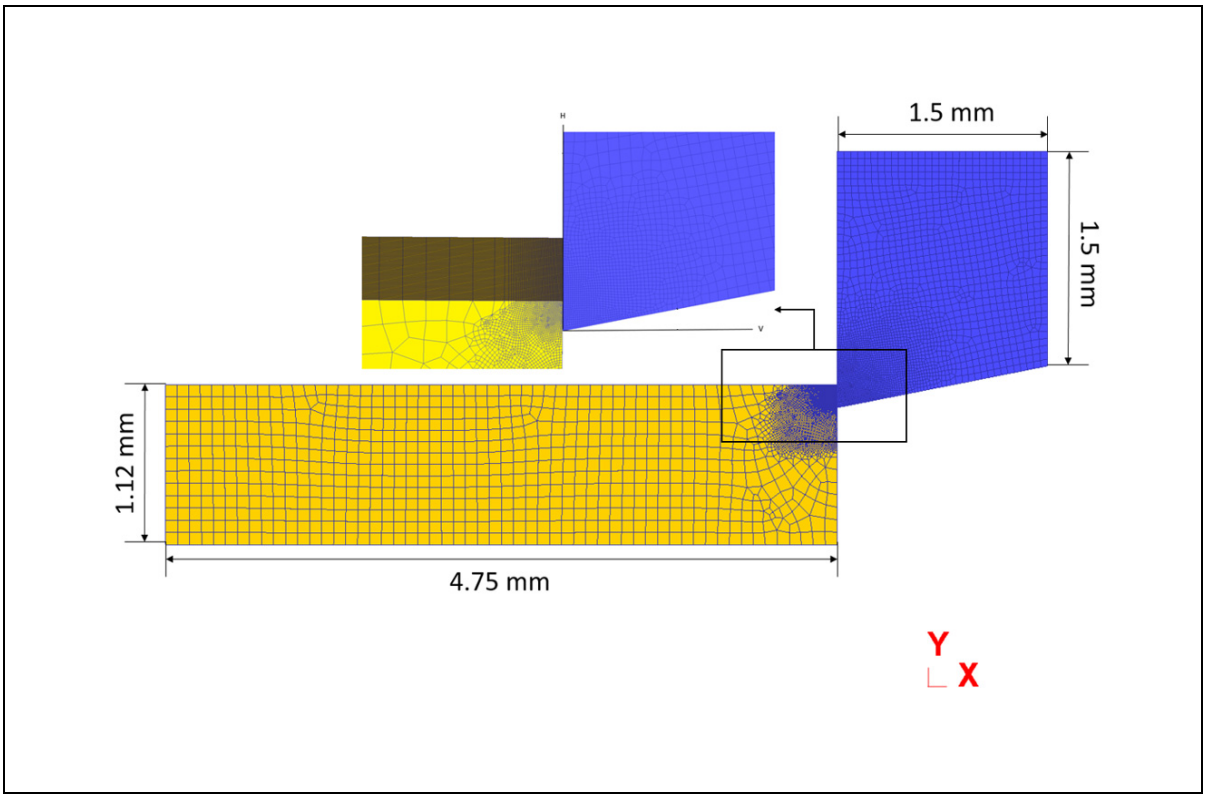

Figure 4.2 The geometry and dimensions of the tool and workpiece in FE modeling

Table 4.4 Mechanical and thermal properties of the workpiece and tool (Daoud *et al.*, 2015)

Properties	AA6061-T6	Uncoated carbide
Density $\rho\ (kg/m^3)$	2700	11900
Young's modulus $E\ (GPa)$	58.5	612
Poisson's ratio υ	0.33	0.22
Conductivity $k\ (W/m\ ^oC)$	167	86
Specific heat capacity $c\ (J/kg\ ^oC)$	896	337
Thermal expansion coefficient $\alpha\ (1/\ ^oC)$	23.5×10^{-6}	4.9×10^{-6}

vertical directions, the top and right sides of the cutting tool are fixed ($\boldsymbol{V_x = 0}$ and $\boldsymbol{V_y = 0}$, respectively). In addition, the bottom and left sides of the workpiece are fixed just in vertical direction ($\boldsymbol{V_y = 0}$). The workpiece material moves through the fixed tool in the horizontal direction with a determined feed rate. The sides of the workpiece and tool which are far from

the cutting zone and are retained at ambient temperature ($\boldsymbol{T_{room}}$) of 20°C. Finally, continuous chip formation was assumed for all the simulations. This assumption can be justified based on the experimental observations of chips for all the selected cutting conditions. The simulations were performed using a computer system of Intel® Xeon® CPU E3-1225 V5 with a CPU speed of 3.30 GHz and a memory RAM of 64.0 GB.

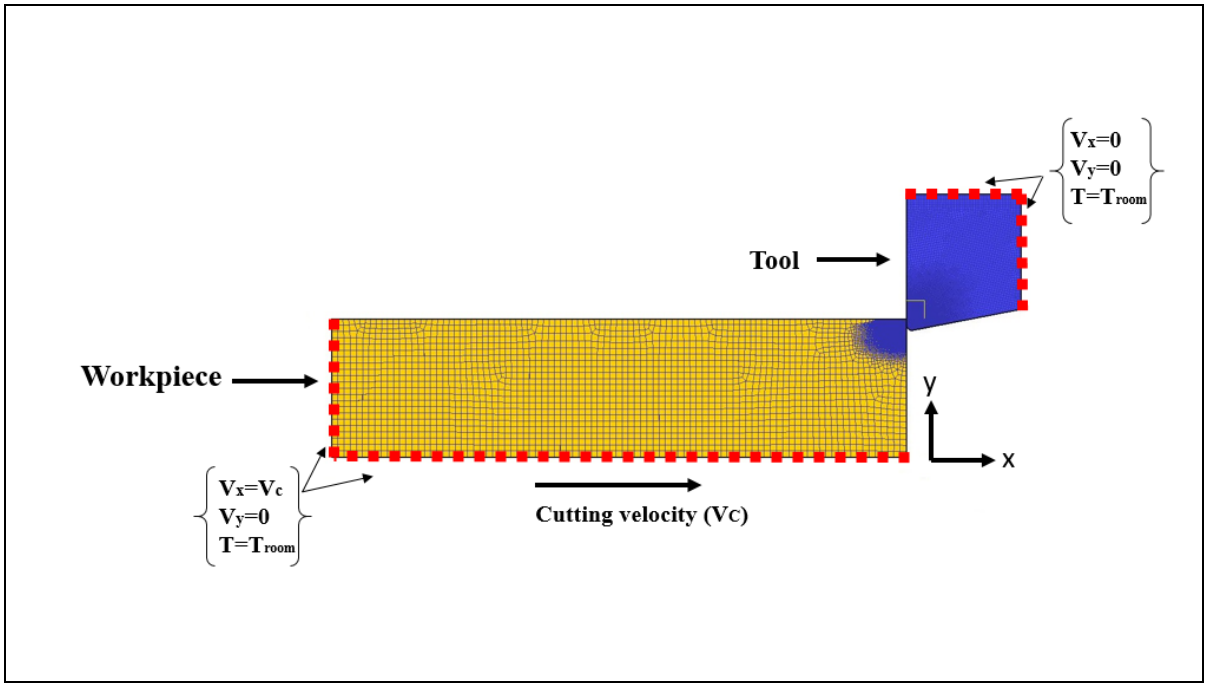

Figure 4.3 The thermal and mechanical boundary conditions of the workpiece and tool

4.5 Validation of the FE model

The developed finite element model is validated by comparing the present numerical results of chip thickness (t_c), cutting force (F_c), and thrust force (F_t) with those obtained through above-mentioned experimental tests. The predicted and experimental chip thicknesses are compared in Figure 4.4(a) and good agreement is observed. Also, as shown in Figure 4.4(b), the simulated and measured cutting and thrust forces are well matched. For instance, for Test No. 5, Figure 4.5 shows the distribution of cutting temperature in the workpiece and tool, where the steady-state condition is realized. Also, the experimental and simulated chip shapes for this test are both continuous as displayed in Figure 4.6(a) and Figure 4.6(b). In addition, the machining

forces for Test No. 5 are compared in Figure 4.7(a), Figure 4.7(b), and Figure 4.7(c). As observed, there exists a good agreement between the experimental and FE results. This was achieved by exploring different values of the shear friction coefficient and the heat transfer coefficient, and selecting appropriate coefficients using calibration of the FE results with the experimental ones. Moreover, mesh windows were assigned to the workpiece and the tool in order to have a high-quality fine mesh in the machined workpiece's surface and near-surface.

The validity of the developed FE model is additionally verified using the orthogonal cutting tests by Daoud *et al.* (2014), whose machining conditions are given in Table 4.5. In (Daoud *et al.,* 2014), the same workpiece and tool's materials as those of the present study were utilized while different tool geometry parameters were used. As shown in Figure 4.8(a) and Figure 4.8(b), the present FE results are in good agreement with the experimental ones presented in (Daoud *et al.,* 2014). Previous research study (Filice *et al.,* 2007) showed that the discrepancy between the simulated and measured thrust forces is unavoidable due to a lack of accurate friction and material constitutive models.

It should be emphasized that the developed FE model is validated with the present experiments for different cutting conditions including cutting speeds and feed rates and fixed tool geometry parameters (Figure 4.4). To verify the correctness of the FE model for different tool geometry parameters, the predicted machining forces and chip thicknesses are compared with the previous experimental ones for additional tool geometry parameters including tool edge radius, rake angle, and clearance angle (Figure 4.8(a) and Figure 4.8(b)).

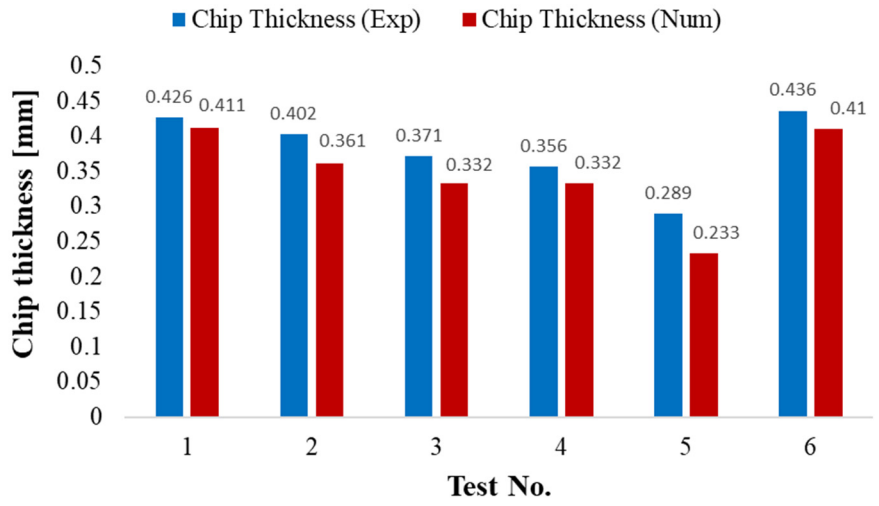

(a)

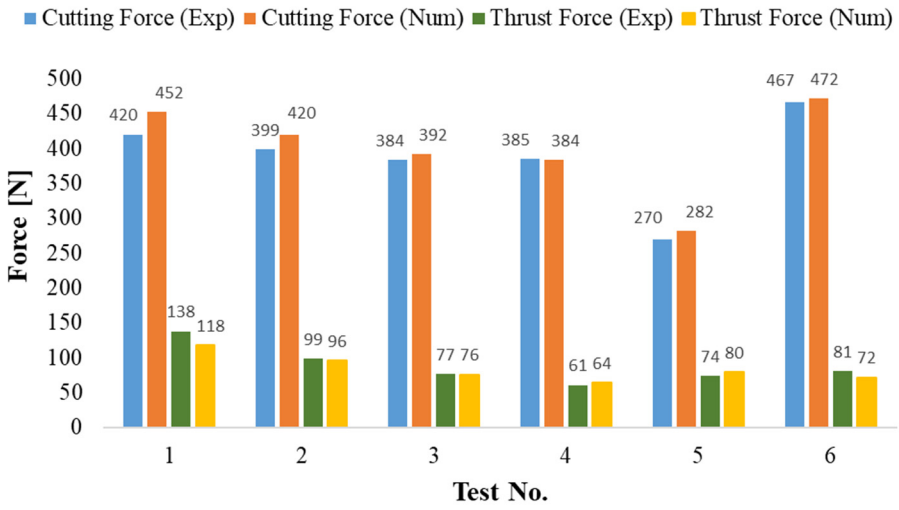

(b)

Figure 4.4 Validation of the FE results of (a) chip thickness and (b) machining forces with the experimental ones

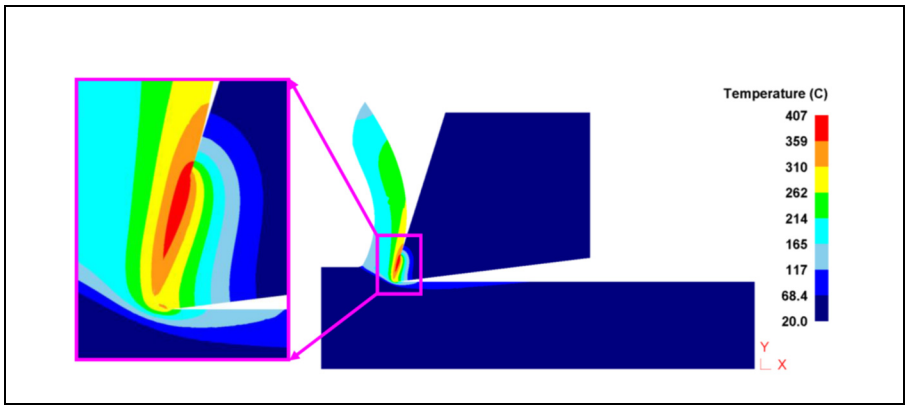

Figure 4.5 The distribution of cutting temperature in the workpiece and tool for steady-state condition

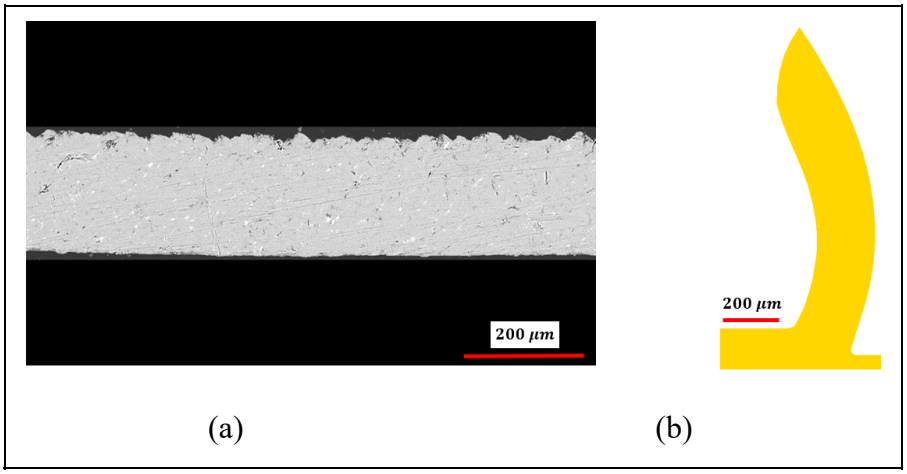

Figure 4.6 A comparison of (a) experimentally observed and (b) numerically simulated chip shapes

Table 4.5 Cutting conditions and tool geometry (Daoud *et al.*, 2014)

Test No.	Cutting speed $V(m/\text{min})$	Feed rate $f(mm/rev)$	Edge radius $r_\beta(mm)$	Rake angle $\gamma_0(\text{deg})$	Clearance angle $\alpha_0(\text{deg})$
1	361	0.16	0.005	0	11
2	650	0.16	0.005	0	11
3	950	0.16	0.005	0	11
4	1250	0.16	0.005	0	11
5	950	0.16	0.005	-8	11
6	950	0.16	0.005	+8	11
7	950	0.1	0.005	0	11
8	950	0.2	0.005	0	11

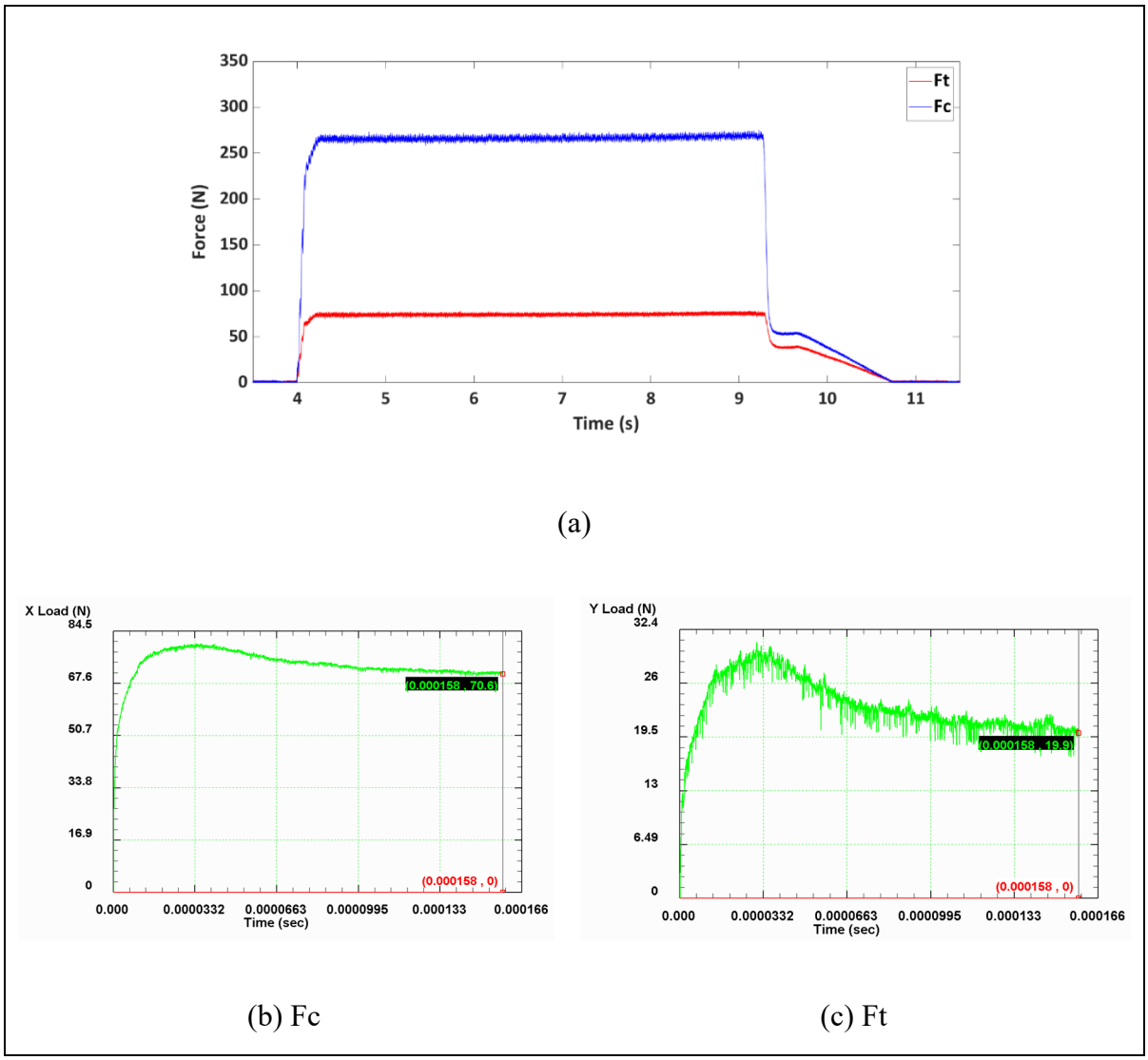

Figure 4.7 Variation of cutting and thrust forces with time during the cutting process: (a) In the experiment (force signals) for the 4-mm width of cut and (b,c) in FE modeling for the unit width of cut

4.6 Results and discussion

4.6.1 Interaction between cutting speed and cutting edge radius

Figure 4.9 illustrates the tool's cutting edge and different edge radii utilized in this research. Machining forces decrease or remain almost constant with increasing the cutting speed, as seen in Figure 4.10 and Figure 4.11. Specifically, there is a large reduction in both cutting and feed

forces from the cutting speed of 361 m/min to other higher speeds. This can be attributed to the resultant of two facts. The first fact is that a higher cutting speed generates larger frictional and plastic works, yielding more thermal softening, and as a result, produces smaller cutting forces during machining (Ucun et Aslantas, 2014). In contrast, the second fact is that a high cutting speed causes a greater material removal rate, leading to a lower cutting temperature and larger cutting forces (Pawade *et al.* 2008). In a cutting process, the contribution of the first above-mentioned fact is greater than or almost equal to that of the second one, depending on the range in which the magnitude of the cutting speed changes (Sadeghifar *et al.,* 2018b). Specifically, as observed in Figure 4.10 and Figure 4.11, the effect of the cutting speed on the machining forces is smaller at higher cutting speeds of 950 and 1250 m/min, demonstrating that machining forces are more dependent on the cutting speed in CM than in HSM.

Machining forces increase with raising the cutting edge radius for all the four cutting speeds considered. The variations of the cutting and feed forces with the edge radius are linearly approximated as displayed in Figure 4.10 and Figure 4.11. Fitting linear regression models to the results assists to compare the variation's trends in responses more easily and efficiently. As observed in Figure 4.10 and Figure 4.11, the slope of the linear model at the cutting speed of 361 m/min is much higher for both cutting and feed forces (the slope is 1880 and 2842 for cutting and feed forces, respectively). This shows that both cutting and feed forces are more sensitive to the cutting edge radius at low cutting speeds which fall into CM. On the other hand, the slopes of the linear models of variations of the feed forces are larger than those of variations of the cutting forces. This reveals that the increase in the feed force is much larger than that in the cutting force for all the cutting speeds when the cutting edge radius is increased.

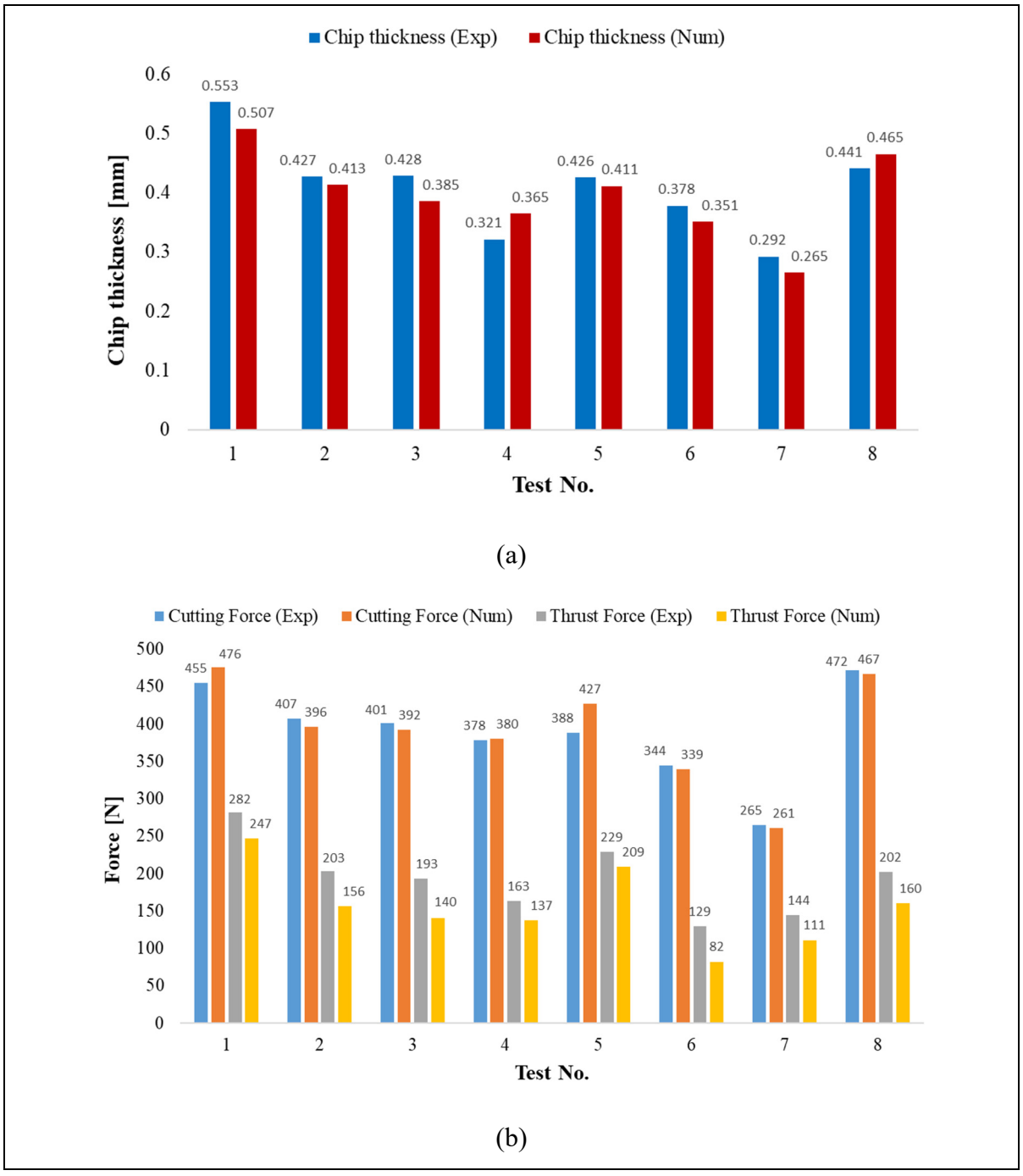

Figure 4.8 Verification of the validity of the present FE results of: (a) chip thickness and (b) machining forces with the previously published experimental ones (Daoud *et al.*, 2014)

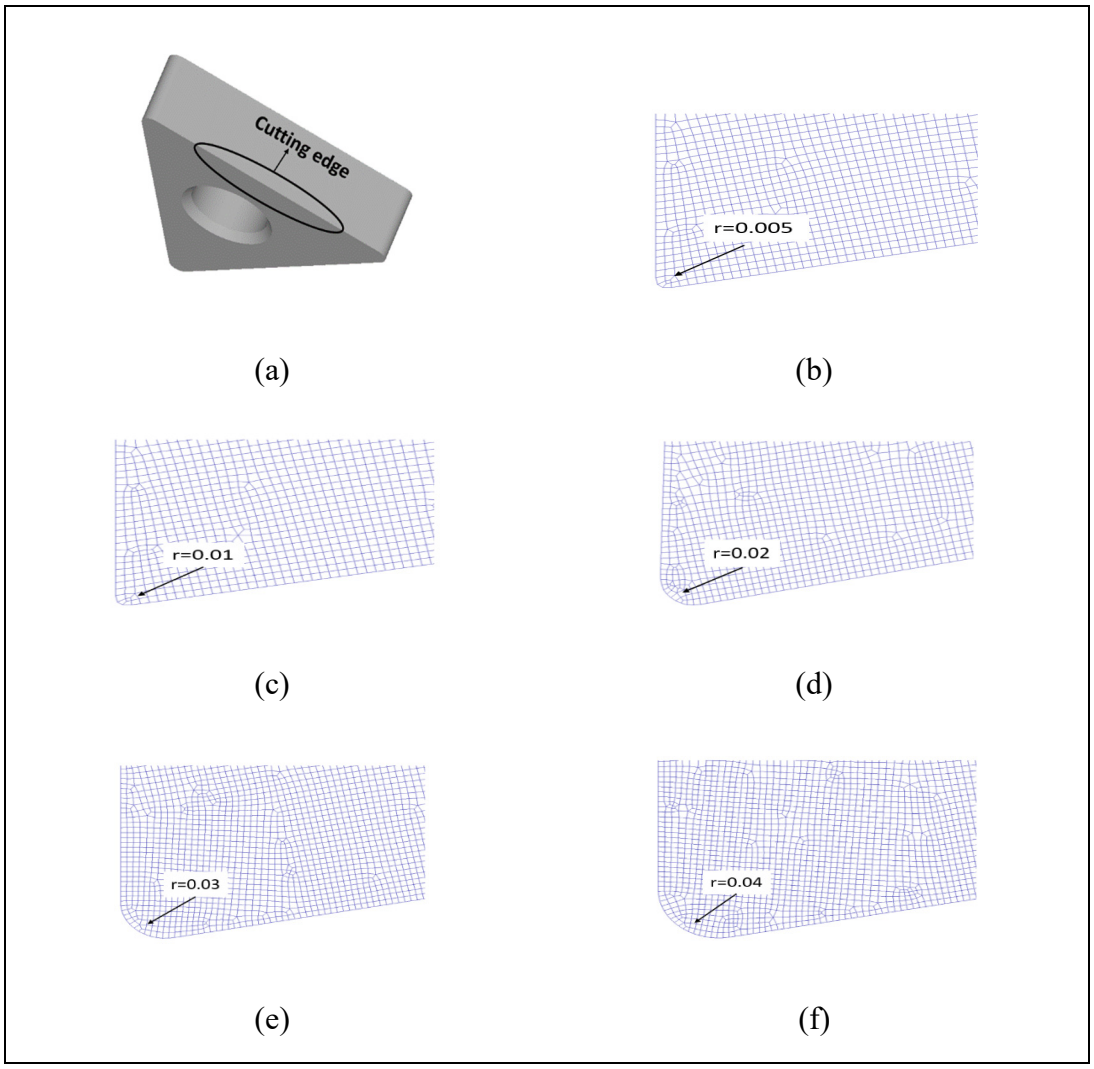

Figure 4.9 The tool's cutting edge and different edge radii (in terms of mm)

The influences of cutting speed and cutting edge radius on cutting temperature are displayed in Figure 4.12 and Figure 4.13, where it can be seen that both the maximum temperature which occurs at the tool rake face (as shown in Figure 4.5) and the average temperature of the tool tip rise with the cutting speed. This is due to the fact that a larger cutting speed generates higher frictional and plastic works, leading to higher temperatures, as mentioned previously.

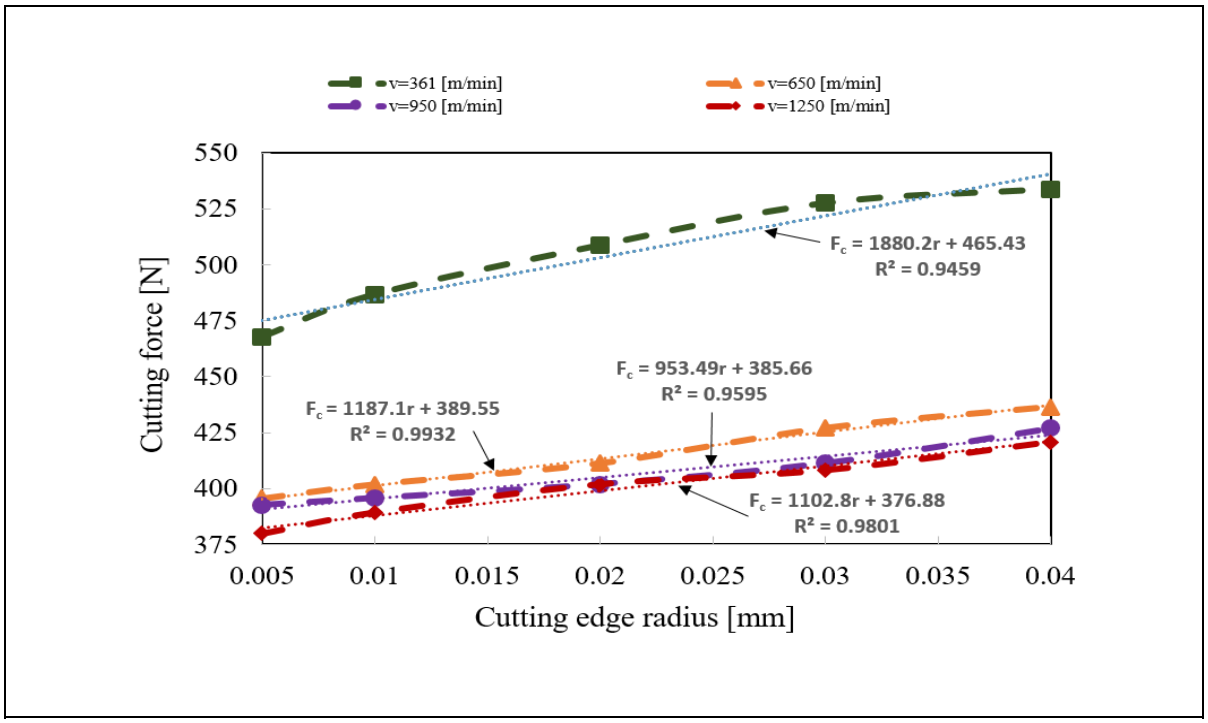

Figure 4.10 The effect of cutting edge radius and cutting speed on cutting force

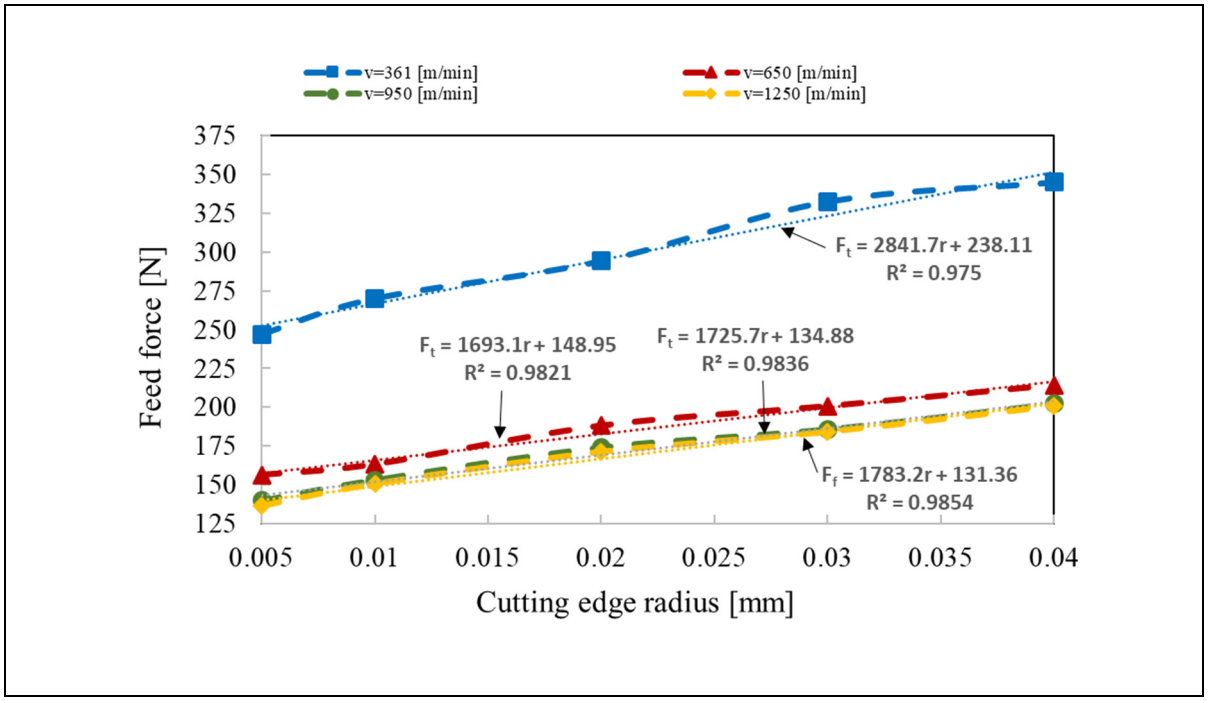

Figure 4.11 The effect of cutting edge radius and cutting speed on feed force

On the other hand, at low cutting speeds (361 and 650 m/min) which fall into CM, there are almost no differences between the magnitudes of the average temperature of the tool tip. By contrast, at high cutting speeds (950 and 1250 m/min) corresponding to HSM conditions, there are larger differences between the values of the average temperature of the tool tip. This shows that the influence of the cutting speed on the average temperature of the tool tip increases with raising the cutting speed. It must be mentioned that linear regression models for the maximum cutting temperatures are not provided here as these temperatures remain nearly constant with increasing the tool edge radius for all the cutting speeds under study, as seen in Figure 4.12. In contrast, as viewed in Figure 4.13, the average temperatures of the tool tip increase with the edge radius. This is better illustrated at the high speeds of 950 and 1250 m/min, in which the slopes of the linear models are higher than those related to the cutting speeds of 361 and 650 m/min. It is interesting to note that these results can be compared with those reported by Yen *et al.* (2004), Özel et Zeren (2007), and Al-Zkeri *et al.* (2009), who examined the impact of the tool edge radius on cutting temperature.

The orthogonal cutting of AISI 1020 steel with uncoated carbide, AISI 4340 steel with uncoated carbide, and AISI 4142H steel with TiAlN-coated carbide was analyzed by Yen *et al.* (2004), Özel et Zeren (2007), and Al-Zkeri *et al.* (2009), respectively. According to the results of Yen *et al.* (2004), the maximum temperature in cutting of AISI 1020 steel took place at the tool tip, as shown in Figure 4.14(a), contrary to the present results for aluminum alloys AA6061-T6. In contrast, based on the results reported by Özel et Zeren (2007), and Al-Zkeri *et al.* (2009), as displayed in Figure 4.14(b) and Figure 4.14(c), the maximum temperature in cutting of AISI 4340 steel and AISI 4142H steel occurred on the tool rake face, which is in agreement with the present results for aluminum alloys AA6061-T6. Also, the temperature of the tool tip in machining of AISI 1020 steel was not sensitive to the size of the edge radius (Yen *et al.,* 2004), while the temperature of the tool rake face increased with raising the edge radius, opposite to the present results for aluminum alloys AA6061-T6. On the other hand, the tool rake face's temperature was not sensitive to the size of the edge radius in machining AISI 4340 steel (Özel et Zeren, 2007), being in excellent agreement with the results for aluminum alloy AA6061-T6. In machining AISI 4142H steel, the temperature of the tool rake face slightly

rose with raising the edge radius. These comparisons demonstrate that the location of the maximum cutting temperature and the sensitivity of the maximum cutting temperature to the cutting edge radius in metal cutting depend more on cutting conditions and tool geometry than workpiece and tool materials.

The effects of cutting speed and cutting edge radius on chip thickness were also investigated. As shown in Figure 4.15, the chip thickness decreases when the cutting speed increases. This is because increasing the cutting speed increases the shear angle, and consequently, diminishes the chip thickness. Similar to the behaviors of the cutting and feed forces against the cutting speed, the influence of the cutting speed on the chip thickness is smaller at higher cutting speeds of 950 and 1250 m/min, which demonstrates that the chip thickness is more affected by the cutting speed in CM than in HSM. On the other hand, as seen in Figure 4.15, the variation of the chip thickness with the cutting edge radius is not significant especially under HSM conditions, and as a result, linear regression models fitting the chip thickness' results are not presented. Also, in CM, the magnitudes of the chip thickness are generally higher at larger edge radii.

4.6.2 Interaction between rake angle and cutting edge radius

The combined effects of rake angle and cutting edge radius on machining forces are shown in Figure 4.16 and Figure 4.17. It can be seen that the machining forces are strongly affected by the rake angle. The change in the rake angle from negative to positive values leads to reduced machining forces for all the cutting edge radii considered. This can be attributed to the reduction in the tool-chip contact pressure and friction when the rake angle changes from -8^{o} to +8^{o}. Also, as viewed in Figure 4.16 and Figure 4.17, with raising the cutting edge radius, machining forces increase for all the three rake angles. More specifically, the slope of the linear model at the rake angle of -8^{o} is larger for both cutting and feed forces (the slope is in turn 1421 and 2390 for cutting and feed forces), demonstrating that both cutting and feed forces are more sensitive to the cutting edge radius at a negative rake angle. Also, similar to the results

obtained for the cutting speed, the percentage increase in the feed force is much larger than that in the cutting force for all the rake angles when the cutting

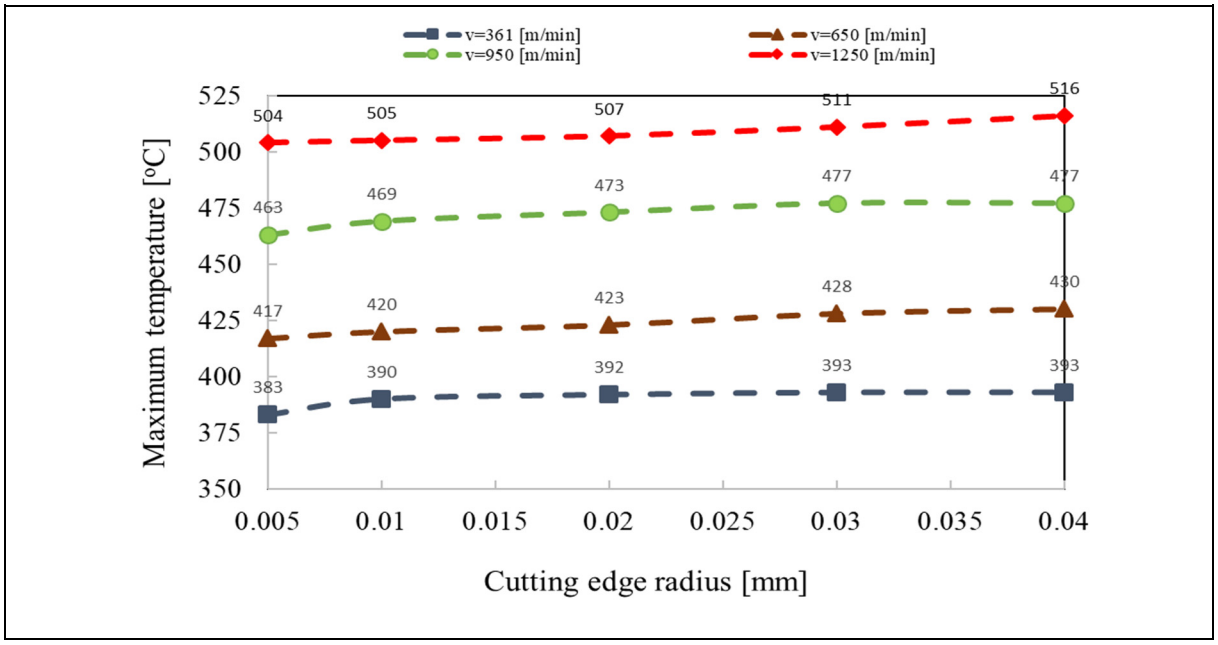

Figure 4.12 The influence of cutting edge radius and cutting velocity on maximum cutting temperature

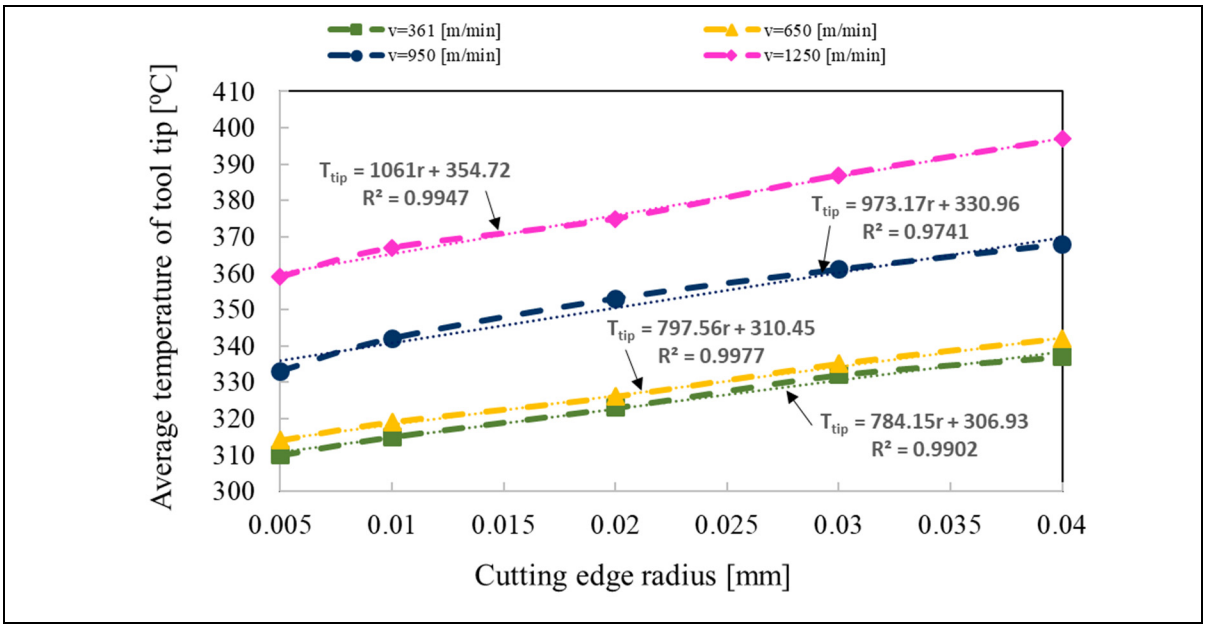

Figure 4.13 The influence of cutting edge radius and cutting velocity on the average temperature of tool tip

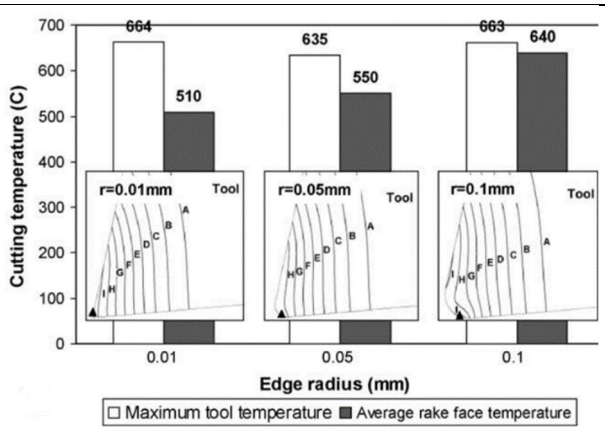

(a)

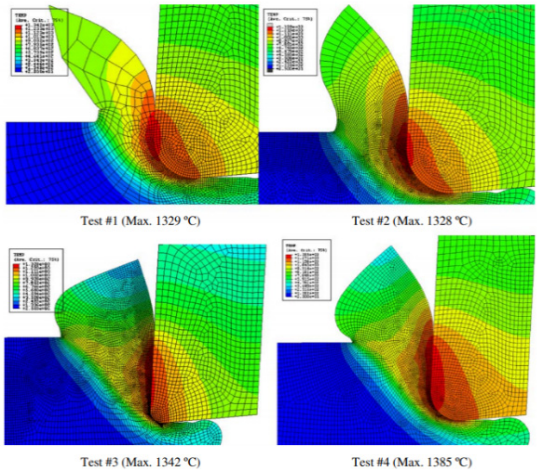

(b)

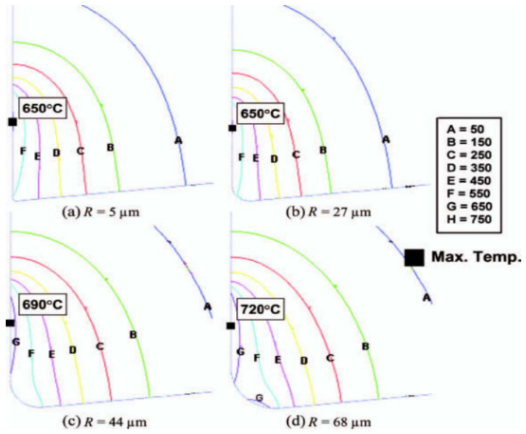

(c)

Figure 4.14 The influence of the cutting edge radius on the cutting temperature in cutting of (a) AISI 1020 steel (Yen *et al.*, 2004), (b) AISI 4340 steel (Özel et Zeren, 2007), and (c) AISI 4142H steel (Al-Zkeri *et al.*, 2009)

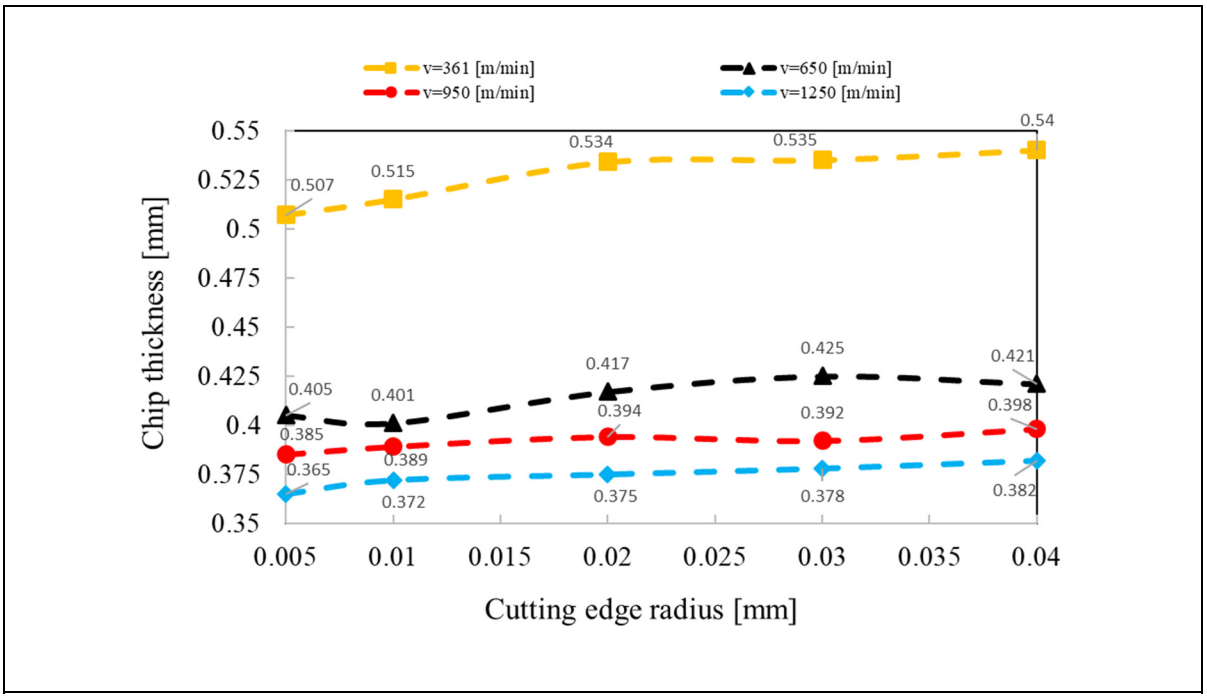

Figure 4.15 The impact of cutting edge radius and cutting velocity on chip thickness

edge radius is increased as the slopes of the linear models are much higher for the feed force compared with those for the cutting force.

The impacts of rake angle and cutting edge radius on cutting temperature are analyzed. As viewed in Figure 4.18 and Figure 4.19, both the maximum temperature occurring at the tool rake face and the average temperature of the tool tip decrease when the rake angle changes from negative to positive values for all the cutting edge radii under study. This reduction in the temperature can be attributed to the decrease in the tool-chip contact pressure and friction when the rake angle changes from -8º to +8º. Moreover, as seen in Figure 4.18 and Figure 4.19, for all the three rake angles under consideration, both the maximum temperature and the average temperature of the tool tip generally increase with increasing the cutting edge radius as also shown by the slopes of the linear models fitting the curves of the cutting temperature.

The effects of rake angle and cutting edge radius on chip thickness are illustrated in Figure 4.20. The chip thickness decreases when the rake angle changes from negative to positive values for all the cutting edge radii under study. It is interesting to note that the variation of the

chip thickness with the cutting edge radius is very small, concluding that the edge radius has a minor effect on the chip thickness.

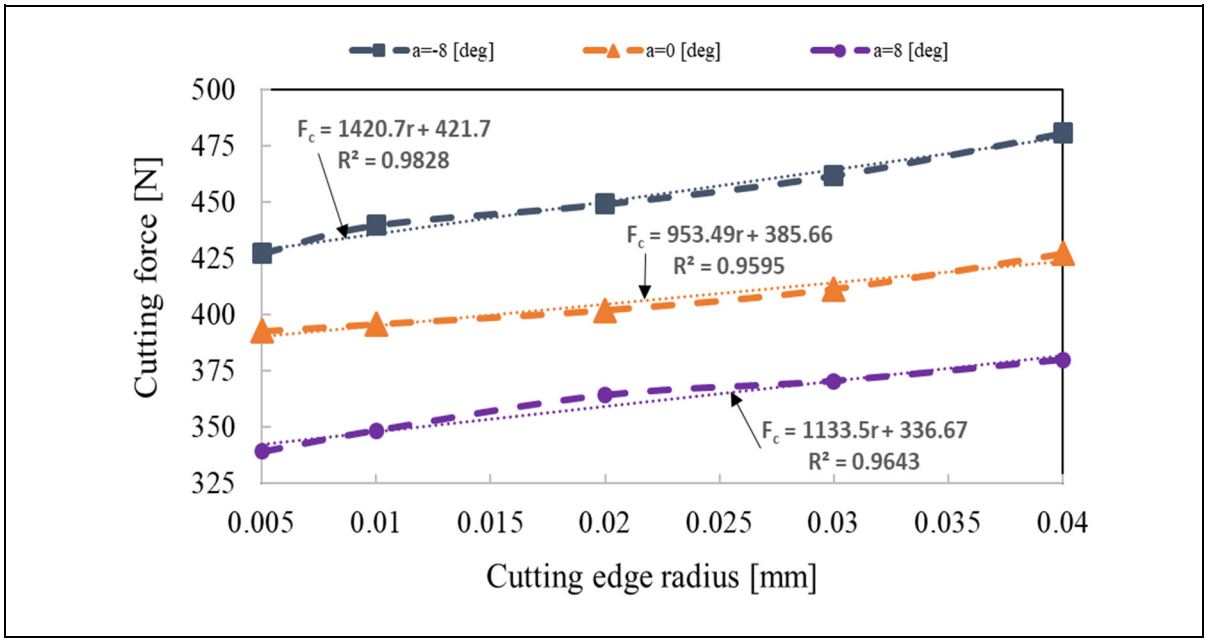

Figure 4.16 The effect of cutting edge radius and rake angle on cutting force

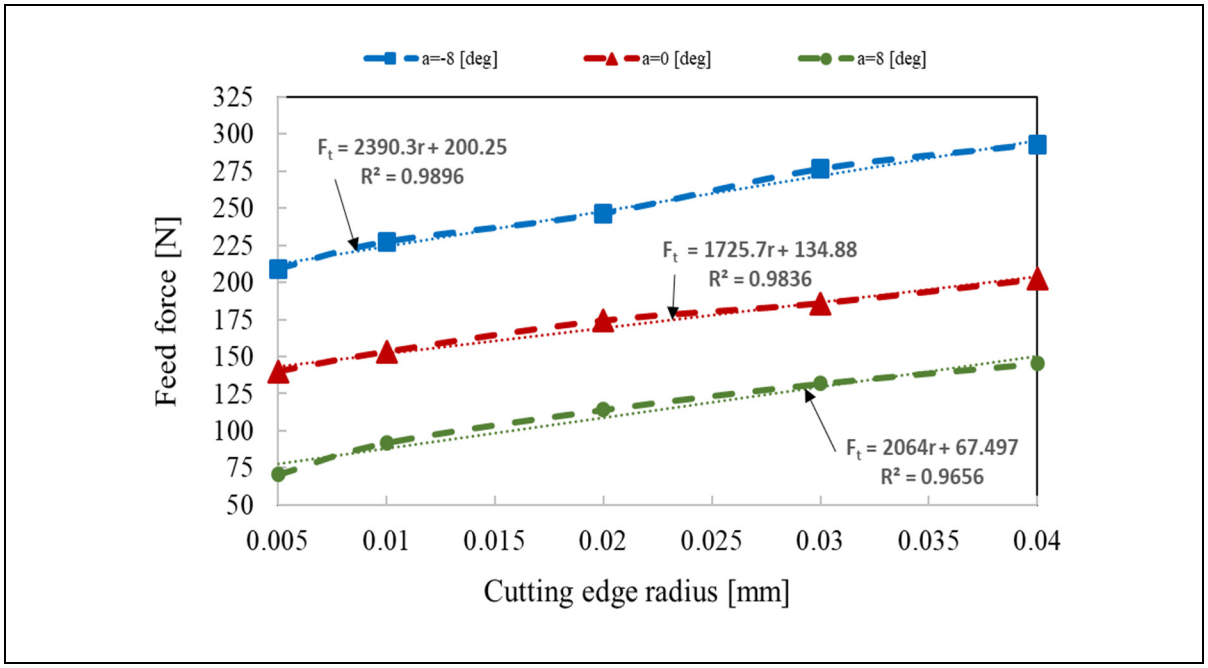

Figure 4.17 The effect of cutting edge radius and rake angle on feed force

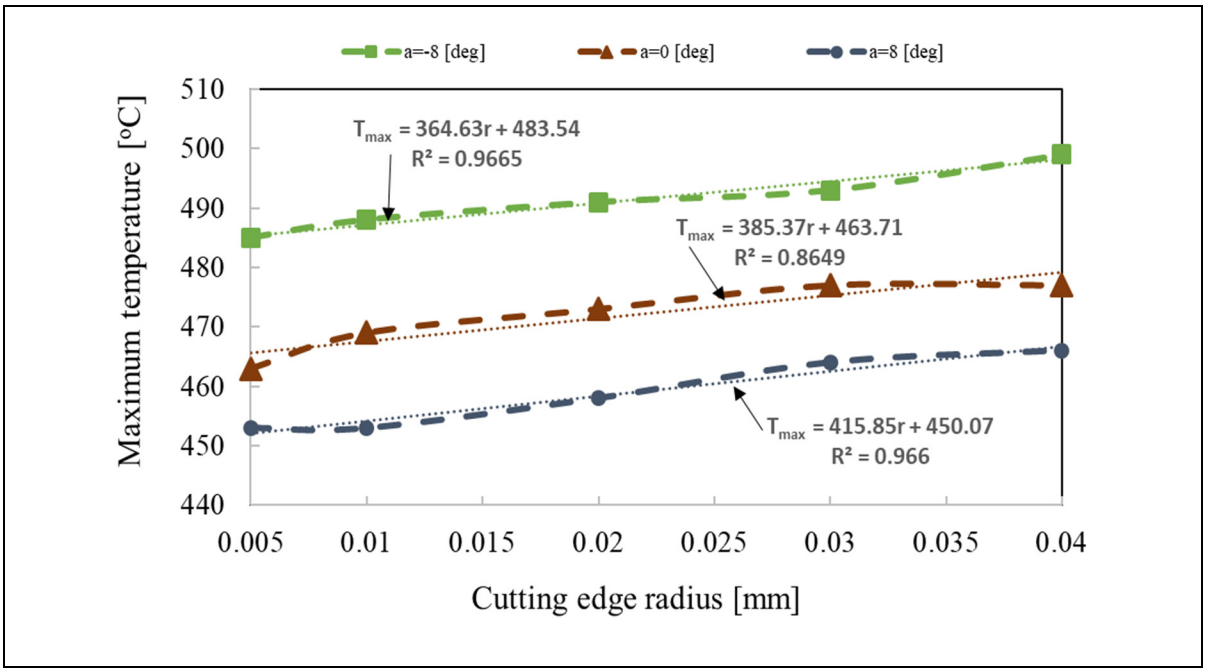

Figure 4.18 The influence of cutting edge radius and rake angle on maximum temperature

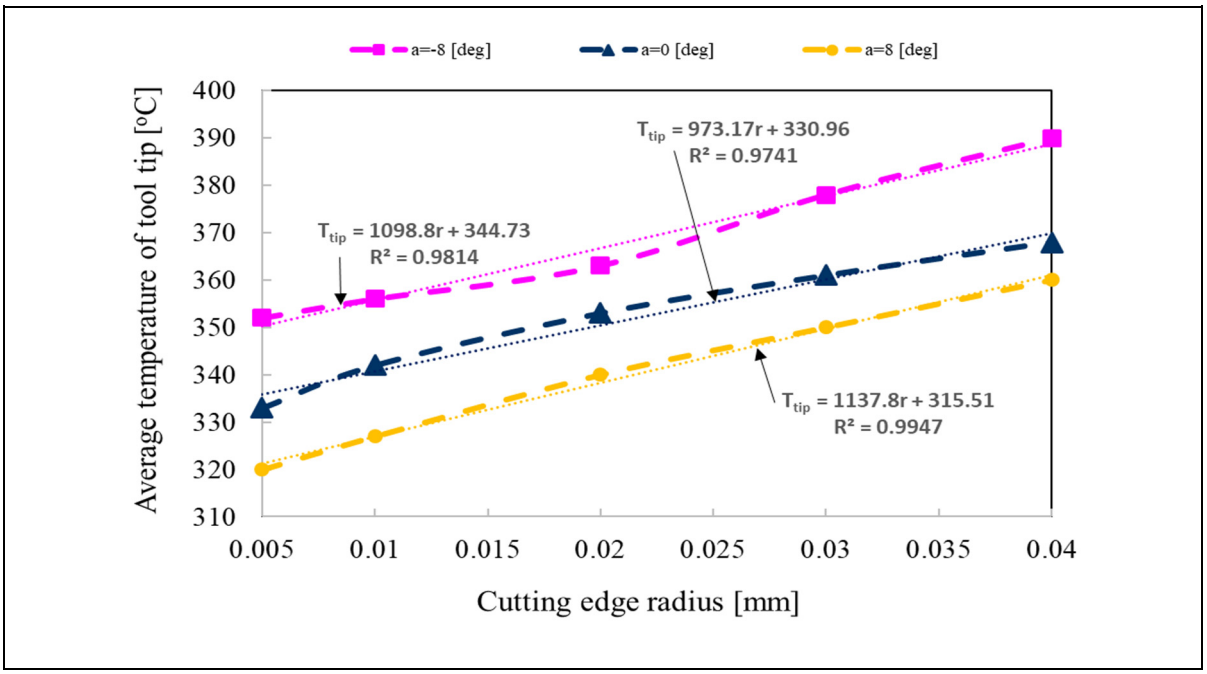

Figure 4.19 The influence of cutting edge radius and rake angle on the average temperature of tool tip

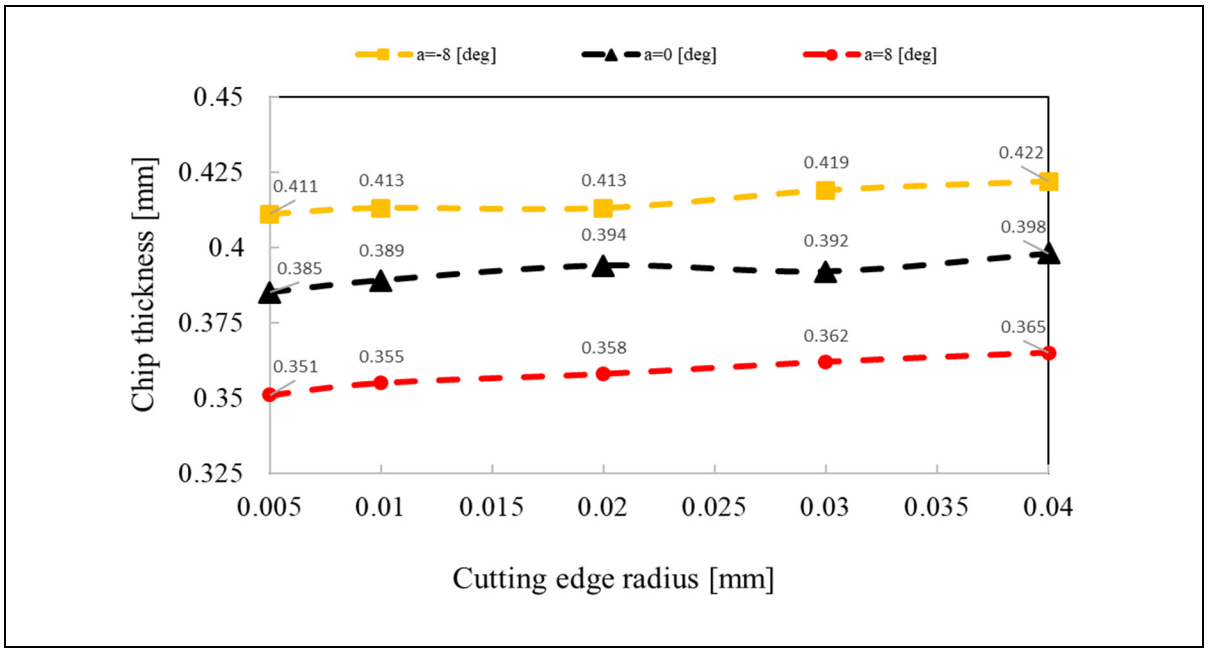

Figure 4.20 The effect of cutting edge radius and rake angle on chip thickness

4.6.3 Interaction between feed rate and cutting edge radius

Figure 4.21 and Figure 4.22 show that at constant edge radius, the machining forces increase with raising the feed rate. These results are in agreement with those reported by Sadeghifar *et al.* (2018b), who reported that an increment in the feed rate increases the tool-chip contact area and directly raises the machining forces in cutting 300M steel. By contrast, a rise in the feed rate may indirectly reduce the cutting forces due to an increase in the frictional area, which produces more heat and softens the material (Sadeghifar *et al.,* 2018b). In the cutting conditions considered herein, the contribution of the increase in the tool-chip contact area is larger than that of the increase in the frictional area, and as a result, the machining forces increase with the feed rate. Also, as seen in Figure 4.21 and Figure 4.22, with raising the cutting edge radius, the machining forces increase for all the feed rates under study. More particularly, similar to the results obtained for the analysis of the cutting speed and rake angle, the percentage increase in the feed force is much larger than that in the cutting force for all the feed rates when the cutting edge radius is increased. This shows that the influence of the cutting edge radius on the feed force is larger than that on the cutting force.

The effects of feed rate and cutting edge radius on the maximum temperature and the average temperature of the tool tip are shown in Figure 4.23 and Figure 4.24, where it can be seen that both temperatures increase with the feed rate. It is known that an increment in the feed rate increases the tool-chip contact area, and as a result, increases the frictional heat, which raises the machining temperature. Furthermore, for all the feed rates under study, the average temperature of the tool tip increases with increasing the cutting edge radius. The maximum temperature also generally increases with the edge radius. However, the percentage increase in the average temperature of the tool tip is much higher than that in the maximum temperature when the cutting edge radius increases.

The chip thickness increases with raising the feed rate as displayed in Figure 4.25. Increasing the feed rate increases the cutting area, and consequently, increases the chip thickness. Also, similar to the results for the cutting speed and rake angle, the variation of the chip thickness with the cutting edge radius is very small.

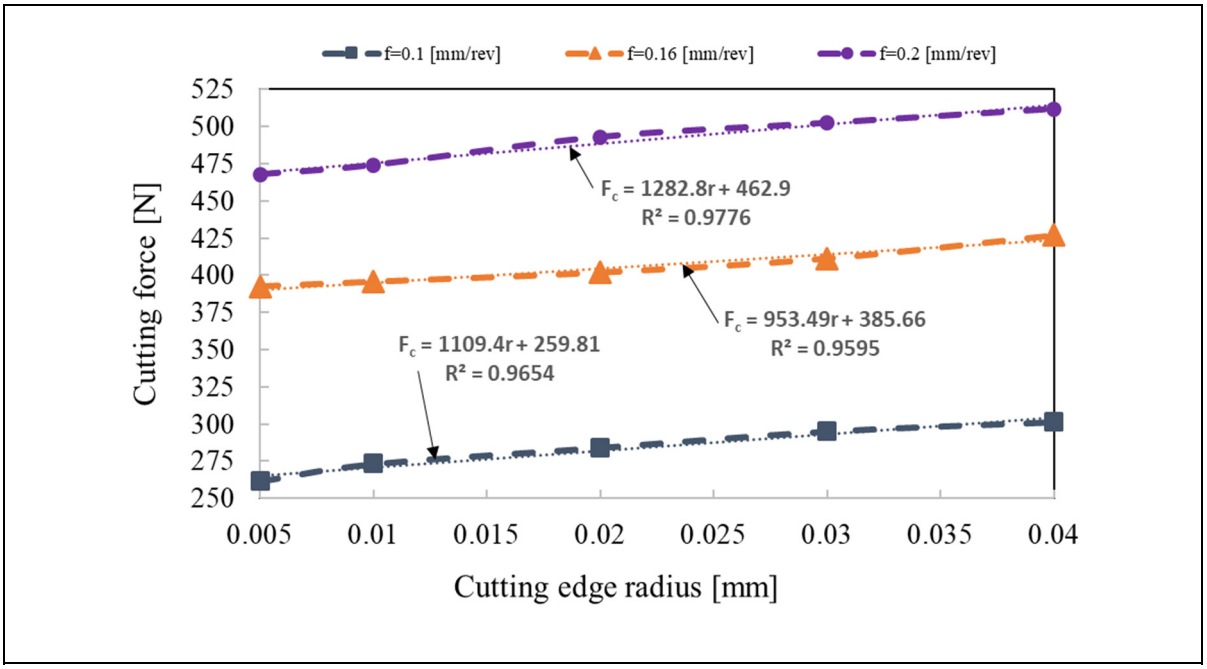

Figure 4.21 The influence of cutting edge radius and feed rate on cutting force

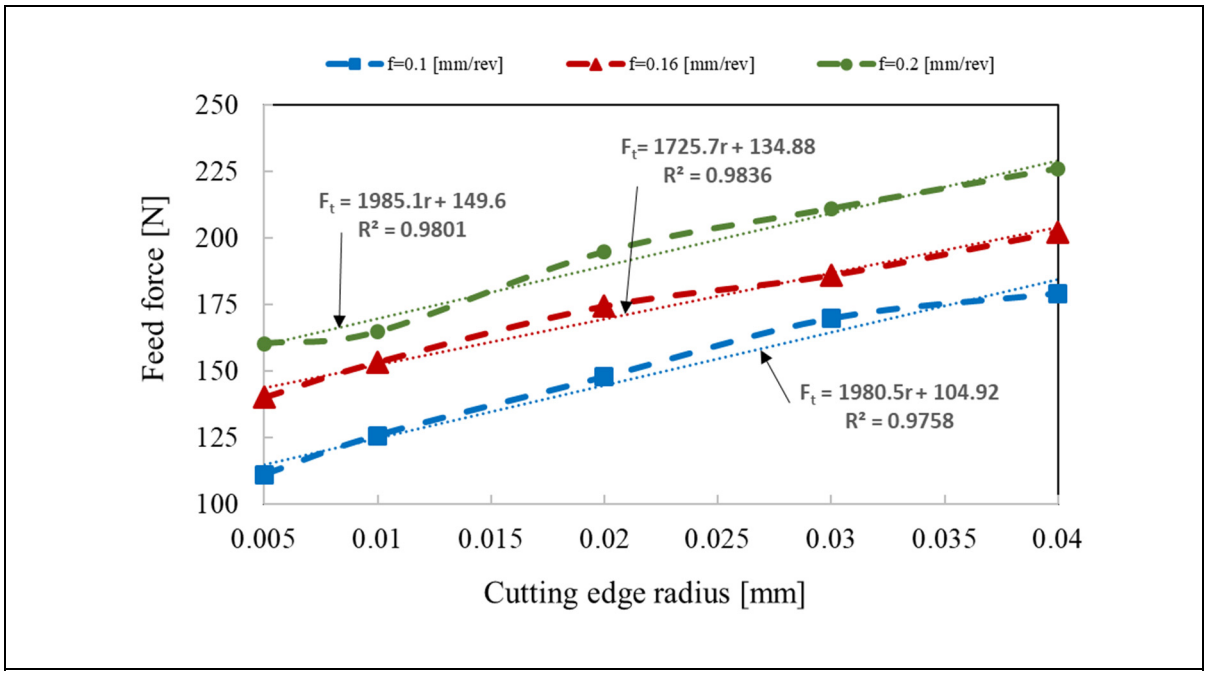

Figure 4.22 The influence of cutting edge radius and feed rate on feed force

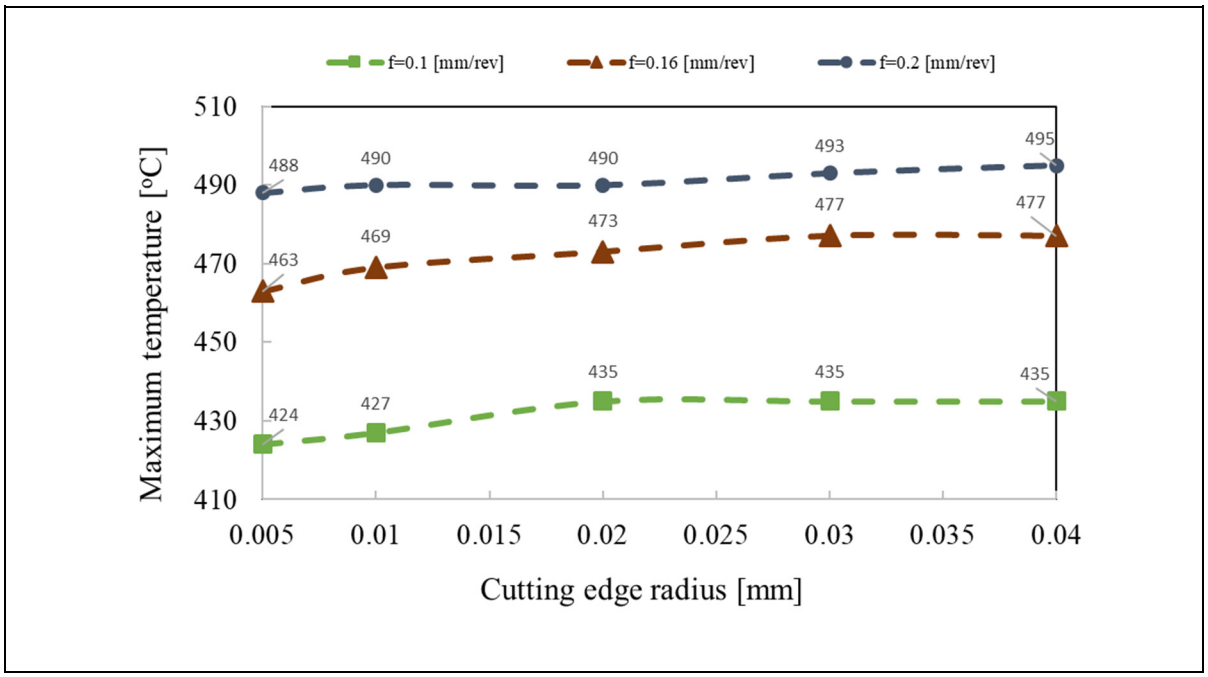

Figure 4.23 The impact of cutting edge radius and feed rate on maximum temperature

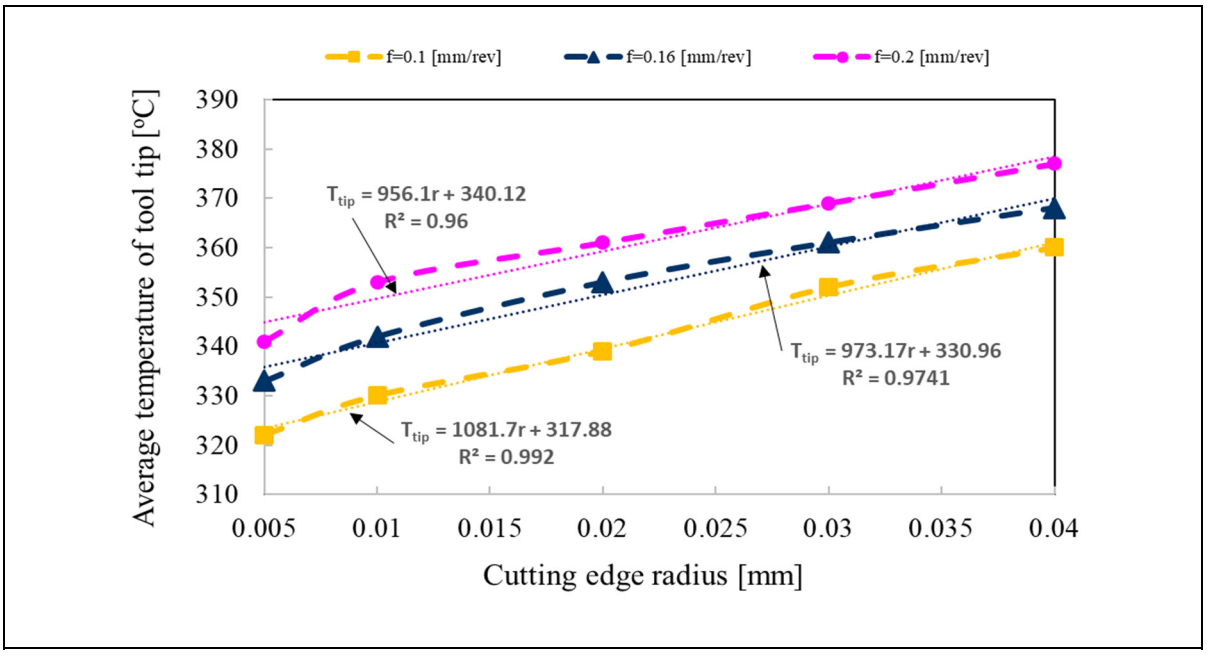

Figure 4.24 The impact of cutting edge radius and feed rate on the average temperature of tool tip

4.7 Summary and conclusions

In this research study, the impact of tool's cutting edge radius on machining forces, cutting temperature, and chip thickness was investigated in orthogonal straight turning of aluminum alloys 6061-T6 for various cutting speeds, rake angles and feed rates using FEM. The FE simulations were performed using the DEFORM^{TM} software. Special attention was given to study the effect of the cutting edge radius on machining characteristics and comparison of the results in CM and HSM. The FE model was validated with the experimental tests for several machining conditions. The results demonstrated that both cutting and feed forces were more sensitive to the cutting edge radius at low cutting speeds (related to CM) and also at a negative rake angle. It was also found that the location of the maximum cutting temperature and the sensitivity of the maximum cutting temperature to the cutting edge radius in cutting of metals depend more on cutting conditions and tool geometry than workpiece and tool materials. Also, the maximum cutting temperatures remained nearly constant with increasing the tool edge radius, whereas the average temperatures of the tool tip clearly increased particularly in HSM. Finally, the results obtained for various cutting speeds, rake angles, and feed rates showed that

the variation of the chip thickness with the cutting edge radius was slight, especially in HSM. These results provide the industry with some insight into the design of tool geometry to improve the machining characteristics including machining forces, cutting temperature and chip morphology. Accurate predictions of machining forces and temperature are crucial for selecting the optimal machining parameters to improve the machining efficiency and the surface integrity of components as the end goal of the machining industry. Moreover, the developed finite element model can be utilized as a predictive reliable tool for industrial applications to avoid conducting too many expensive, time-consuming experimental tests, which will be more desirable and economical to the industrial environments.

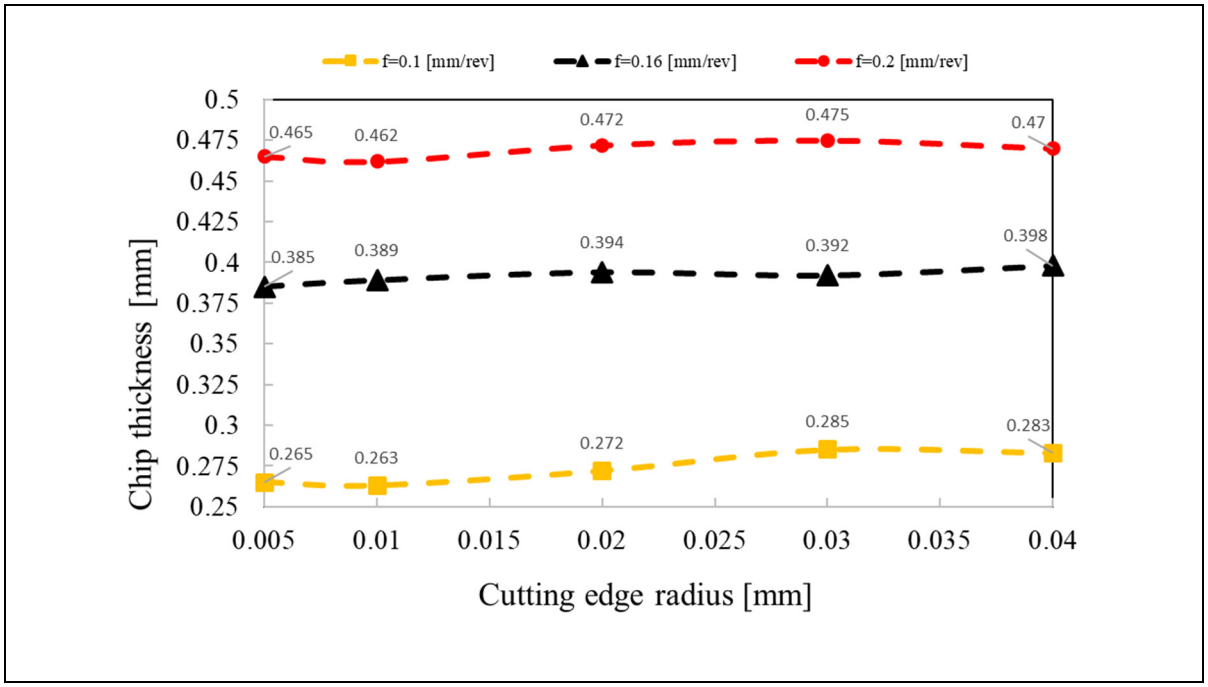

Figure 4.25 The influence of cutting edge radius and feed rate on chip thickness

CHAPTER 5

EFFECT OF TURNING ENVIRONMENTS AND PARAMETERS ON SURFACE INTEGRITY OF AA6061-T6: EXPERIMENTAL ANALYSIS, PREDICTIVE MODELING, AND MULTI-CRITERIA OPTIMIZATION

Mahshad Javidikia[1], Morteza Sadeghifar[1], Victor Songmene[1], Mohammad Jahazi[1]

[1]Department of Mechanical Engineering, École de Technologie Supérieure, 1100 Notre-Dame Ouest, Montréal, Québec, Canada H3C 1K3

This article is published in "International Journal of Advanced Manufacturing Technology", Volume 110, August 2020, Pages 2669-2683
DOI: 10.1007/s00170-020-06027-w

5.1 Abstract

The present research investigates the effect of turning environments and parameters on surface integrity induced by turning of AA6061-T6. Specifically, the evolution of turning parameters of cutting speed, feed rate and depth of cut was studied under DRY, Minimum Quantity Lubrication (MQL) and WET environments and their impact on surface roughness and residual stresses, as critical parameters for surface integrity, were quantified. Machining tests were carried out using a Design of Experiment (DoE) based on Central Composite Design (CCD) under the three turning environments. The most effective turning parameters were identified for each environment using Analysis of Variance (ANOVA). Response Surface Method (RSM) was used to predict effective regression models for each turning environment for the average arithmetic surface roughness, the height peak from the valley, the axial surface residual stress, and the hoop surface residual stress. Then, using the predictive regression models, a multi-objective optimization study was performed to determine optimal turning parameters in each environment for improved surface integrity in Low Speed Turning (LST) and High Speed Turning (HST) of AA6061-T6. The results showed that feed rate and cutting speed were the most effective parameters on surface integrity. It was also found that better surface integrity

and higher material removal rate (MRR) were achieved using MQL mode, which is an environmental friendly and cost saving turning environment.

Keywords: Turning Environment; Aluminum Alloy; Surface Integrity; Regression Model; Multi-Criteria Optimization

5.2 Introduction

Machining processes are commonly used in the aerospace industry to produce the final shape of the parts. Turning operations affect the surface integrity of machined components due to high temperature, large strain, and high strain rate occurring during cutting process (Javidikia *et al.*, 2020). It is important to improve the machining-induced surface integrity of surface and subsurface layers for crack prevention and fatigue life improvement (Javidi *et al.*, 2008; Touazine *et al.*, 2019). In a turning process, it is important to use optimum turning parameters (cutting speed, feed rate, and depth of cut) and turning environment to achieve higher surface quality. The process could be carried out under dry, wet, or MQL modes, which the amount of cutting fluid applied in MQL machining is extremely smaller than that in wet machining. Cutting fluids as coolant and/or lubricant are utilized to reduce the generated heat due to the plastic work in the component and the frictional work at the tool-chip interface (Kouam *et al.*, 2015).

Kirby *et al.* (2006) conducted a study on AA6061-T6 to capture the optimal dry turning parameters including spindle speed, feed rate, depth of cut, and tool nose radius in order to improve surface finish using a Taguchi's L9 orthogonal array experimental design approach. The results showed that feed rate and tool nose radius were the most effective parameters on surface roughness. Jayaraman (2014) conducted turning of AA6063-T6 under dry mode to optimize cutting speed, feed rate, and depth of cut in terms of surface roughness using a Taguchi's L9 orthogonal array and the Grey relational analysis. The results showed that feed rate and depth of cut were the most influential factors on surface roughness.

Horváth et Drégelyi-Kiss (2015) investigated the effect of cutting speed, feed rate, depth of cut, and tool's cutting edge shape on surface roughness of two aluminum alloys. They utilized CCD, RSM, and multi-performance optimization and found that cutting speed and feed rate were the most influential parameters. Camposeco-Negrete (2015) carried out an experimental study on the rough turning of AA6061-T6 in wet mode using CCD and RSM and reported that feed rate was the most significant factor for minimizing surface roughness.

Priyadarshi et Sharma (2016) evaluated the impact of cutting speed, feed rate, and depth of cut on average arithmetic surface roughness in turning of Al-6061-SiC-Gr hybrid nanocomposites under dry mode. CCD, RSM, and multi-objective optimization were used to minimize the response. They found that feed rate and depth of cut had significant effects on surface roughness. Deepak et Rajendra (2016) performed an optimization study to minimize the arithmetic average surface roughness induced by turning of AA6061 in dry mode using RSM and a Taguchi L9 orthogonal array experimental design method. They found that feed rate was the most influential cutting parameter on surface roughness, followed by cutting speed and depth of cut.

Saravanakumar *et al.* (2018) conducted an optimization study of cutting speed, feed rate, and depth of cut in dry turning of AA6063 using RSM and a Taguchi's L27 orthogonal array experimental design method to minimize surface roughness. The results demonstrated that surface roughness was remarkably influenced by feed rate, followed by cutting speed. Sateesh *et al.* (2018) carried out an analysis to find the optimum values of spindle speed, feed rate, and depth of cut to minimize the surface roughness of the workpiece in dry turning of Al6063-T6 using a Taguchi L9 orthogonal array and the Grey relational analysis. The optimum value of the arithmetic average surface roughness was obtained for the maximum spindle speed and depth of cut and the minimum feed rate in the design space.

Warsi *et al.* (2019) obtained the optimal cutting speed, feed rate, and depth of cut during high-speed turning of AA6061-T6 alloy under dry condition to minimize surface roughness. RSM, the Taguchi's L18 orthogonal array design method and the Grey relational analysis augmented

with the analytic hierarchy process were utilized to obtain optimal values. The ANOVA results showed that feed rate was the most important parameter influencing surface roughness while cutting speed and depth of cut were in the second and third places, respectively. The optimization results demonstrated that surface roughness remained unaffected. It needs mentioning that in the above-mentioned research works, residual stresses were not studied and optimized. Moreover, the effect of different turning environments such as dry, MQL, and wet on surface integrity was not examined and compared.

Regarding residual stresses induced by turning of metals, a few studies investigated the influences of cutting conditions. In addition, only a few studies proposing regression models and performing the optimization of surface integrity characteristics in turning of aluminum alloys, especially for different turning environments, were found in the open literature. Ajaja *et al.* (2019) performed a multi-objective optimization to find the optimal cutting tool, cutting speed, feed rate, and depth of cut in order to minimize residual stresses and surface roughness parameters induced by hard turning of 300M Steel in wet cutting condition. They utilized RSM and three different approaches named the single-response Taguchi method, the multi-response Grey relational analysis, and the proportion quality loss reduction method. However, the impact of different turning environments on surface integrity was not investigated and compared.

Leppert et Peng (2012) carried out an experimental study to investigate the effects of dry, MQL, and wet modes together with cutting speed, feed rate, and depth of cut on residual stresses after turning AISI 316L steel using regression functions. The results showed that by properly selecting cutting parameters, the values of residual stresses in dry and MQL modes could be lower or comparable to those in wet turning.

Garcia *et al.* (2019) optimized cutting speed, feed rate, and depth of cut on finish turning of AA6082-T6 for dry and reduced quantity lubricant (RQL) modes to improve surface roughness using Box-Behnken design (BBD) and RSM. The ANOVA results showed that feed rate was the most important input on surface roughness for both dry and RQL conditions. Moreover,

the results presented that using RQL mode led to eliminating the waviness, which occurred in dry machining. However, residual stresses were not studied and analyzed in this study. Moreover, surface roughness was not optimized to determine the optimal cutting conditions.

Boulahmi (2015) studied and optimized feed rate and tool's nose radius to improve surface roughness parameters and residual stresses in turning AA2024-T4, AA6061-T6, and AA7075-T651 under various environments of dry, MQL and wet using DoE and RSM. The results showed that MQL turning provided the best results for all individually investigated responses. It was also observed that surface roughness increased with increasing feed rate and compressive residual stresses were observed for the lowest feed rates. However, the effect of cutting speed and depth of cut on surface roughness and residual stress were not analyzed and the responses were not optimized altogether.

Previous research studies focusing on the design optimization of surface integrity in turning of aluminum alloy were limited mostly to surface roughness parameters and other machinability indexes such as machining forces, cutting temperature, tool wear, energy consumption, and MRR. As far as the literature reveals, no studies on the multi-criteria optimization of the overall surface integrity characteristics including residual stresses and surface roughness parameters in turning of AA6061-T6 are available in the open literature, particularly for all of the three turning environments including DRY, MQL, and WET. In the present research, the most effective turning parameters on the arithmetic average surface roughness, the maximum height of the profile, the axial surface residual stress, and the hoop surface residual stress for DRY, MQL, and WET environments were identified and regression models were then developed. Moreover, the optimal values of turning parameters in each environment were obtained to optimize and improve the surface integrity characteristics in low and high speed turning of AA6061-T6.

5.3 Methodology

The material used in the study was AA6061-T6 widely used in the automotive, aerospace, and marine industries. An experimental plan, based on central composite design consisting of an extensive range of cutting parameters, was developed. Cylindrical components were turned in the three selected environments. The arithmetic average surface roughness (R_a), the maximum height of the profile (R_t), the axial surface residual stress (σ_a), and the hoop surface residual stress (σ_h) were measured for all the samples in each turning environment. The response surface method was used to develop predictive regression models, which were then validated using extra cutting conditions different from those of the DoE. The most effective turning parameters in each environment were identified using analysis of variance. Finally, the models were utilized in the multi-criteria optimization process to determine cutting conditions that provide minimum surface roughness and residual stress characteristics.

5.3.1 Design of Experiment and Response Surface Method

The turning experiments were conducted using a DoE based on the CCD method with three factors and five levels. The independent factors were cutting speed (V), feed rate (f), and depth of cut (D). Nineteen experiments were generated including 8 (2^3) factor points, 6 (2×3) star points, and 5 center points (including 4 replications). It is well proved that the models based on CCD provide acceptable accuracy of nonlinear responses, which is the case for turning operations (Jawahir *et al.*, 2011; Thakur et Gangopadhyay, 2016). The Design-Expert® software was used to conduct analysis of variance.

RSM is a combination of mathematical and statistical techniques used to build response functions fitting to the data (Kosaraju et Anne, 2013). RSM is based on regression analysis to find a suitable approximation, often polynomial functions, to the true relationship between the output quantities and input variables (Sadeghifar *et al.*, 2018b).

A complete quadratic model with 3 design variables and 10 terms ((3+1)(3+2)/2)) was utilized as indicated in Eq. (5.1) (Montgomery, 2006):

$$y = a_0 + a_1 \times V + a_2 \times f + a_3 \times D + a_4 \times V \times f + a_5 \times f \times D + a_6 \times V \times D + a_7 \times V^2 + a_8 \times f^2 + a_9 \times D^2 \quad (5.1)$$

where a_0 to a_9 are the regression coefficients.

The coefficient of determination, R^2, was calculated as (Montgomery, 2006):

$$R^2 = 1 - (SSE/SST) \quad (5.2)$$

in which $SSE = \sum_{i=1}^{n}(y_i - \hat{y}_i)^2$ and $SST = \sum_{i=1}^{n}(y_i - \bar{y})^2$, where y_i is the true output response, here obtained from the experiments, $\hat{y}_i$ is the approximate response computed from RSM, $\bar{y}$ is the average of the true response, n is the number of design points used to generate the model, and i is the number of independent variables in the model.

5.3.2 Multi-criteria optimization

Using the response functions obtained in the previous section, a number of optimization criteria based on the desired performances can be formulated as follows:

$$\begin{gathered} \text{Find } V, f, \text{ and } D \text{ to} \\ \text{Minimize } R_a, R_t, \sigma_a, \text{ and } \sigma_h \\ \text{Subject to } V_L - V \leq 0, V - V_U \leq 0, f_L - f \leq 0, \\ f - f_U \leq 0, D_L - D \leq 0, \text{ and } D - D_U \leq 0 \end{gathered} \quad (5.3)$$

where $V, f,$ and D are the design variables, R_a, R_t, σ_a, and σ_h are the objective functions (OFs), and V_L, f_L, and D_L and V_U, f_U, and D_U are the lower and upper bounds of the design variables, respectively.

The multi-criteria optimization procedure was conducted based on a hill climbing technique using a penalty function approach. The goal of the penalty function is to provide a hill to climb when the optimization starts in an undesirable location. In addition to the design points, a set of random points are checked to see if there is a more desirable solution (Design-Expert User's Manual, 2019). A constrained optimization problem can be transformed to an unconstrained problem by constructing a composite function using the objective and constraint functions (CF) (Arora, 2012) through a penalty approach as:

$$\text{Find } X \text{ to}$$
$$\text{Minimize} \quad \left\{ f(X) + p \sum_{j} g_j(X) \right\} \tag{5.4}$$

where X is a vector of design variables, $f(X)$ is the response to be minimized, $g_j(X)$ are the constraints whose values are positive (for $j = 1$ to m where m is the number of constraints), and p is a penalty parameter (greater than zero) which starts at 1 and increases with each iteration by a factor of 100. The number of iterations is limited to 15, which gives a maximum penalty factor of 10^{30}. Convergence is achieved and the optimum point is found, when the distance between two consecutive objective functions (OFs), or the change in the ratio of the two functions is less than 10^{-6} (Sadeghifar *et al.*, 2020). An overview of the hill climbing optimization solution procedure can be found in (Design-Expert User's Manual, 2019).

5.4 Experimental tests and measurements

Turning tests for the cutting length of 80 mm were conducted on a MAZAK CNC machine for the three environments, as illustrated in Figure 5.1(a) and Figure 5.1(b). The workpiece was a 75-mm diameter and 120-mm length cylinder made of AA6061-T6. The T6 heat treatment is corresponding to a heat solution treatment and an artificial aging. The beneficial properties of T6 temper are obtained through the solution treatment process involving high temperature heating and rapid cooling of material, leading to a stronger and more useful material (Khan *et al.*, 2017). The chemical composition and mechanical, thermal, and physical properties of

AA6061-T6 are given in Table 5.1 and Table 5.2, respectively. The insert was made of uncoated carbide with the designation of ISO CNMG 120408-THM providing a nose radius of 0.8 mm. A KENNAMETAL right-hand tool holder (DCLNR 2020 K12) was utilized to hold the inserts. A new insert and component were used for each machining experiment to provide similar conditions for all the tests. MQL experiments were carried out using a Tecnolub system model SLS1.2-2. The cutting fluids for MQL and WET modes were Microkut 400 and Oemeta coolant with flow rate of 21.5 ml/min and 7200 ml/min, respectively. The machining tests were carried out using a DoE planed with CCD with three factors and five levels consisting of nineteen cutting conditions as given in Table 5.3 and Table 5.4. The center point was replicated four times (Test Nos. 2, 4, 5, 7, and 9) to obtain a more precise evaluation of the lack of fit of the regression models and the measurement errors. Mitutoyo SJ-410 was used to measure surface roughness parameters as shown in Figure 5.2.

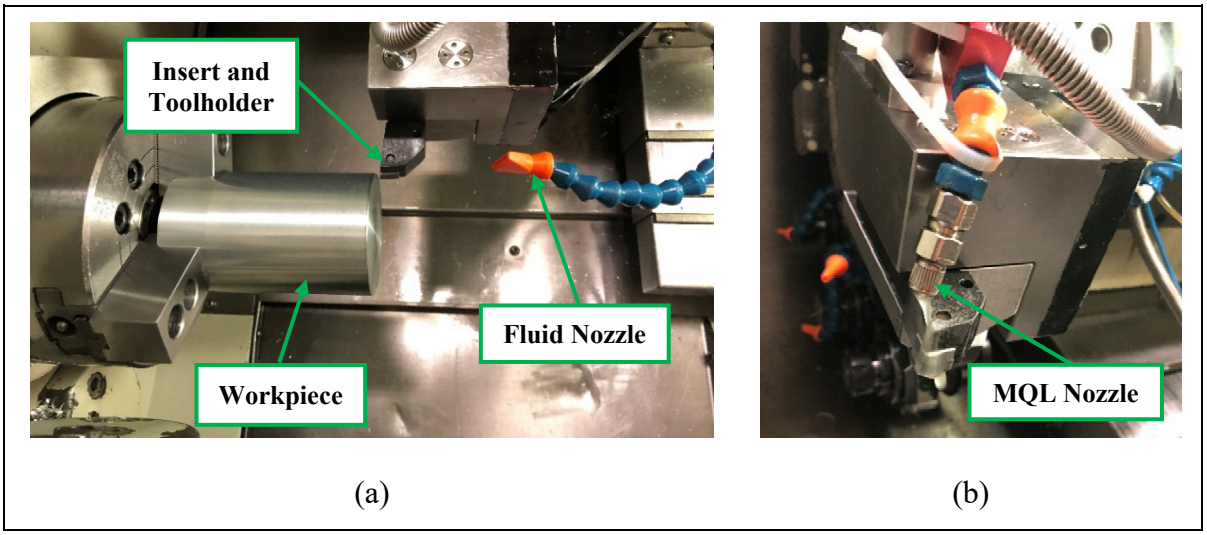

Figure 5.1 The experimental set-up of the turning process: (a) DRY and WET modes, (b) MQL mode

Table 5.1 Chemical composition (wt.%) of AA6061-T6 (Jomaa *et l.*, 2016)

Si	Fe	Cu	Mn	Mg	Cr	Zn	Ti	Al
0.6	0.2	0.28	0.1	1.0	0.2	0.22	0.12	Balance

Table 5.2 Mechanical, thermal, and physical properties of AA6061-T6 (Javidikia *et al.*, 2020b)

Properties	AA6061-T6
Density $\rho\ (kg/m^3)$	2700
Young's modulus $E\ (GPa)$	58.5
Poisson's ratio υ	0.33
Conductivity $k\ (W/m\ ^oC)$	167
Specific heat capacity $c\ (J/kg\ ^oC)$	896
Thermal expansion coefficient $\alpha\ (1/\ ^oC)$	23.5×10^{-6}
Tensile yield strength (MPa)	276
Melting temperature $(\ ^oC)$	652

Table 5.3 Factors and levels in the DoE

Level	Factor		
	Cutting speed $V\ (m/min)$	Feed rate f (mm/rev)	Depth of cut $D\ (mm)$
1	145	0.07	0.66
2	350	0.12	1
3	650	0.19	1.5
4	950	0.26	2
5	1155	0.31	2.34

Table 5.4 DoE using CCD

Run	V (m/min)	f (mm/rev)	D (mm)	Run	V (m/min)	f (mm/rev)	D (mm)
1	350	0.26	1	11	950	0.12	2
2	650	0.19	1.5	12	145	0.19	1.5
3	350	0.12	1	13	650	0.31	1.5
4	650	0.19	1.5	14	950	0.26	2
5	650	0.19	1.5	15	650	0.19	2.34
6	350	0.12	2	16	350	0.26	2
7	650	0.19	1.5	17	650	0.19	0.66
8	650	0.07	1.5	18	1155	0.19	1.5
9	650	0.19	1.5	19	950	0.12	1
10	950	0.26	1				

The sampling length and the evaluation length were set to 0.8 and 4 mm, respectively, using a Gaussian filter. As shown in Figure 5.3(a) and Figure 5.3(b), residual stresses in hoop and axial directions were measured using a Pulstec μ-X360n X-Ray Diffraction machine, which uses Debye-Scherrer ring image (based on a diffracted cone) and cos α method to measure and calculate residual stresses (Sadeghifar *et al.*, 2018b). In addition, X-Ray incidence angle and X-Ray irradiation time were selected as 25 degrees and 30 s, respectively. Bragg's angle and crystallographic plane were 139.3 degrees and {311}, respectively. Surface roughness parameters and residual stresses were measured on all the machined samples at two points located 3 cm from the front edge of the sample.

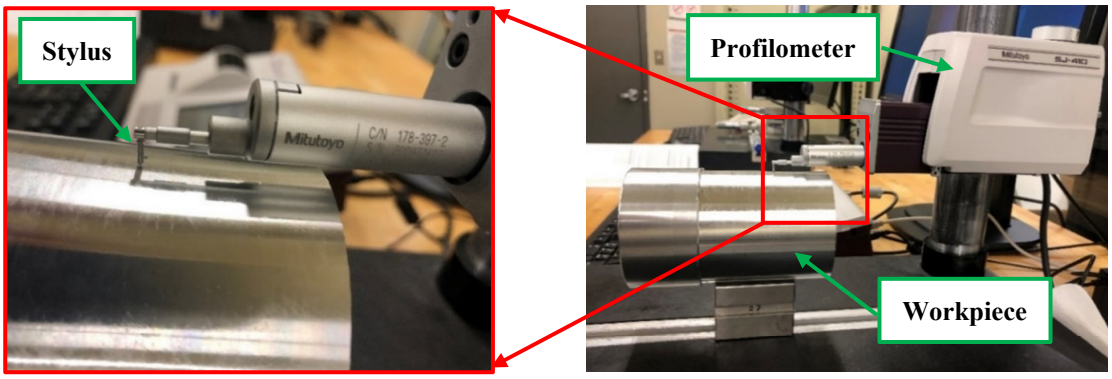

Figure 5.2 Mitutoyo SJ-410 profilometer for surface roughness measurements

Figure 5.3 Pulstec μ-X360n XRD machine for measuring: (a) Hoop and (b) Axial residual stresses

5.5 Results and discussion

5.5.1 A Comparative analysis of surface integrity characteristics

Table 5.5, Table 5.6, and Table 5.7 provide the measured values of surface roughness and residual stress characteristics for DRY, MQL, and WET environmental modes, respectively. As reported in these tables, for all the three lubrication modes, the lowest and highest R_a occurred at Test Nos. 8 and 13, respectively. Specifically, the minimum and maximum values of the average arithmetic surface roughness R_a were from 0.345 μm for Test No. 8 to 2.519 μm for Test No. 13 for DRY mode, from 0.304 μm for Test No. 8 to 2.649 μm for Test No. 13 for MQL mode, and from 0.472 μm for Test No. 8 to 2.806 μm for Test No. 13 for WET mode. The above two tests correspond to the smallest and largest values of feed rate (for the same cutting speed and depth of cut) equal to 0.07 mm/rev and 0.31 mm/rev, respectively. It is also seen that the R_a values for DRY and MQL modes were slightly lower than those obtained for WET mode. This might be attributed to the fact that in WET machining, cutting temperature is lower than that in DRY and MQL modes, leading to less thermal softening, and as a result, higher cutting forces and tool wear, and consequently, less surface quality (Sadeghifar *et al.*, 2018b; Pawade *et al.*, 2008).

The lowest and highest values of the height peak from the valley R_t were ranged from 2.112 μm for Test No. 8 to 9.866 μm for Test No. 13 for DRY mode, from 1.952 μm for Test No. 8 to 10.152 μm for Test No. 13 for MQL mode, and from 2.526 μm for Test No. 8 to 10.704 μm for Test No. 13 for WET mode. As seen, for all the three environments, the trend of variation of R_t was the same as the one obtained for R_a.

Table 5.5 Experimental measurements of surface integrity in DRY mode

Run	R_a (μm)	R_t (μm)	σ_a (MPa)	σ_h (MPa)	Run	R_a (μm)	R_t (μm)	σ_a (MPa)	σ_h (MPa)
1	2.494	9.632	99	98	11	0.861	3.682	69	122
2	1.482	7.382	106	152	12	1.499	7.238	85	70
3	0.607	3.509	90	90	13	2.519	9.866	163	148
4	1.233	5.002	115	162	14	2.086	8.509	120	178
5	1.245	5.270	115	120	15	1.640	6.740	72	119
6	0.992	6.656	50	98	16	2.309	9.169	126	131
7	1.122	4.742	123	136	17	1.267	4.889	118	117
8	0.345	2.112	50	106	18	1.349	5.785	111	156
9	1.225	5.479	132	128	19	0.538	2.840	96	144
10	1.967	7.426	114	178					

Table 5.6 Experimental measurements of surface integrity in MQL mode

Run	R_a (μm)	R_t (μm)	σ_a (MPa)	σ_h (MPa)	Run	R_a (μm)	R_t (μm)	σ_a (MPa)	σ_h (MPa)
1	2.320	9.698	87	45	11	0.815	3.794	85	94
2	0.826	4.096	113	131	12	1.450	6.786	68	60
3	0.758	3.979	73	94	13	2.649	10.152	123	150
4	1.156	5.236	140	138	14	2.451	9.578	129	136
5	0.815	4.338	132	157	15	1.294	5.725	89	60
6	0.556	3.125	63	74	16	2.042	9.007	100	124
7	1.562	6.547	135	130	17	1.314	5.619	118	70
8	0.304	1.952	38	90	18	1.282	5.945	143	131
9	1.285	5.870	100	135	19	0.532	2.065	80	119
10	2.146	9.152	136	114					

Table 5.7 Experimental measurements of surface integrity in WET mode

Run	R_a (μm)	R_t (μm)	σ_a (MPa)	σ_h (MPa)	Run	R_a (μm)	R_t (μm)	σ_a (MPa)	σ_h (MPa)
1	1.945	7.973	100	54	11	0.706	3.398	68	150
2	0.962	4.457	106	114	12	1.631	6.264	51	36
3	0.657	3.366	-15	-28	13	2.806	10.704	143	74
4	1.364	5.774	119	80	14	1.711	7.180	118	100
5	1.074	4.577	132	107	15	1.353	5.474	74	88
6	0.584	3.173	-112	-28	16	2.211	8.674	108	80
7	1.204	5.178	102	90	17	1.458	5.749	128	130
8	0.472	2.526	55	114	18	1.400	5.754	98	180
9	1.442	5.546	131	120	19	0.479	2.994	220	153
10	2.073	8.306	87	125					

Surface residual stress in the axial direction σ_a extended from 50 MPa for Test Nos. 6 and 8 to 163 MPa for Test No. 13 for DRY mode, from 38 and 63 MPa for Test Nos. 8 and 6 to 140 and 143 MPa for Test Nos. 4 and 18 for MQL mode, and from -112 MPa for Test No. 6 to 220 MPa for Test No. 19 for WET mode. This high value of σ_a (220 MPa) is comparable to the yield strength of AA6061-T6 (about 276 MPa). The above results show that the highest compressive and tensile values of axial surface residual stresses were obtained for WET mode. Moreover, for all the three turning environments, Test No. 6 generally gave the lowest surface axial residual stress.

Hoop surface residual stresses σ_h ranged from 70 MPa for Test No. 12 to 178 MPa for Test Nos. 10 and 14 for DRY mode, from 45 MPa for Test No. 1 to 150 and 157 MPa for Test Nos. 13 and 5 for MQL mode, and from -28 MPa for Test Nos. 6 and 8 to 180 MPa for Test No. 18 for WET mode. The results further confirm that, similar to σ_a, the highest compressive and tensile values of σ_h were obtained for WET mode.

5.5.2 ANOVA and regression analysis

The experimental results of surface roughness and residual stress characteristics were used to derive the predictive mathematical quadratic models using RSM. The predicted regression models were used to quantify the effect of turning parameters, for each environment, on the surface integrity using ANOVA. The regression coefficients of each predictive model are presented in Table 5.8, Table 5.9, and Table 5.10 for DRY, MQL, and WET modes, respectively. The tables also provide the ANOVA results so as to determine the significance (*P-value*) of turning parameters and their interactions and also the accuracy of the regression models (*P-value*, R^2, and *Adequate Precision*). Based on the variance analyses at 95% confidence, the regression terms with *P* values less than 0.05 were considered to be Significant in the predictive models. The lack of fit was calculated and observed to be Non-Significant for all the models. Non-significant terms identified through ANOVA were eliminated from the models. The more R^2 is close to 1, the more accurate the regression models are. *Adequate Precision* measures the signal to noise ratio, where a ratio greater than 4 is desirable.

As observed in the ANOVA results in Table 5.8, Table 5.9, and Table 5.10, *P-value* of the predictive regression models for all three turning environments are less than 5%, showing that all the models are Significant. Moreover, Non-Significant Lack of Fit (greater than 5%) for all the regression models reveals that the models are adequately fit to the experimental data (Priyadarshi et Sharma, 2016; Ajaja *et al.*, 2019; Design-Expert User's Manual, 2019; Touazine *et al.*, 2017; Jumare *et al.*, 2019). Considering that R^2 values are between 85 to 98%, the developed models could be considered statistically precise (Leppert et Peng, 2012; Boulahmi, 2015; Sadeghifar *et al.*, 2018b; Touazine *et al.*, 2017; Capello, 2005) and can be used with a high level of confidence to predict surface integrity characteristics in the design space given in the DoE. It needs mentioning that despite considering wide ranges of cutting speed, feed rate, and depth of cut in the DoE to cover from LST to HST with low to large MRR, the R^2 values are between 92% to 98% for surface roughness and between 85% to 90% for residual stresses, confirming the reliability of the predictive models.

The ANOVA results presented in Table 5.8, Table 5.9, and Table 5.10 show that feed rate is the most significant parameter influencing surface roughness for all the environments, which is confirmed by the results of previous studies (Boulahmi, 2015; Leppert, 2011). Furthermore, the roughness parameters were slightly affected by the turning environments. Feed rate is also the most important parameter affecting σ_a for all environmental modes. This result is in agreement with the one in turning of various aluminums and steels reported by (Leppert et Peng, 2012; Boulahmi, 2015; Capello, 2005; Capello, 2006). This is mainly because of the fact that σ_a is in the same direction as feed rate. Both cutting speed and feed rate are highly influential in MQL and WET modes. The same result was reported by Ajaja *et al.* (2019). In contrast, in terms of σ_h, cutting speed is the most effective parameter for all modes. This is probably due to the fact that the direction of σ_h is the same as that of cutting speed. This result is similar to that obtained in turning of 300M steel by Ajaja *et al.* (2019) and of AISI 316L steel by Leppert et Peng (2012). Accordingly, feed rate and cutting speed were the most influential parameters on the surface integrity characteristics.

Table 5.8 ANOVA for prediction of regression models of surface integrity in DRY mode

Predictor	R_a (μm)		R_t (μm)		σ_a (MPa)		σ_h (MPa)	
	Coef.	P-value	Coef.	P-value	Coef.	P-value	Coef.	P-value
Intercept	-0.43		0.38		11.5826		-5.0459	
V	-0.0006	0.022	-0.0078	0.0120	0.1320	0.1107	0.2041	**< 0.0001**
f	10.9765	**< 0.0001**	34.4108	**< 0.0001**	198.198	**< 0.0001**	-230.449	0.0020
D	-0.1925	0.0169	1.6569	0.0251	22.5004	0.0303	63.6022	0.6565
V^2	7.20E-07	0.0739	4.36E-06	0.0992	-0.00008	0.0361	-0.00007	0.0910
$V \times f$	-0.00327	0.1364					0.2916	0.2188
$V \times D$							-0.0525	0.1225
f^2	13.8162	0.0639	42.5225	0.3603	-984.282	0.1696		
$f \times D$	-2.7642	0.0459	-12.0321	0.1677	357.1428	0.0140	167.8571	0.2367
D^2	0.3012	0.0430	0.5866	0.5155	-35.5554	0.0203	-19.3650	0.2008
Model		**< 0.0001**		**< 0.0001**		**0.0002**		**0.0007**
Fit Statistics								
Lack of fit		0.6968		0.3598		0.2897		0.9013
R^2		98.01 %		92.23 %		89 %		88.84 %
Adeq Precision		28.35		14.63		12.94		10.69

Table 5.9 ANOVA for prediction of regression models of surface integrity in MQL mode

Predictor	R_a (μm)		R_t (μm)		σ_a (MPa)		σ_h (MPa)	
	Coef.	P-value	Coef.	P-value	Coef.	P-value	Coef.	P-value
Intercept	2.048		7.372		-137.284		-148.903	
V	-0.0027	0.9852	-0.0118	0.3675	0.0981	**0.0006**	0.3270	**0.0013**
f	0.2711	**< 0.0001**	13.4928	**< 0.0001**	1322.2944	**< 0.0001**	-290.142	0.0310
D	-1.4515	0.9242	-4.3819	0.7838	81.7866	0.3541	227.2419	0.4954
V^2	1.062E-06	0.1158	5.032E-06	0.0496	-0.00007	0.0913	-0.00014	0.0089
$V \times f$					0.2916	0.2213		
$V \times D$	0.00089	0.0951	0.003	0.1126			-0.0516	0.1743
f^2	27.4796	0.0349	69.8204	0.1238	-3169.446	0.0013	-912.359	0.2962
$f \times D$							521.4285	0.0063
D^2	0.2946	0.2150	0.831	0.3333	-29.5942	0.0654	-95.6639	0.0002
Model		**< 0.0001**		**< 0.0001**		**0.0003**		**0.0007**
Fit Statistics								
Lack of fit		0.9955		0.9293		0.8540		0.2042
R^2		94.56 %		94.72 %		88.17 %		89 %
Adeq Precision		18.79		19.14		11.38		8.01

Table 5.10 ANOVA for prediction of regression models of surface integrity in WET mode

Predictor	R_a (μm)		R_t (μm)		σ_a (MPa)		σ_h (MPa)	
	Coef.	P-value	Coef.	P-value	Coef.	P-value	Coef.	P-value
Intercept	0.4860		2.1392		-244.015		-260.8353	
V	-0.00097	0.2792	-0.0018	0.2753	0.8706	**0.0008**	0.44720	**< 0.0001**
f	2.3094	**< 0.0001**	2.2603	**< 0.0001**	1313.78	**0.0031**	1697.2534	0.6323
D	-0.0173	0.8722	0.5671	0.7273	-120.936	0.0155	-10.6371	0.4404
V^2	5.986E-07	0.3224	2.23E-06	0.1686	-0.0002	0.0291		
$V \times f$					-2.4881	0.0004	-1.5952	0.0021
$V \times D$			-0.00102	0.4129				
f^2	19.9065	0.0853	84.7707	0.0105	-2160.393	0.1919	-1614.633	0.2492
$f \times D$					1028.571	0.0045		
D^2					-39.5152	0.2208		
Model		**< 0.0001**		**< 0.0001**		**0.0003**		**< 0.0001**
Fit Statistics								
Lack of fit		0.5629		0.7076		0.0504		0.1759
R^2		93.12 %		96.33 %		90.52 %		85.15 %
Adeq Precision		21.14		26.08		15.2		13.39

5.5.3 Validation tests

Extra turning parameters named Test Nos. 20 and 21 were chosen in the space of the design of experiment and listed in Table 5.11. These tests were planned to validate the predictive regression models for each turning environment. The surface integrity characteristics were predicted using the regression models given in Table 5.8, Table 5.9, and Table 5.10. For instance, the regression equation of R_a in DRY mode given in Eq. (5.5) was calculated for turning Test No. 20. Moreover, the measured roughness profile of Test No. 20 is shown in Figure 5.4. The surface roughness and surface residual stresses were measured for the new cutting conditions. The predicted and measured values of surface integrity characteristics are compared in Figure 5.5 and Figure 5.6, where the errors are between 0.7% and 19% for surface roughness parameters and residual stresses. Therefore, there is good agreement between predictions and measurements for all the modes and the regression models can be used to better understand the influence of turning parameters and environments on surface integrity.

Table 5.11 Validation tests

Test No.	$V\ (m/min)$	f (mm/rev)	$D\ (mm)$
20	500	0.19	1.75
21	650	0.22	1.25

$$\begin{aligned} &R_a(V = 500, f = 0.19, D = 1.75) \\ &= -0.430094 - 0.000608454 \times V + 10.9765 \times f \\ &-0.192514 \times D - 0.00327381 \times V \times f - 2.76429 \times f \times D + 7.20793e \\ &- 07 \times V^2 + 13.8163 \times f^2 + 0.301205 \times D^2 \end{aligned} \tag{5.5}$$

where R_a is obtained equal to $1.385\ \mu m$.

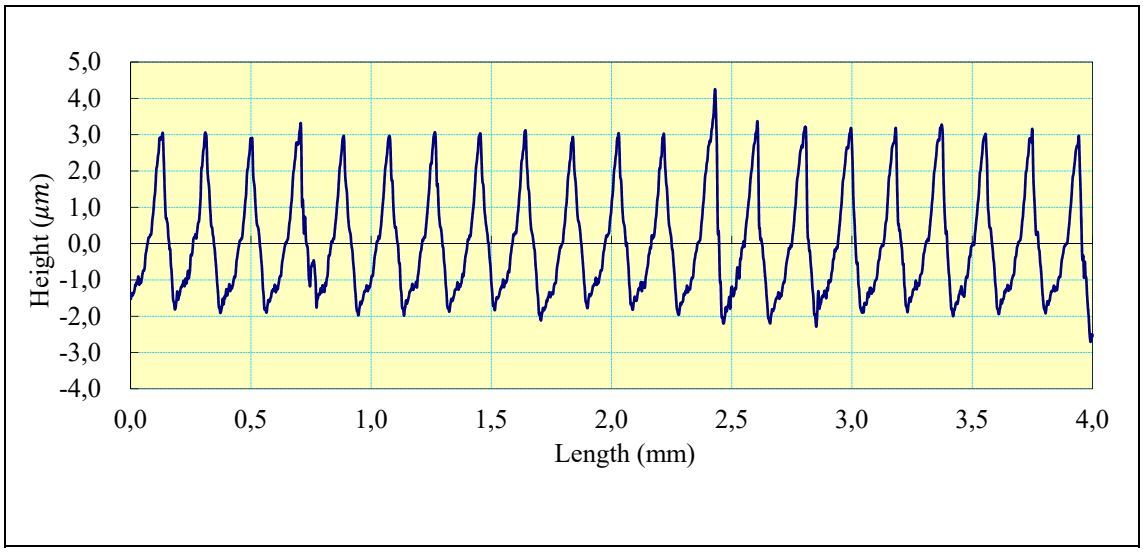

Figure 5.4 The measured roughness profile in DRY mode for Test No. 20

5.5.4 Multi-Criteria optimization of surface integrity

As shown in Table 5.12 for DRY mode, the optimum cutting speed, feed rate, and depth of cut were obtained as 145 m/min, 0.07 mm/rev, and 0.66 mm, respectively, corresponding to the lowest values in the DoE. In addition, the values of R_a, R_t, σ_a, and σ_h were optimized as 0.176 μm, 2.742 μm, 54 MPa, and 46 MPa, respectively. Compared with the best (smallest) values of surface integrity characteristics in the 19 design points in DRY mode, R_a was decreased by 49%, whereas R_t was increased by 29%. Moreover, σ_a was almost the same as the lowest value in the DoE, while σ_h was decreased by 34%. Therefore, surface integrity was generally improved. As displayed in Table 5.12 for MQL mode, the optimum cutting speed, feed rate, and depth of cut were captured as 350 m/min, 0.07 mm/rev, and 2.02 mm, respectively. Furthermore, the optimal values of R_a, R_t, σ_a, and σ_h were obtained as 0.28 μm, 1.863 μm, 16 MPa, and 28 MPa, respectively. In comparison with the lowest value of surface integrity In the 19 design points in MQL mode, R_a, R_t, σ_a, and σ_h were diminished by 8%, 4%, 56%, and 36%, respectively. Consequently, the surface integrity was improved.

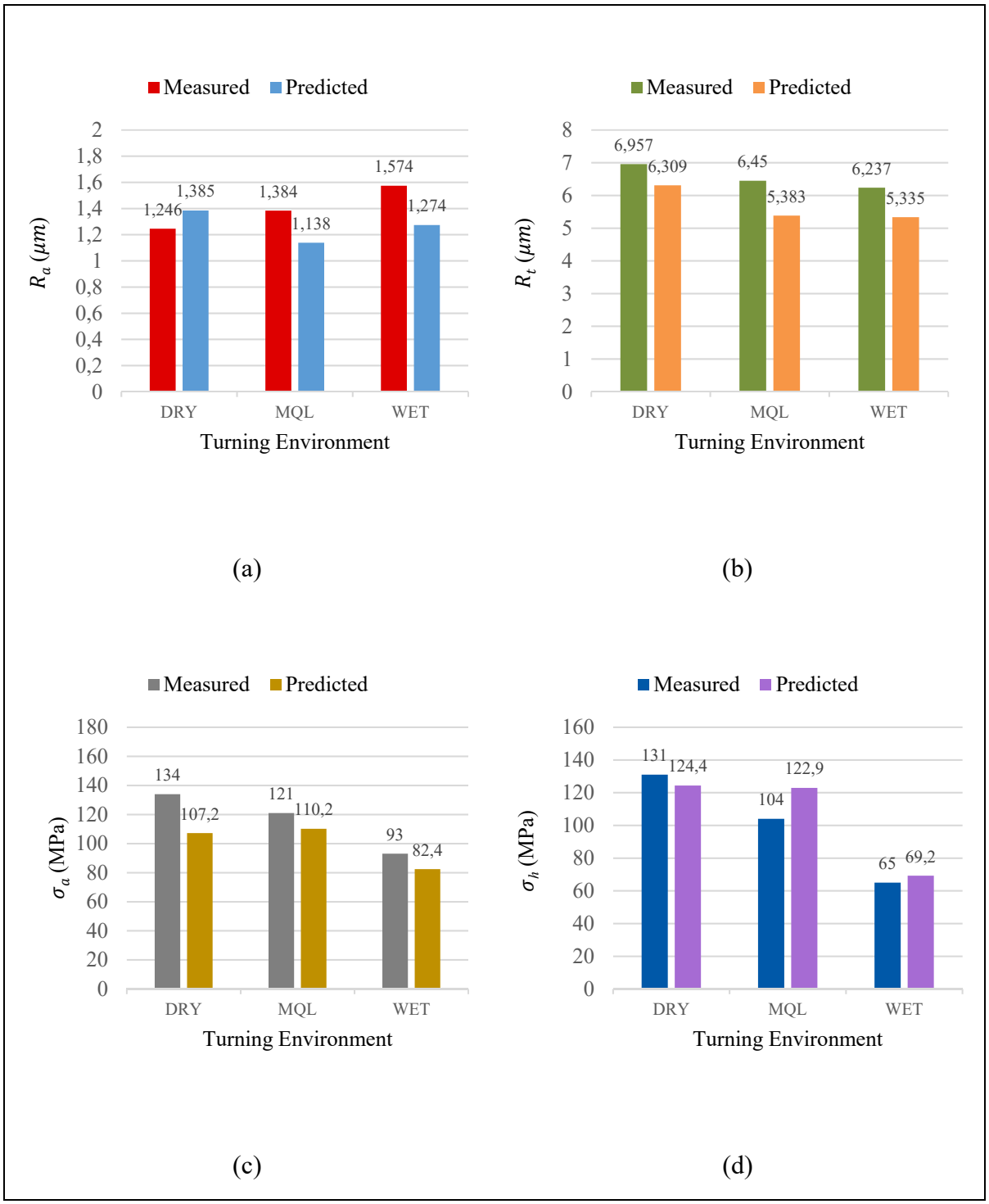

Figure 5.5 Validation of predictive models of (a) R_a, (b) R_t, (c) σ_a, and (d) σ_h for three turning environments for Test No. 20

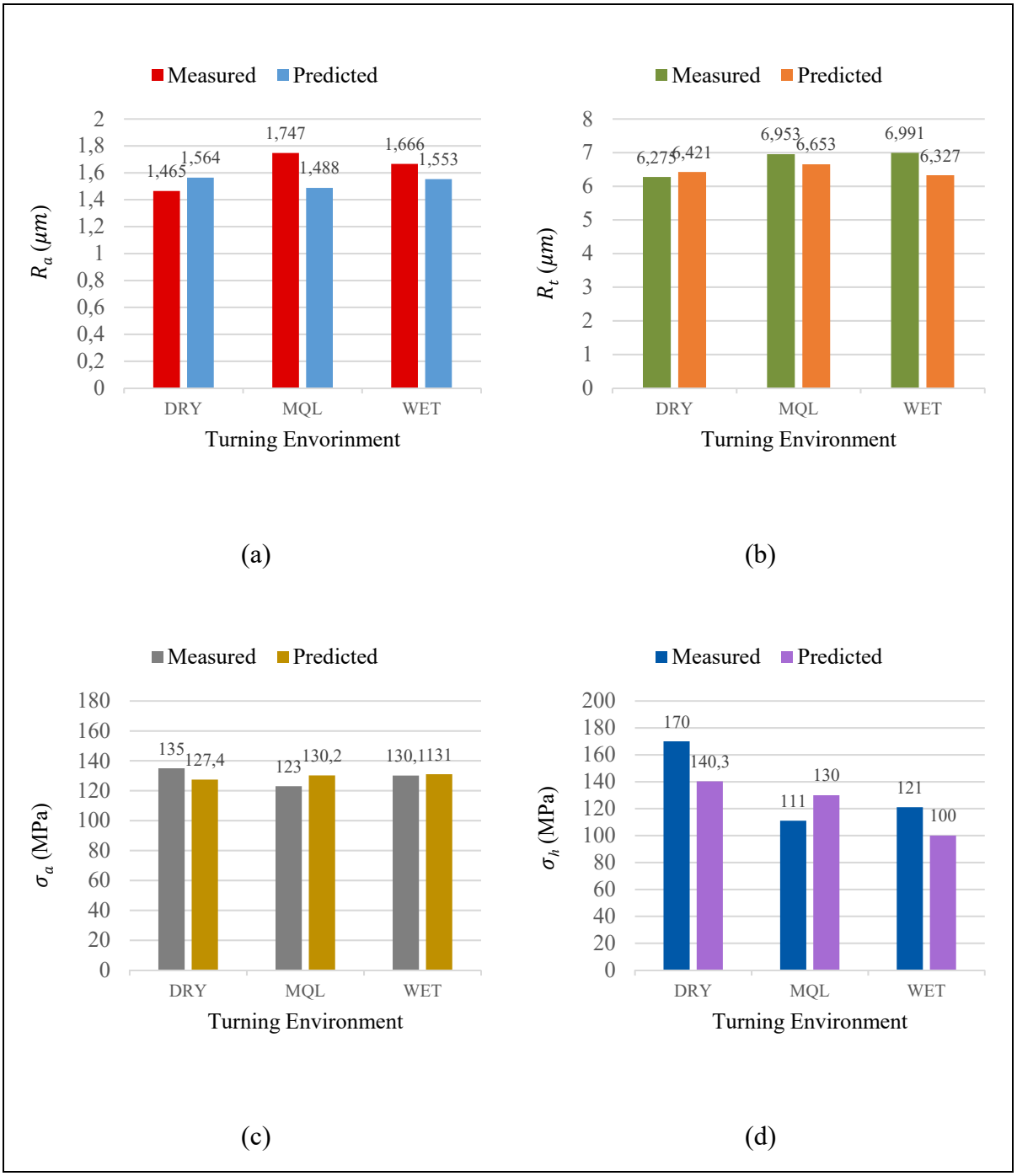

Figure 5.6 Validation of predictive models of (a) R_a, (b) R_t, (c) σ_a, and (d) σ_h for three turning environments for Test No. 21

The optimal cutting speed, feed rate, and depth of cut for WET mode were obtained as 387 m/min, 0.07 mm/rev, and 1.64 mm, respectively, as illustrated in Table 5.12. In addition, the values of R_a, R_t, σ_a, and σ_h were optimized as 0.428 μm, 2.594 μm, -112 MPa, and -28 MPa, respectively. R_a was decreased by 9%, whereas R_t, σ_a, and σ_h remained almost constant compared to the corresponding minimum values in the DoE in WET mode.

Table 5.12 The optimum solutions for surface integrity induced by DRY, MQL, and WET turning

	Turning parameters			Surface integrity			
	V (m/min)	f (mm/rev)	D (mm)	R_a (μm)	R_t (μm)	σ_a (MPa)	σ_h (MPa)
DRY	145	0.07	0.66	0.176	2.742	54	46
MQL	350	0.07	2.02	0.28	1.863	16	28
WET	387	0.07	1.64	0.428	2.594	-112	-28

In order to better understand the interactions between turning parameters, the variations of surface roughness parameters and residual stress characteristics with cutting speed and feed rate are shown in Figure 5.7, Figure 5.8, and Figure 5.9 at the optimal values of depth of cut in DRY, MQL, and WET environments, respectively. As observed in the ANOVA results presented in Table 5.8, Table 5.9, and Table 5.10, since depth of cut had less influence on the surface integrity characteristics, it was fixed in the contour plots. As seen in Figure 5.7(a) and Figure 5.7(b), R_a and R_t increased with increasing feed rate, while they remained almost unaffected with the variation of cutting speed in DRY mode. This is because higher feed rates produce more distinct feed marks at the machined surface and larger machining forces on the tool, resulting in larger magnitudes of surface roughness parameters. Moreover, σ_a reached its highest value around the center point in the design space, as illustrated in Figure 5.7(c). As shown in Fig. Figure 5.7(d), σ_h increased with raising cutting speed. The effect of cutting speed on σ_h was greater at higher values of feed rate in DRY mode, which could be attributed to the high cutting temperature and heat concentration in the cutting zone.

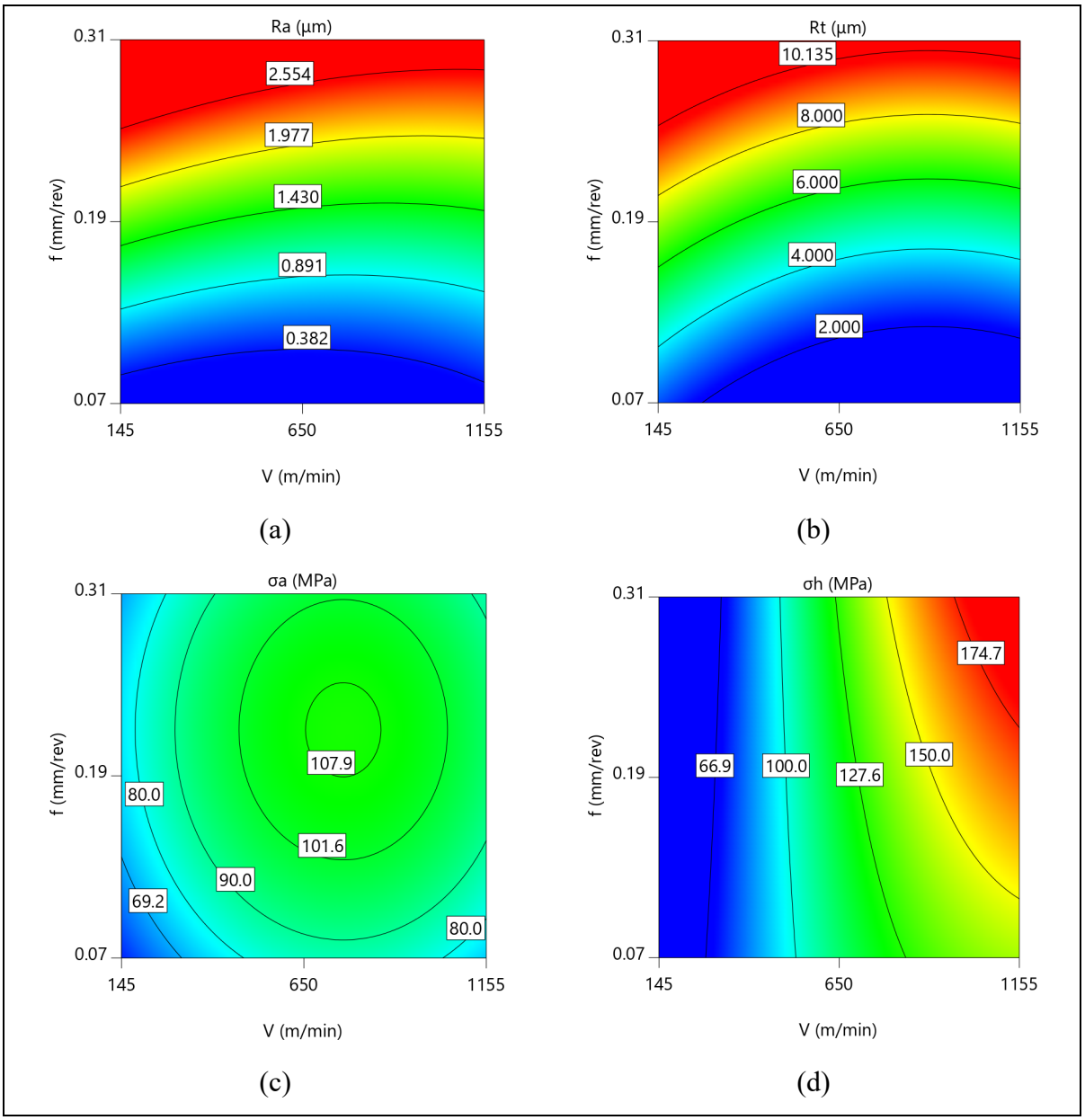

Figure 5.7 Contour plots of surface integrity in DRY mode for D=0.66 mm

As observed in Figure 5.8(a) and Figure 5.8(b), R_a and R_t in MQL mode indicate the same behavior as those obtained in DRY environment. Moreover, as seen in Figure 5.8(c) and Figure 5.8(d), the impact of cutting speed and feed rate on σ_a and σ_h are greater at higher values of the speed and feed in MQL mode, respectively.

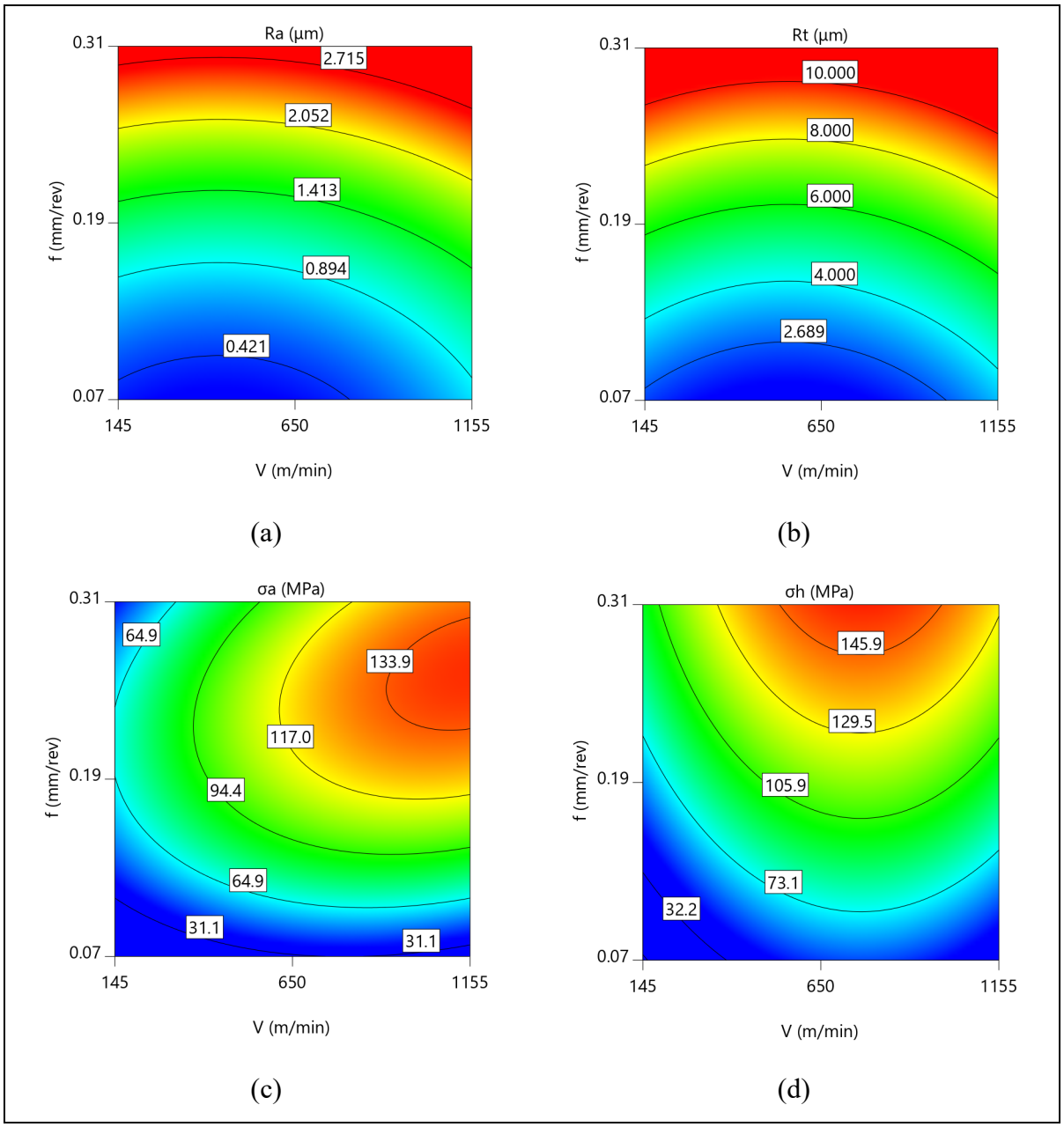

Figure 5.8 Contour plots of surface integrity in MQL mode for D=2.02 mm

R_a and R_t in WET mode show the same behavior as those obtained in DRY and MQL modes (Figure 5.9(a) and Figure 5.9(b)). Furthermore, as observed in Figure 5.9(c), cutting speed plays a more important role on σ_a at lower values of feed rate. In addition, the impact of feed rate on σ_a is greater at lower values of cutting speed in WET mode. As seen in Figure 5.9(d), the influence of cutting speed on σ_h was greater at lower values of feed rate in WET mode.

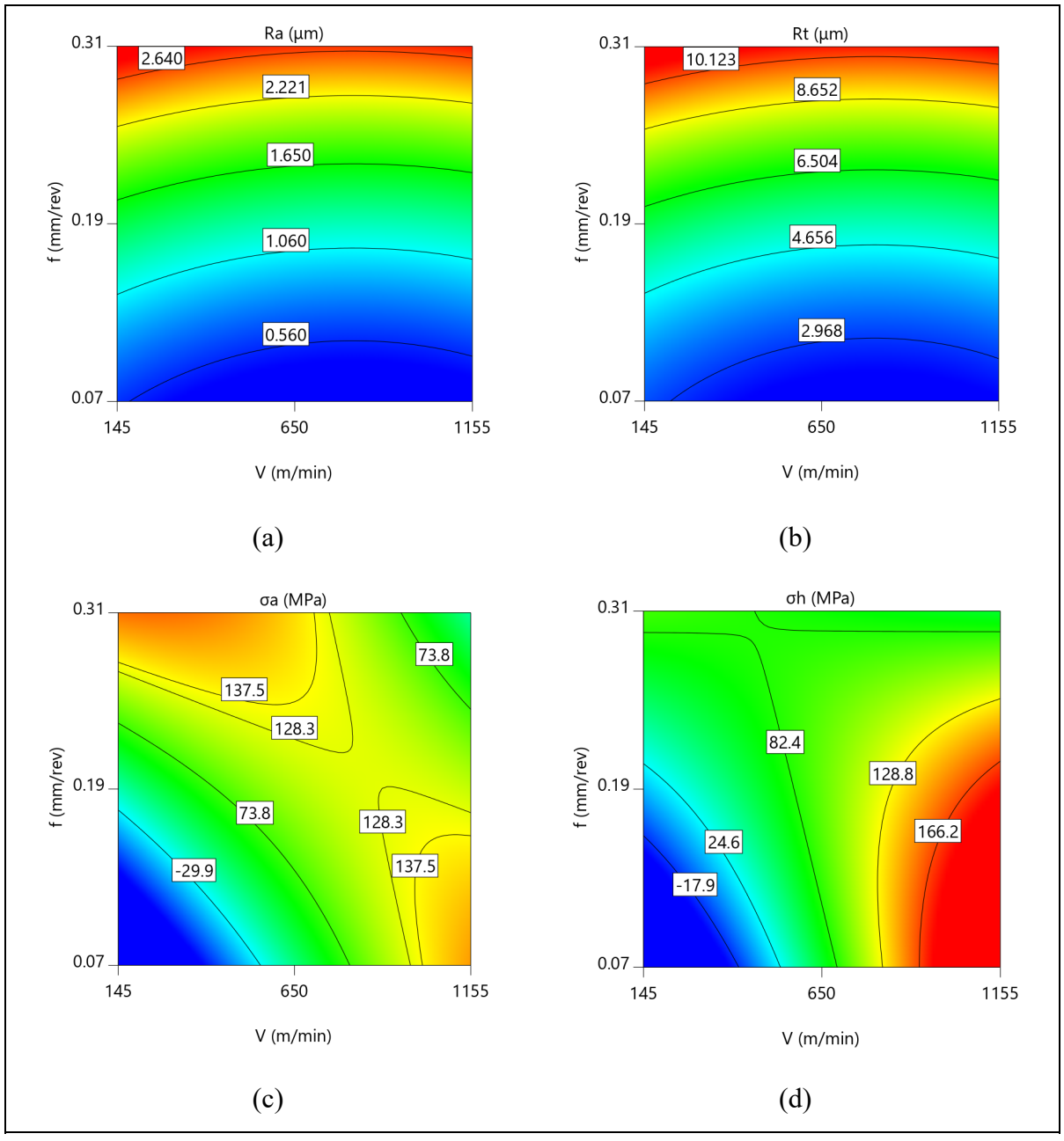

Figure 5.9 Contour plots of surface integrity in WET mode for D=1.64 mm

A comparative study of the optimal values of turning parameters showed that feed rate in all the three modes approached its lowest value equal to 0.07 mm/rev in the DoE, as shown in Table 5.12. The optimal values of cutting speed and depth of cut were the lowest in the DoE for DRY mode. In contrast, higher cutting speed and depth of cut were obtained for MQL and

WET modes, leading to higher material removal rate and more productivity, which is highly suitable for the industry.

Surface roughness parameters in DRY and MQL modes were smaller (better) than those obtained in WET mode, which could be due to higher generated heat and thermal softening of material in DRY and MQL modes, and therefore, less turning forces and tool wear. However, considering both surface roughness and MRR, MQL turning provided the optimum results. On the other hand, MQL and WET modes led to smaller residual stresses compared to DRY mode. This can be attributed to the fact that lubricant and coolant cause higher heat evacuation from the cutting zone by better chip evacuation. Moreover, lubricant and coolant reduce the generated frictional and plastic heats, resulting in lower turning temperature and smaller residual stresses. These results are in agreement with those obtained for turning of AISI 4310 steel by Ji *et al.* (2014). Considering both residual stresses and MRR, WET turning provided the optimal results.

5.6 Summary and conclusion

In the present research work, an experimental study with a broad range of turning parameters was carried out to find the most influential cutting speed, feed rate, and depth of cut on surface integrity characteristics and obtain their optimum values for three environments including DRY, MQL, and WET in LST and HST of AA6061-T6. Based on the ANOVA and optimization studies, several conclusions are drawn. The ANOVA results showed that feed rate was the most influential parameter on both surface roughness parameters for all the turning environments. Furthermore, feed rate had the highest effect on the axial residual stress in DRY mode, whereas both cutting speed and feed rate were significantly effective in MQL and WET modes. In terms of the hoop residual stress, cutting speed was the most influential parameter for all the modes. As a result, feed rate and cutting speed were the most efficient parameters on the surface integrity characteristics. The multi-performance optimization results revealed that the optimum cutting speed, feed rate, and depth of cut were the lowest values in the DoE for DRY mode. The lowest feed rate in the DoE provided the optimum results in all the three

modes. Moreover, larger cutting speed and depth of cut were obtained in MQL and WET turning, which resulted in higher material removal rate and more productivity. Accordingly, based on the ANOVA and multi-criteria optimization, DRY and MQL modes provided lower surface roughness characteristics, whereas MQL and WET modes furnished smaller surface residual stresses and larger MRR. Therefore, in terms of overall surface integrity characteristics and MRR in turning of AA6061-T6, MQL turning environment is suggested, which is also proper to decrease manufacturing costs, protect ecology and environment, and preserve machinist's health.

CHAPTER 6

3D FE MODELLING AND EXPERIMENTAL ANALYSIS OF RESIDUAL STRESSES AND MACHINING CHARACTERISTICS INDUCED BY DRY, MQL, AND WET TURNING OF AA6061-T6

Mahshad Javidikia[1], Morteza Sadeghifar[1], Victor Songmene[1], Mohammad Jahazi[1]

[1]Department of Mechanical Engineering, École de Technologie Supérieure, 1100 Notre-Dame Ouest, Montréal, Québec, Canada H3C 1K3

This article is submitted to "Journal of Machining Science and Technology" in July 2020

6.1 Abstract

The present research study aimed to investigate the influences of turning environments and parameters on machining temperature (MT), machining forces (MFs), and axial surface residual stresses (ASRS) induced by turning operation of AA6061-T6 alloy bar. Turning environments included DRY, minimum quantity lubrication (MQL), and WET modes, and turning parameters consisted of cutting speed (V), feed rate (f), depth of cut (DoC), tool nose radius (r), side cutting edge angle (SCEA), and back rake angle (BRA). A 3D finite element (FE) model was developed to simulate and predict MT, MFs, and ASRS for different turning environments and parameters and was validated by experimental measurements. The results showed that increasing feed rate led to a higher tensile ASRS while using tools with a nose radius of 0.4 mm resulted in lower ASRS. In addition, the deviation of SCEA from 0° to positive or negative values caused higher tensile ASRS. ASRS increased with decreasing BRA from 0° to -15°. Finally, the variation of ASRS was found to be more sensitive to thermal effects than to mechanical effects.

Keywords: Turning Environments and Parameters; Residual Stresses; 3D FE Simulation; AA6061-T6

6.2 Introduction

The machining process is characterized by non-uniform temperatures and machining forces, producing residual stresses (Javidikia *et al.*, 2020a; Javidikia *et al.*, 2020b; Sadeghifar *et al.*, 2018b). For instance, in a turning process, cutting conditions including cutting speed, feed rate, and depth of cut and tool geometry including tool nose radius, side cutting edge angle, and bake rake angle modify the temperature and force patterns inducing residual stresses at the end of the operation. Using FE models enables manufacturers to predict residual stresses without having to conduct a large number of expensive, time-consuming experimental tests and measurements (Sadeghifar *et al.,* 2018b). 2D FE simulations of turning processes for aluminum alloys were investigated by many researchers (Sadeghifar *et al.*, 2018a; Mabrouki *et al.*, 2008; Menezes *et al.*, 2014; Haddag *et al.*, 2015; Daoud *et al.*, 2015a). However, a very small number of 3D FE simulations of turning processes were carried out during the last decade.

Jafarian (2019) developed a 3D finite element model of the dry turning process of Inconel 718 using the DEFORM^{TM} software to predict machining temperature and residual stress distribution. The results showed that the maximum compressive residual stress in the deep layers of the machined workpiece decreased with increasing the depth of cut from 0.2 to 0.8 mm. However, the effects of different turning environments on residual stress results were not investigated. Elsheikh *et al.* (2019) studied the influence of cutting speed, feed rate, depth of cut, and tool nose radius on surface residual stress in dry turning of AISI 1035 steel. The simulations were carried out using the AdvantEdge^{TM} software. The results showed that an increase in tool nose radius, feed rate, and depth of cut resulted in higher tensile residual stresses, whereas an increase in cutting speed led to decreasing tensile residual stresses. However, the effects of different turning environments and tool geometry such as side cutting edge angle and back rake angle on surface residual stress were not studied.

Özel et Ulutan (2012) carried out 3D FE simulations of dry turning of Ti-6Al-4V and IN100 alloys using the DEFORM^{TM} software to study the effects of different tool geometry parameters and coatings on residual stresses. They concluded that the predicted residual stresses became more compressive with increasing cutting edge radius and more tensile on the

surface region due to the presence of coating. It needs mentioning that the influence of turning environment on residual stresses was not analyzed.

Navas *et al.* (2012) conducted an experimental investigation on the effect of cutting speed, feed rate, and tool nose radius on surface residual stresses after turning of AISI 4340 steel. Their results demonstrated that decreasing feed rate and increasing cutting speed resulted in lower tensile surface residual stress levels in machined AISI 4340 steel. They also found that a smaller tool nose radius significantly decreased surface tensile residual stresses. However, surface residual stresses were not predicted using a 3D finite element model. In addition, the influence of turning environments on superficial residual stresses was not studied.

Attanasio *et al.* (2009) used the DEFORM^{TM} software to conduct 3D FE modeling simulations of dry turning of AISI 1045 steel to predict the effect of feed rate and tool nose radius on residual stresses. The simulation results showed that using a smaller tool nose radius and a lower feed rate resulted in decreasing superficial residual stresses. Outerio *et al.* (2008) carried out experimental research on the impacts of feed rate and cutting speed on residual stress generated by dry turning of Inconel 718 and AISI 316L steel. A 3D finite element model was also developed using DEFORM^{TM} software to predict machining forces and temperature. They concluded that feed rate strongly affected residual stresses. However, residual stresses were not simulated and the influence of turning environment on residual stresses was not studied.

The above review of the literature shows that a comprehensive experimental-finite element analysis of residual stresses induced by turning processes for various turning environments including DRY, MQL, and WET modes was not carried out. In the present work, the effects of turning environments and parameters on machining temperature, forces, and axial surface residual stress induced by turning AA6061-T6 were studied. Turning parameters consisted of cutting speed, feed rate, depth of cut, tool nose radius, side cutting edge angle, and back rake angle. The developed 3D FE model was experimentally validated using machining forces and residual stresses. The variations of axial surface residual stress with turning environments, cutting conditions, and tool geometry parameters are analyzed and discussed.

6.3 Materials and experimental methods

Turning tests were conducted on a MAZAK CNC machine for the three turning environments, as displayed in Figure 6.1(a) and Figure 6.1(b). The workpiece was a solid cylinder with a diameter of 75 mm and a length of 120 mm made of AA6061-T6. The cutting insert was an uncoated carbide with the designation of ISO CNMG 120408-THM, providing a nose radius of 0.8 mm. A KENNAMETAL right-hand tool holder (DCLNR 2020 K12) was used to hold the inserts with SCEA and BRA equal to -5^{o}. A new insert and component were used for each turning experiment listed in Table 6.1. MFs were measured using a Kistler (type 9121) three-component piezoelectric dynamometer. The acquisition of force signals was performed with a LabVIEW software and data were analyzed using MATLAB codes. A Tecnolub lubricating system model SLS1.2-2 was used to apply MQL during the turning process. The utilized cutting fluids for MQL and WET modes were Microkut 400 and Oemeta coolant with the flow rate of 21.5 and 7200 ml/min, respectively.

Surface residual stress in the axial direction was measured using a Pulstec μ-X360n X-Ray Diffraction machine (Figure 6.2(a)), which uses Debye-Scherrer ring image based on a diffracted cone (Figure 6.2(b)) and cos α method to measure and calculate residual stresses (Sadeghifar, 2017). In addition, X-Ray incidence angle and X-Ray irradiation time were selected as 25 degrees and 30 s, respectively. Bragg's angle and crystallographic plane were 139.3 degrees and {311}, respectively. Residual stress was measured on all the machined samples at two points located 3 cm from the front edge of the sample.

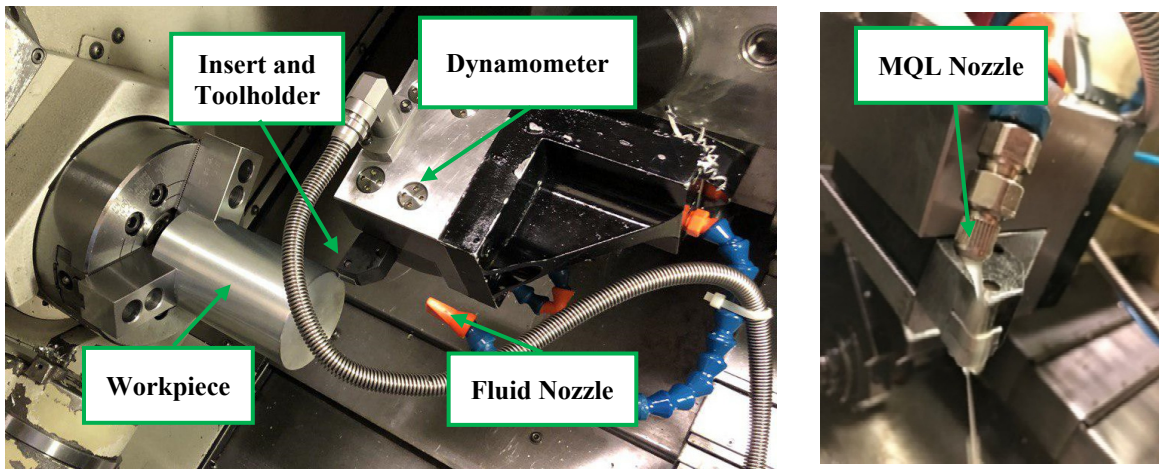

Figure 6.1 The experimental set-up of the turning process: (a) DRY and WET modes and (b) MQL mode

Table 6.1 Turning tests and parameters

Test No.	Cutting speed $V\ (m/min)$	Feed rate $f\ (mm/rev)$	Depth of cut $D\ (mm)$
1	650	0.19	1.5
2	650	0.07	1.5
3	145	0.19	1.5
4	650	0.31	1.5
5	650	0.19	2.34
6	650	0.19	0.66
7	1155	0.19	1.5

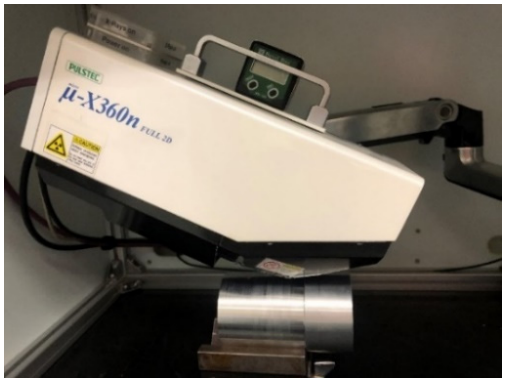

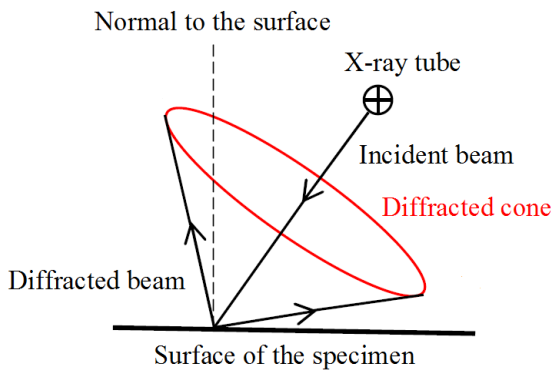

(a) (b)

Figure 6.2 Surface residual stress measurement: (a) A Pulstec μ-X360n XRD machine and (b) A Debye-Scherrer ring image based on a diffracted cone (Sadeghifar, 2017)

6.4 3D Finite element modeling

In the present study, finite element method was utilized to simulate the turning process of AA6061-T6 using the DEFORM^{TM} software. The mathematical formulation of the analysis is based on an updated Lagrangian formulation and implicit integration method for large plastic deformations.

The equations of motion during the turning process can be expressed at a specific instant of time as (Javidikia *et al.*, 2020b; Sadeghifar *et al.*, 2018b):

$$[M]\{\ddot{U}\} + \{R_{\text{int}}\} = \{R_{ext}\} \tag{6.1}$$

where $[M]$ is the mass matrix, $\{\ddot{U}\}$ is the acceleration vector ($\{U\}$ is the displacement), and $\{R_{\text{int}}\}$ and $\{R_{ext}\}$ are the vectors of internal and external forces, respectively. The influence of damping is neglected (Sadeghifar *et al.,* 2018b), and therefore, $\{R_{\text{int}}\}$ equals:

$$\{R_{\text{int}}\} = [C_d]\{\dot{U}\} + [K_s]\{U\} \cong [K_s]\{U\} \text{ where } [C_d] \cong 0 \tag{6.2}$$

in which $[C_d]$ and $[K_s]$ are the damping and stiffness matrices, respectively. $\{R_{ext}\}$ is related to the external forces applied during cutting including the reaction forces at the supports.

Heat transfer occurring during the machining process is expressed as (Javidikia *et al.*, 2020b; Sadeghifar *et al.*, 2018b):

$$[C_T]\{\dot{T}\} + [K_T]\{T\} = \{\dot{Q}_g\} \tag{6.3}$$

where $[C_T]$ and $[K_T]$ are the volumetric heat capacitance and thermal conduction matrices, respectively. $\{\dot{Q}_g\}$ is also the total heat generation in the machining process.
The thermal contact between the tool and workpiece was defined using the heat transfer through the tool-chip contact faces from the chip to the tool during the turning process which is calculated as (Javidikia *et al.*, 2020b; Sadeghifar *et al.*, 2018b):

$$Q = h_{\text{int}}\,(T_{wp} - T_t) \tag{6.4}$$

where h_{int} is heat transfer coefficient, T_{wp} and T_t are the workpiece and tool's temperature at the tool-chip interface. A heat transfer coefficient of $10^7\ W/m^2\ ^oC$ was calibrated for modeling and an initial temperature of $20\ ^oC$ (room temperature) was applied to both tool and workpiece. It needs mentioning that the heat transfer coefficient was calibrated when the steady-state condition for MT was reached. The high value was selected because the high pressure of the chip on the tool rake faces makes a perfect contact between the tool and chip (Sadeghifar *et al.*, 2018a). Another reason was to quickly reach the steady-state condition in order to shorten the machining time and avoid excessive distortion of elements (Sadeghifar *et al.*, 2018a).

The convection heat transfer takes place between the workpiece surface and the ambient according to the following formula (Javidikia *et al.*, 2020b; Sadeghifar *et al.*, 2018b):

$$Q = h\ (T_{wp} - T_a) \tag{6.5}$$

in which h is convection heat transfer coefficient, and T_a is the ambient (room) temperature.

The Johnson-Cook constitutive equation was used for modeling plastic deformation of the workpiece material as follows:

$$\bar{\sigma} = [A + B(\varepsilon)^n]\left[1 + C\ln\left(\frac{\dot{\varepsilon}}{\dot{\varepsilon}_0}\right)\right]\left[1 - \left(\frac{T - T_{room}}{T_{melt} - T_{room}}\right)^m\right] \quad (6.6)$$

where σ_{fl} is the flow stress of the workpiece material, ε is the plastic strain, $\dot{\varepsilon}$ the plastic strain rate (s^{-1}), $\dot{\varepsilon}_0$ the reference plastic strain rate (s^{-1}), $T(\,^oC)$ the workpiece temperature, $T_{melt}\,(\,^oC)$ the melting temperature of the workpiece, and $T_{room}(\,^oC)$ the room temperature. Moreover, $A\ (MPa)$ is the initial yield strength, $B\ (MPa)$ the hardening modulus, C the strain rate sensitivity coefficient, n the hardening coefficient, and m the thermal softening coefficient. Table 6.2 lists the Johnson-Cook constants of AA 6061-T6.

Table 6.2 The constants of the Johnson-Cook material model of aluminum alloy 6061-T6 (Daoud *et al.*, 2014)

$A\ (MPa)$	$B\ (MPa)$	n	C	m	$\dot{\varepsilon}_0\ (1/s)$	$T_{melt}\,(\,^oC)$	$T_{room}\,(\,^oC)$
250	79.70	0.499	0.0249	1.499	1	652	20

Modeling of frictional behavior at the tool-workpiece contact areas is a challenging task in finite element simulations of metal cutting processes. Previous research showed that aluminum alloys tend to adhere to the tool at the tool-chip interface during cutting (Roy *et al.*, 2009), creating a sticking zone. The Coulomb and Zorev models are not capable of predicting the frictional behavior precisely since there is no relative sliding at the tool-chip interface. The mechanical contact between the tool and the workpiece was modeled using the shear friction model as follows (Javidikia *et al.*, 2020b; Sadeghifar *et al.*, 2020):

$$\tau = m\tau_Y \quad (6.7)$$

where m is the shear friction factor and τ_Y is the shear flow stress in the chip at the tool-chip interface. A shear friction model was used by calibrating and comparing the present simulated machining forces and residual stresses with the corresponding experimental results.

Cutting fluids have two main functions in machining processes including cooling and lubricating. For the lubricating effect, mostly, cutting fluids decrease the friction at the tool-chip interface, while for the cooling effect, cutting fluids increase the convection heat transfer. MQL and WET modes play mostly lubricating and cooling roles, respectively. A heat convection cube was utilized in the FE modeling of MQL turning to include the influence of the lubricant around the tool tip, as shown in Figure 6.3.

For the simulation purposes, the workpiece with an elastic-plastic behavior was meshed with 45000 tetrahedral elements. The tool material was considered as a rigid body and was meshed with 35000 tetrahedral elements. Mesh windows were assigned to the workpiece in order to have a high-quality fine mesh in the machined workpiece. The workpiece and tool's material properties are given in Table 6.3. Residual stresses were modeled in two steps: cutting process and stress relaxation process. In the first step, cutting is carried out to reach the steady-state condition in which MFs, MT, strains and stresses, and chip thickness remain almost constant with time. During the stress relaxation step, the tool was retracted and the mechanical BCs Vx = Vy = Vz = 0 were removed from the side faces of the workpiece so as to allow the workpiece material to relax by cooling down to room temperature. This cooling process was carried out using a convection heat transfer to the workpiece including the chip (Sadeghifar *et al.*, 2018b). The mechanical and thermal boundary conditions for cutting and stress relaxation steps for DRY, MQL, and WET environments are displayed in Figure 6.4.

Table 6.3 Mechanical and thermal properties of the workpiece and tool

Properties	AA6061-T6 (Javidikia *et al.*, 2020b)	Uncoated carbide (DEFORM™ Software, 2017)
Density $\rho\ (kg/m^3)$	2700	11900
Young's modulus $E\ (GPa)$	58.5	650
Poisson's ratio υ	0.33	0.25
Conductivity $k\ (W/m\ ^oC)$	167	59
Specific heat capacity $c\ (J/kg\ ^oC)$	896	337
Thermal expansion coefficient $\alpha\ (1/\ ^oC)$	23.5×10^{-6}	5×10^{-6}

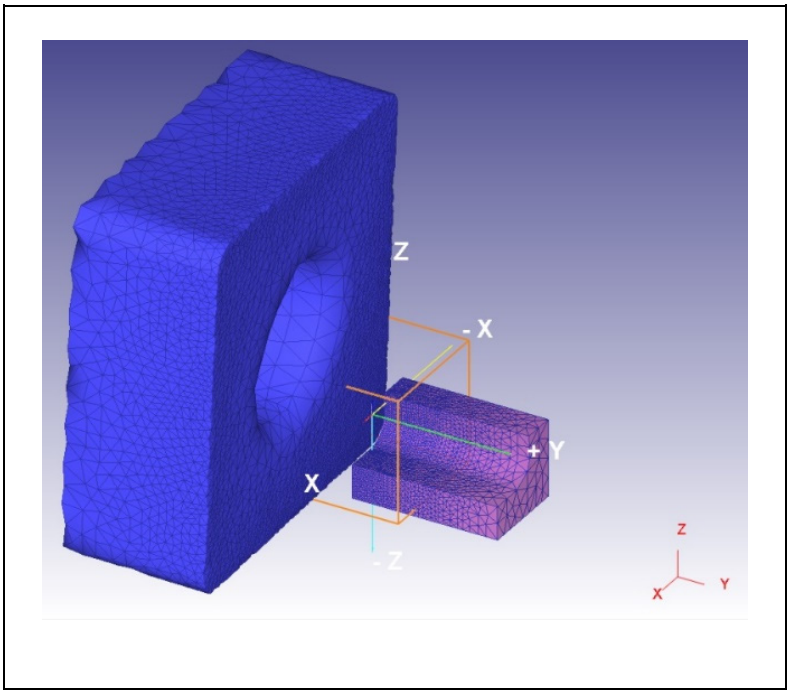

Figure 6.3 Heat convection cube in the FE modeling of MQL turning

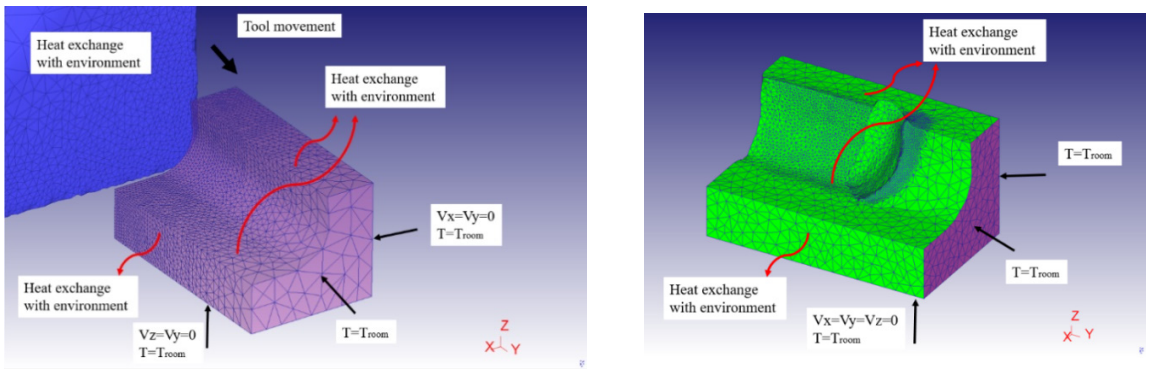

(a) (b)

Figure 6.4 Thermal and mechanical boundary conditions in the FE model for (a) the cutting process and (b) the stress relaxation process

6.5 Results and discussion

6.5.1 Residual stress measurement

6.5.1.1 Interaction between turning environment and feed rate

The influence of turning environment and feed rate on axial surface residual stress was studied for Test Nos. 1, 2, and 4, whose cutting speed and depth of cut were fixed at 650 m/min and 1.5 mm, respectively. Feed rate was the most significant parameter affecting ASRS for all environmental modes (Javidikia *et al.*, 2020a). As shown in Figure 6.5, ASRS increased with feed rate for all the modes. In a turning process, an increment in feed rate increases the tool-chip contact area and the frictional heat, which increases temperature and residual stresses. In contrast, an increment in feed rate raises material removal rate (MRR, $V \times f \times D$), which increases the heat evacuation by the chip from the workpiece, and as a result, can decrease temperature and residual stresses (Javidikia *et al.*, 2020b; Sadeghifar *et al.*, 2018b; Pawade *et al.*, 2008). Therefore, in a machining process, the magnitude of residual stresses depends significantly on the competition between these two phenomena (Javidikia *et al.*, 2020b;

Sadeghifar *et al.*, 2018b; Pawade *et al.*, 2008). For the present range of feed rate, the first phenomenon occurred, where residual stresses rose with increasing feed rate. This occurs depending on the values of cutting conditions and tool geometry parameters as well as tool and workpiece materials. In addition, this result is in agreement with those obtained in turning of steels reported by (Capello, 2005; Leppert et Peng, 2012).

For feed rate between 0.07 and 0.19 mm/rev, ASRS was almost the same for all the environments. Moreover, the smallest ASRS was obtained at the lowest feed rate of 0.07 mm/rev for all the modes. It is observed that the highest value of ASRS, 163 MPa, was reached at the feed rate of 0.31 mm/rev in DRY mode. In contrast, the smallest ASRS value of 38 MPa took place at the feed rate of 0.07 mm/rev in MQL mode. Therefore, MQL turning at the feed rate of 0.07 mm/rev is proposed in order to minimize ASRS levels.

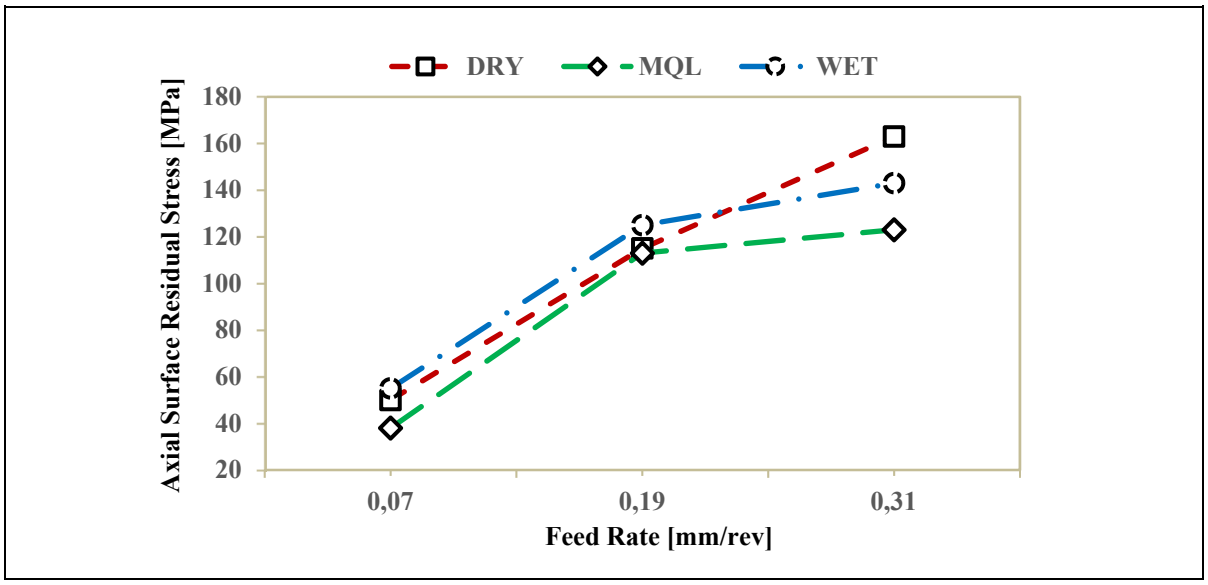

Figure 6.5 Influence of turning environment and feed rate on ASRS

6.5.1.2 Interaction between turning environment and depth of cut

The impact of turning environment and depth of cut on axial surface residual stress was examined for Test Nos. 1, 5, and 6, whose cutting speed and feed rate were fixed at 650 m/min and 0.19 mm/rev, respectively. Figure 6.6 illustrates that for DRY, MQL, and WET modes,

ASRS first remained almost unaffected between the depth of cut of 0.66 to 1.5 mm and then decreased from the depth of cut of 1.5 to 2.34 mm. In a turning process, an increase in depth of cut increases the tool-chip contact area and the frictional heat being entrapped in the cutting zone, increasing temperature and residual stresses. This is in agreement with (Arunachalam *et al.*, 2004), where an increase in the depth of cut raised the residual stresses in tensile direction. This was attributed to the fact that Inconel 718 has a poor thermal conductivity, leading most of the heat to be entrapped in the cutting zone, and as a result, increasing temperature and the tensile character of residual stresses (Arunachalam *et al.*, 2004). On the other hand, an increase in depth of cut raises MRR, which increases the heat evacuation, and consequently, can decrease temperature (Javidikia *et al.*, 2020b; Sadeghifar *et al.*, 2018b; Pawade *et al.*, 2008) and residual stresses (Capello, 2005; Leppert et Peng, 2012). As a result, the magnitude of residual stresses depends considerably on this competition between these two phenomena. For the present range of depth of cut, in the first interval from 0.66 to 1.5 mm, the two phenomena have the same contributions to the creation of residual stresses, and as a result, the residual stresses remained unaffected. In the second interval of depth of cut, the second phenomenon dominated, declining residual stresses with increasing depth of cut.

In addition, the largest ASRS equal to 128 MPa was obtained at the lowest depth of cut equal to 0.66 mm in WET mode, while the lowest ASRS was achieved at the depth of cut of 0.66 mm for DRY and WET modes. As a result, DRY and WET turning at the depth of cut of 2.34 mm is proposed to obtain low values of ASRS.

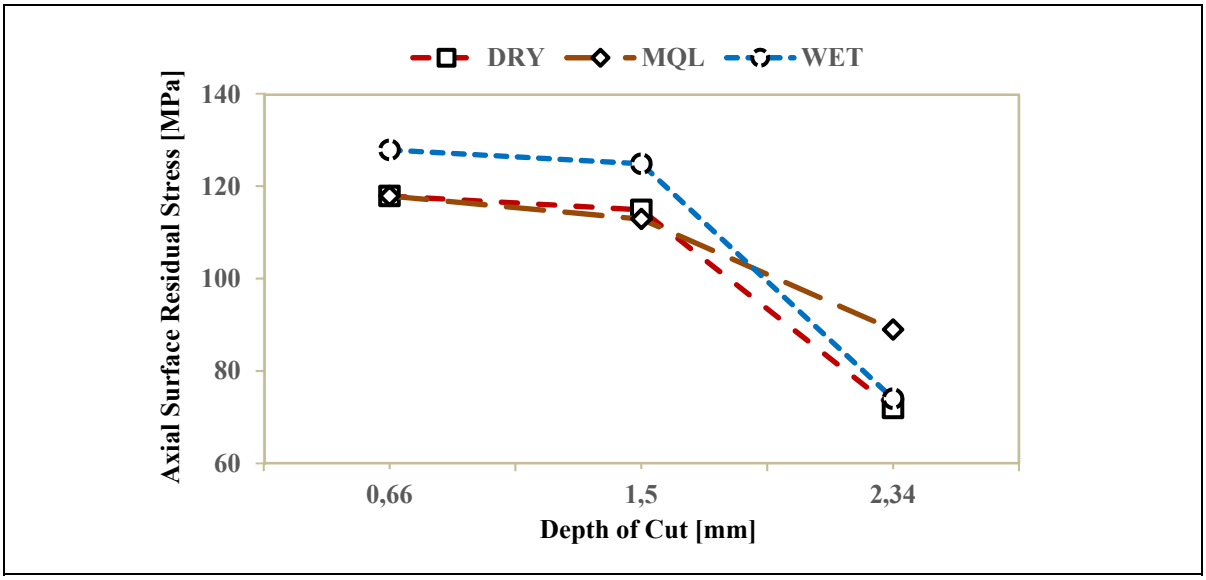

Figure 6.6 Influence of turning environment and depth of cut on ASRS

6.5.1.3 Interaction between turning environment and cutting speed

The effect of lubrication mode and cutting speed on surface integrity was investigated using Test Nos. 1, 3, and 7, whose feed rate and depth of cut were fixed at 0.19 mm/rev and 1.5 mm, respectively. Figure 6.7 shows that ASRS increased with cutting speed in the range of 145 to 650 m/min for DRY, MQL, and WET. For cutting speed between 650 to 1155 m/min, ASRS increased for MQL, while it decreased in WET mode. In addition, ASRS remained almost the same for DRY. In a turning process, an increment in cutting speed raises the plastic work $\sigma_{fl}\dot{\varepsilon}_p$ and the frictional work τV_{Ch} (Sadeghifar *et al.*, 2018b), in which σ_{fl}, $\dot{\varepsilon}_p$, τ, and V_{Ch} are flow stress, effective plastic strain rate, frictional shear stress at the tool-chip contact face, and chip velocity along the tool-chip interface, respectively. These works augment the generated heat, and as a result, can increase the temperature and residual stresses. In contrast, an increment in cutting speed increases material removal rate (MRR), which increases the heat evacuation, and consequently, can decrease temperature (Javidikia *et al.*, 2020b; Sadeghifar *et al.*, 2018b; Pawade *et al.*, 2008) and residual stresses (Sadeghifar *et al.*, 2018b; Pawade *et al.*, 2008; Moussa *et al.*, 2012). The competition between these two phenomena determines the magnitude of residual stresses. For the first interval of cutting speed under study, the first

phenomenon occurred for all the modes, where residual stresses rose with increasing cutting speed. In the second interval of cutting speed, the two phenomena have the same contributions to the creation of residual stresses for DRY mode, whereas the first and second phenomena dominated in MQL and WET modes, respectively.

It is also observed that the cutting speed of 145 m/min provided the lowest ASRS for all the turning environments. In addition, the largest value of ASRS equal to 143 MPa was observed at the cutting speed of 1155 m/min in MQL mode, while the lowest value of ASRS equal to 51 MPa was obtained at 145 m/min for WET mode. Therefore, WET turning at the cutting speed of 145 m/min is proposed to obtain small values of ASRS.

6.5.2 Validation of the FE model

The developed 3D finite element model was validated by comparing the present numerical results of radial force (F_r), feed force (F_f), cutting force (F_c), and ASRS with those obtained through experimental measurements in DRY, MQL, and WET modes for two turning parameters listed in Table 6.4. As shown in Figure 6.8, a good agreement exists between the predicted and measured MFs. Previous research (Javidikia *et al.*, 2020b; Sadeghifar *et al.*, 2018b; Sadeghifar *et al.*, 2018a; Outeiro *et al.*, 2008; Yen *et al.*, 2004; Filice *et al.*, 2007) showed that the discrepancy between one of the predicted and measured MFs is unavoidable due to lack of precise frictional models. Figure 6.9 displays the simulated and measured MFs of Test No. 4 in WET mode, where the steady-state condition can be observed.

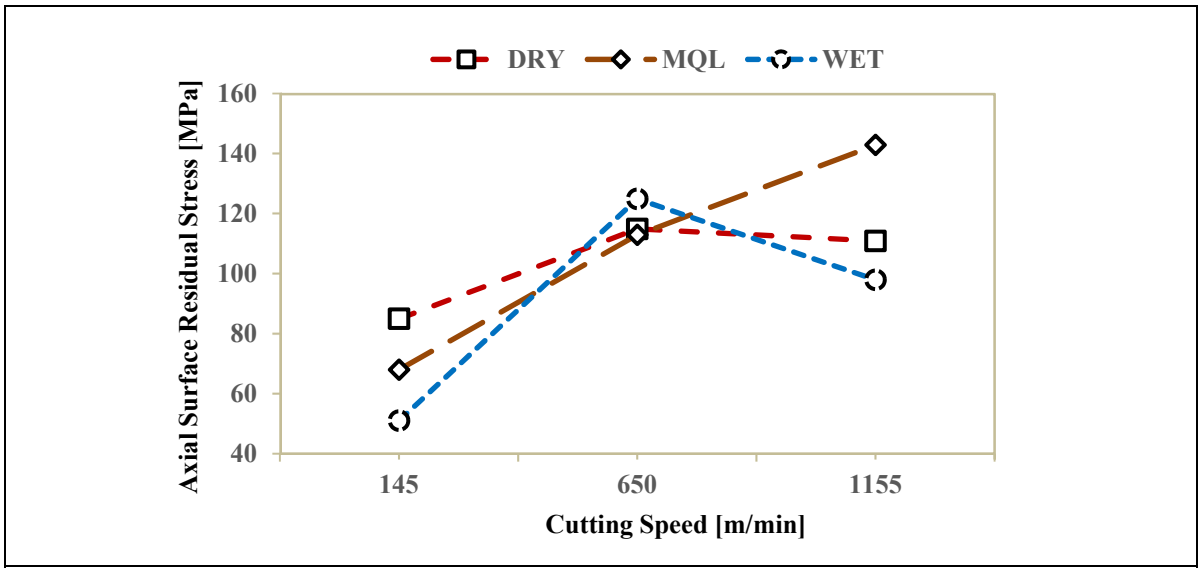

Figure 6.7 Influence of turning environment and cutting speed on ASRS

Moreover, as shown in Figure 6.10, the predicted and measured ASRS in DRY, MQL, and WET modes were reasonably matched. This was obtained by exploring different values of shear friction factor and heat transfer coefficient and selecting proper coefficients using calibration of the FE results with the experimental ones, as shown in Table 6.5. It needs mentioning that in the present study, a heat transfer convection coefficient of 20 $kW/(m^2°C)$ for WET mode, which was numerically calibrated by Ahmad Shahir bin Jamaludin (2017), was used for FE predictions. In addition, the distribution of simulated ASRS in the machined surface for Test Nos. 1 and 4 in DRY, MQL, and WET modes are shown in Figure 6.11 and Figure 6.12. ASRS was calculated by averaging five values in several locations in the 'validation' zone on the machined surface. The 'validation' zone in the workpiece to extract residual stresses in FE simulations was considered at the mid-length of the machined surface. It must be emphasized that the 'validation' zone is far enough both from the chip root to exclude the local effect produced by the tool nose at the chip root and from the front side of the workpiece to avoid the influence of the boundary condition as well as the transient effects in the beginning of the turning process (Sadeghifar et al., 2018b; Sadeghifar et al., 2018a; Sadeghifar, 2020). An additional reason for choosing the middle zone of the workpiece was to have enough cutting length to reach the steady-state condition (Sadeghifar et al., 2018a; Sadeghifar et al., 2018b; Sadeghifar et al., 2020).

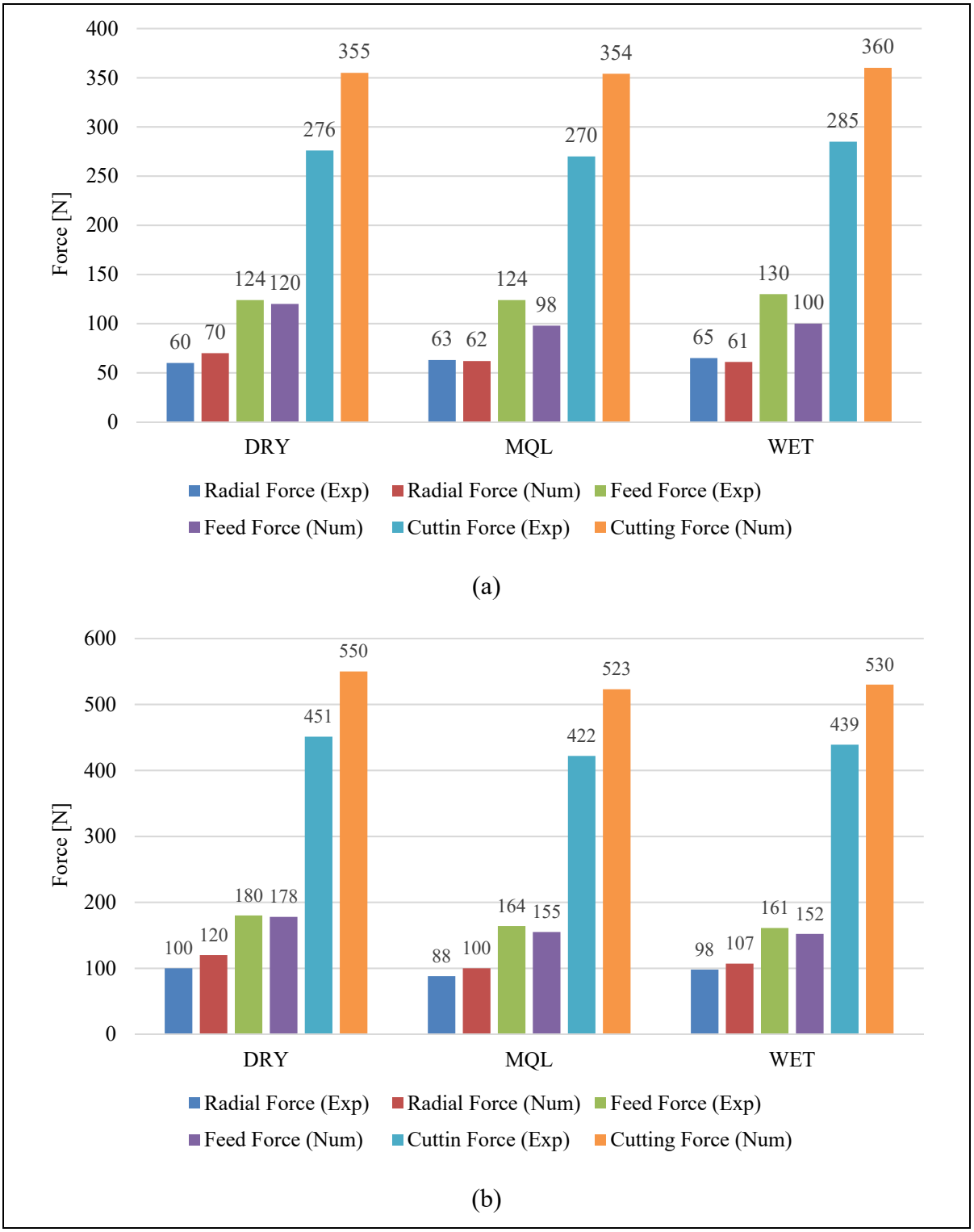

Figure 6.8 Validation of machining forces of the FE results (Num) with the experimental ones (Exp) for (a) Test No. 1 and (b) Test No. 4

Table 6.4 Turning parameters and tool geometry for validation tests

Test No.	V (m/min)	f (mm/rev)	D (mm)	r (mm)	SCEA (deg)	BRA (deg)
1	650	0.19	1.5	0.8	-5	-5
4	650	0.31	1.5	0.8	-5	-5

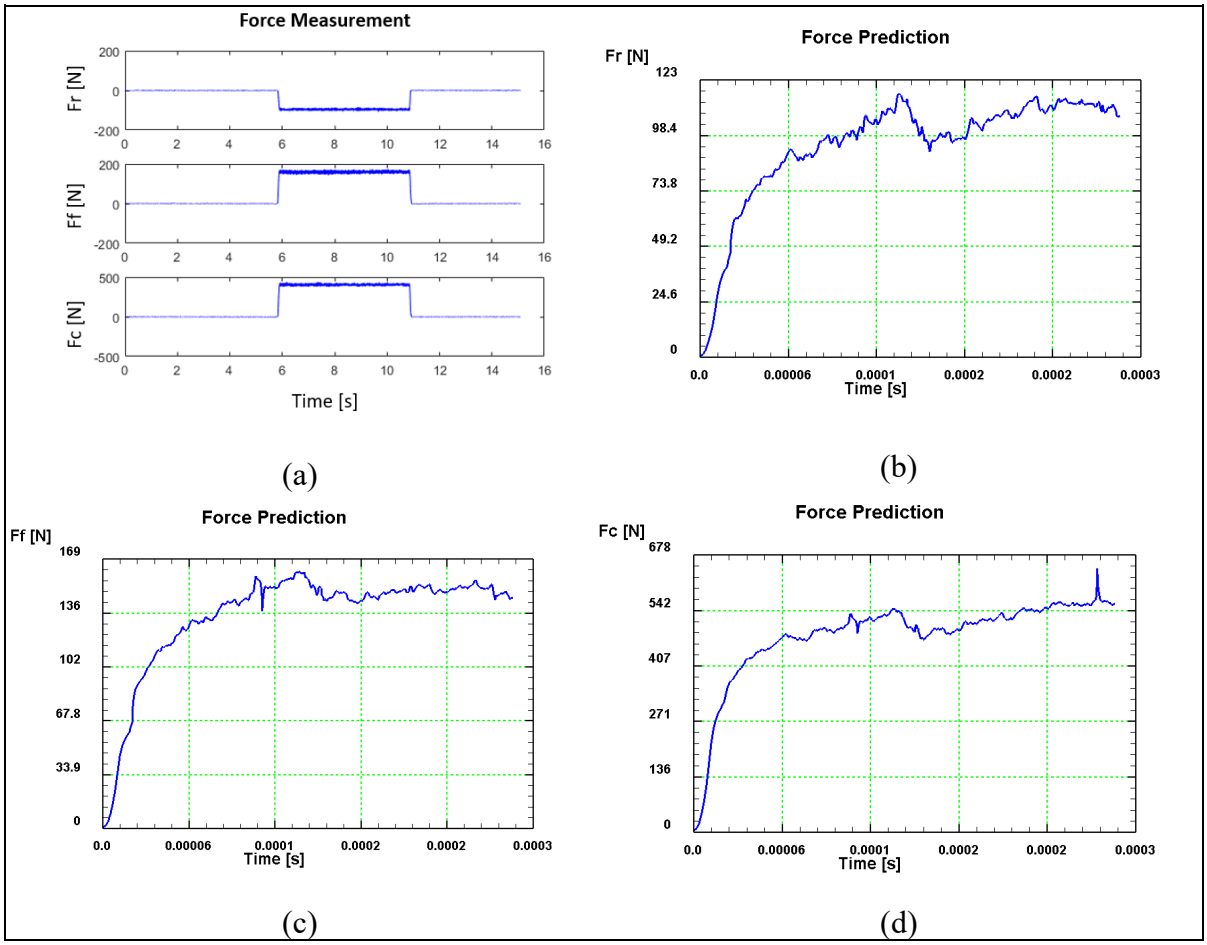

Figure 6.9 Variation of radial, feed, and cutting forces with time during the turning process for Test No. 4 in: (a) the experiment (force signals) and (b,c,d) the FE simulation

Table 6.5 The calibrated frictional and thermal coefficients in the FE models

	DRY	MQL	WET
Shear Friction Factor	0.5	0.43	0.45
Heat Transfer Coefficient $[kW/(m^2°C)]$	10000	10000	10000
Heat Convection Coefficient $[kW/(m^2°C)]$	0.02	3	20

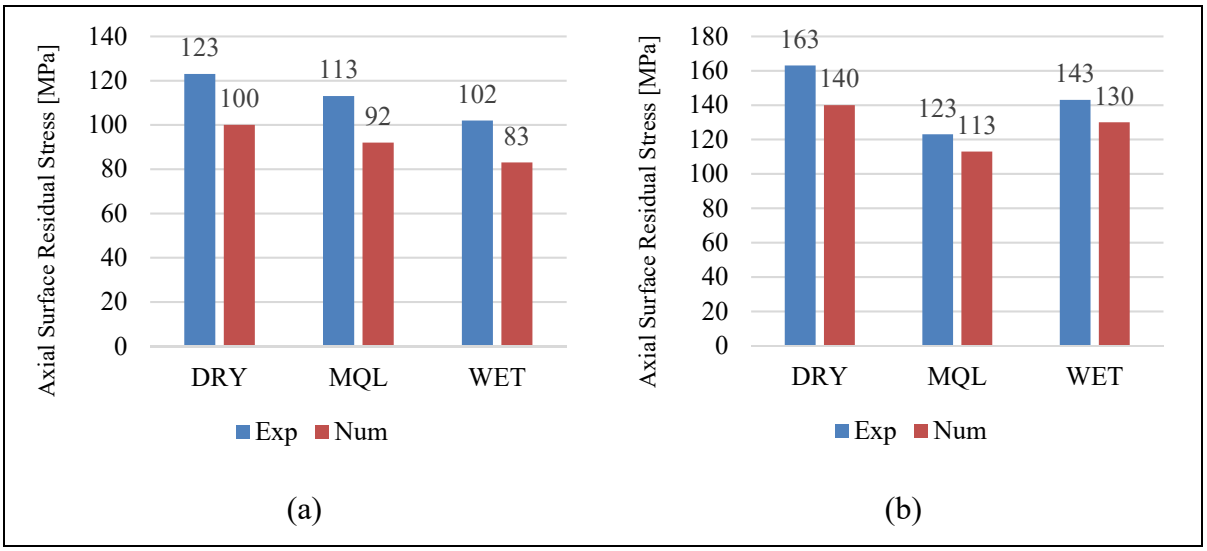

Figure 6.10 Validation of the FE results of ASRS with the experimental ones for: (a) Test No. 1 and (b) Test No. 4

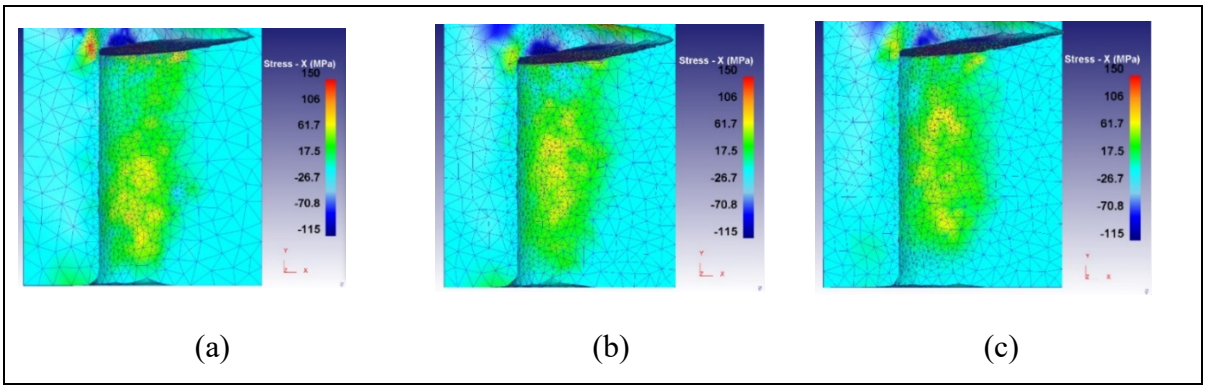

Figure 6.11 The distribution of simulated ASRS in the machined surface for Test No. 1 in: (a) DRY, (b) MQL, and (c) WET modes

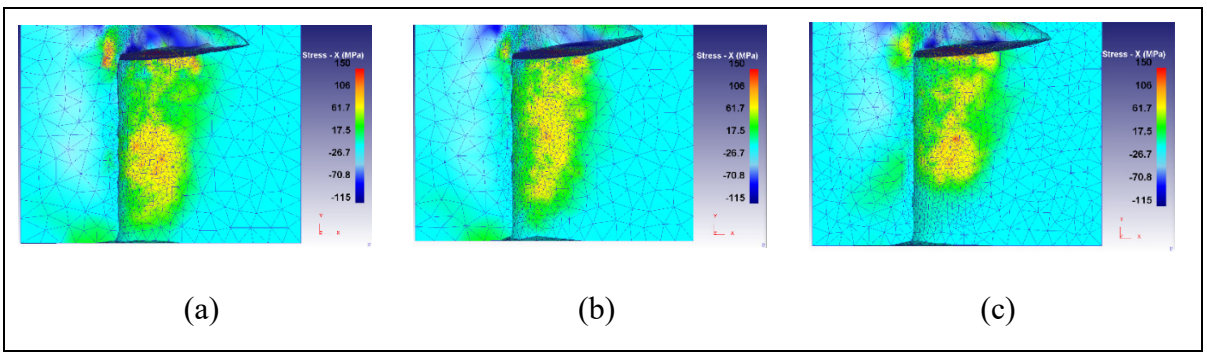

Figure 6.12 The distribution of simulated ASRS in the machined surface for Test No. 4 in: (a) DRY, (b) MQL, and (c) WET modes

6.5.3 Machining characteristics and residual stress prediction

In a previous experimental research study by the same authors (Javidikia *et al.*, 2020a), it was found that WET turning provided optimal surface residual stress and material removal rate in comparison with Dry and MQL environments. Consequently, the effect of tool geometry parameters including tool nose radius, side cutting edge angle, and back rake angle on machining characteristics including machining forces and temperature and axial surface residual stress induced by WET turning of AA6061-T6 was investigated using FE simulations and presented below.

6.5.3.1 Influence of tool nose radius

The influence of tool nose radius including 0.2, 0.4, 0.8, and 1.2 mm on MFs, MT and ASRS was studied for Test No. 1. The different tool nose radii and the FE simulated ASRS are shown in Figure 6.13 and Figure 6.14, respectively. In addition, the predicted values of MFs, MT and ASRS are provided in Table 6.6. As observed in Table 6.6, the lowest value of ASRS was obtained for the nose radius of 0.4 mm, where the resultant of MFs was the largest and MT was the lowest. This result is in agreement with the superficial residual stress experimentally obtained for wet turning of aluminum alloys by Boulahmi (2015), where different tool geometry and material and also cutting conditions were utilized. In contrast, the nose radius of 0.2 mm provided the highest magnitude of ASRS, where the resultant of MFs had the smallest magnitude and MT was the highest. Therefore, the tool with the nose radius of 0.4 mm was selected for further analysis. The FE predicted MT for the nose radius of 0.4 mm is displayed in Figure 6.15.

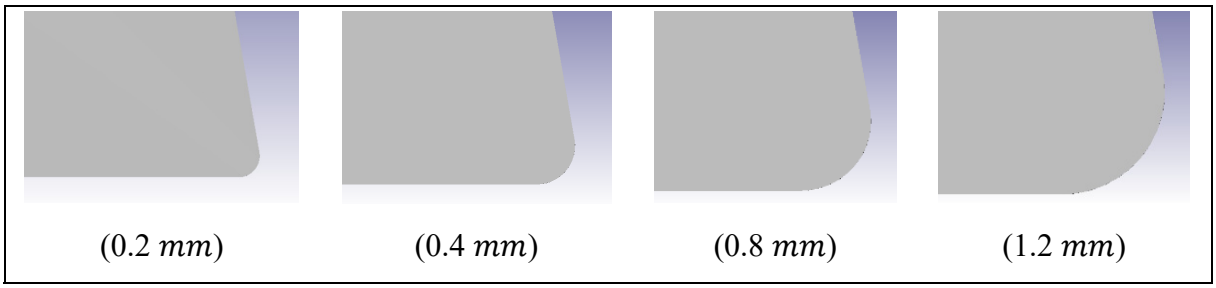

Figure 6.13 Different tool nose radii

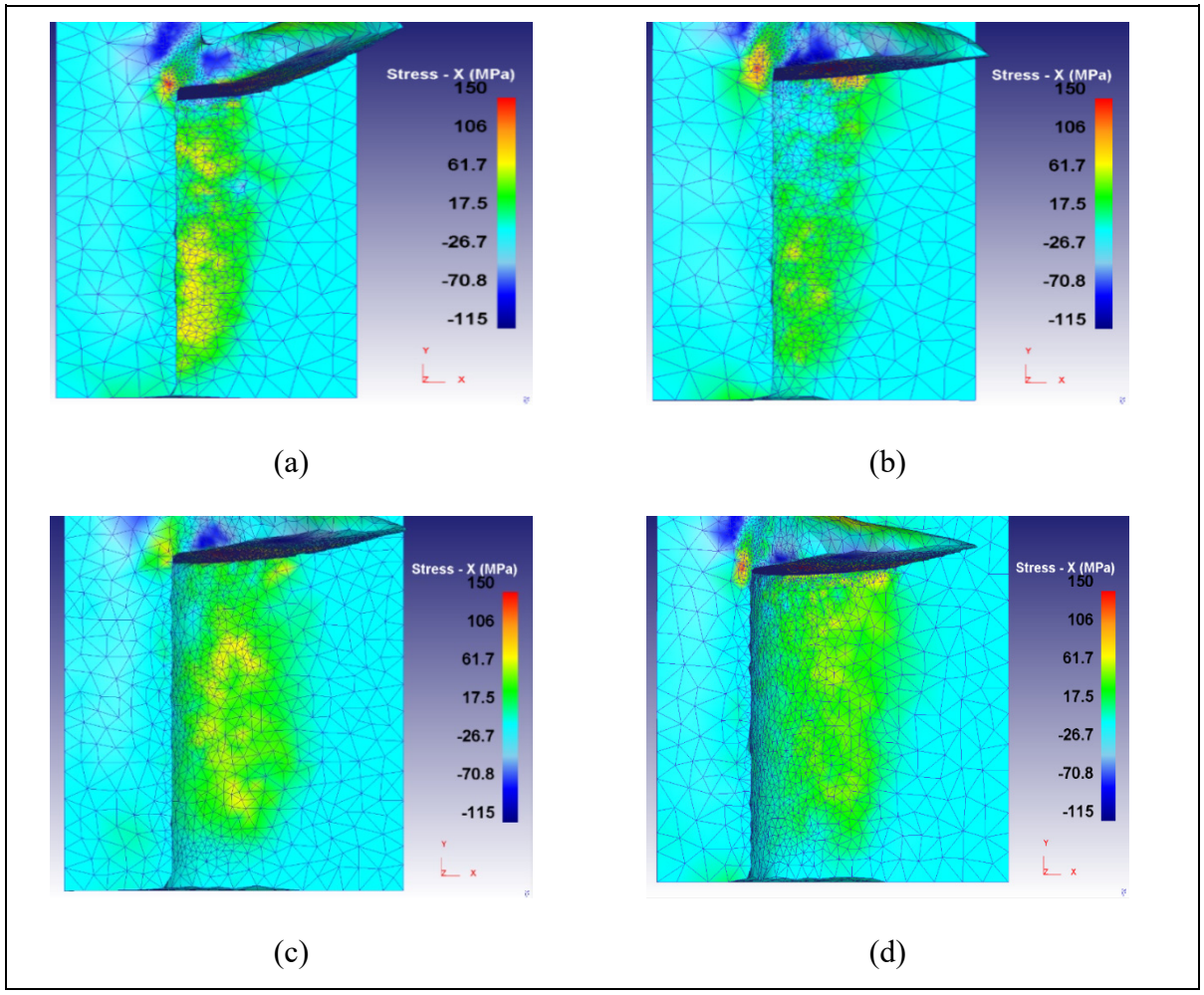

Figure 6.14 The distribution of simulated ASRS in the machined surface for Test No. 1 for the nose radius of (a) 0.2 mm, (b) 0.4 mm, (c) 0.8 mm, and (d) 1.2 mm

Table 6.6 The FE predicted MFs, MT, and ASRS for different nose radii

$r\ [mm]$	$F_r\ [N]$	$F_f\ [N]$	$F_c\ [N]$	T [°C]	ASRS $[MPa]$
0.2	45	83	327	526	101
0.4	67	124	400	419	38
0.8	61	106	360	505	83
1.2	79	97	388	494	61

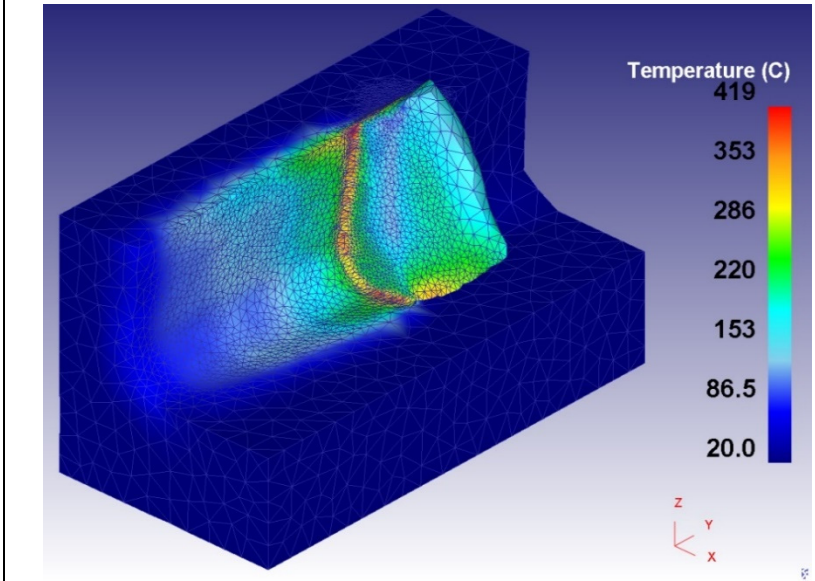

Figure 6.15 The FE predicted MT for the nose radius of 0.4 mm

In a turning process, increasing tool nose radius increases the contact area and the frictional heat at the tool-chip-workpiece interfaces, yielding higher MT and more thermal softening of material, which can result in smaller MFs and higher residual stresses. On the other hand, by increasing tool nose radius, the heat transfer from the workpiece to the tool rises, resulting in less heat accumulation in the workpiece, which can produce lower MT and higher MFs (Sadeghifar *et al.*, 2020), and smaller residual stresses. Therefore, the magnitude of machining characteristics and residual stresses depend on the competition between these two phenomena.

6.5.3.2 Influence of side cutting edge angle

The influence of SCEA including -5º, 0º, 10º, and +15º on MFs, MT and ASRS was investigated for Test No. 1. The different SCEAs and the FE predicted ASRS are illustrated in Figure 6.16 and Figure 6.17, respectively. Furthermore, the simulated values of MFs, MT and ASRS are listed in Table 6.7. As seen in Table 6.7, the predicted value of ASRS using the SCEA of 0º was the smallest, where MT had the lowest value. On the other hand, the SCEA of 10º provided the highest ASRS, where MT was the largest. As a result, the SCEA of 0º is recommended for turning of AA6061-T6 to obtain the smallest ASRS.

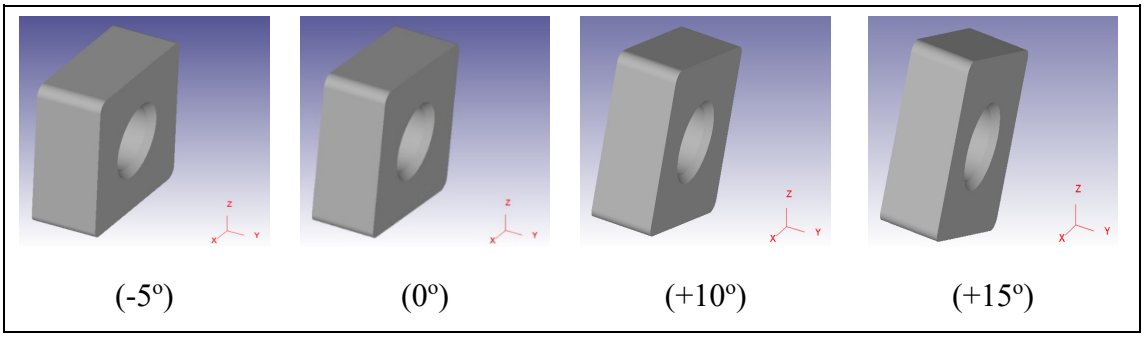

Figure 6.16 Different side cutting edge angles

Table 6.7 The FE predicted MFs, MT, and ASRS for different side cutting edge angles

SCEA $[deg]$	F_r $[N]$	F_f $[N]$	F_c $[N]$	T [°C]	ASRS $[MPa]$
-5	61	100	360	505	83
0	70	106	360	472	4
10	77	101	336	524	135
15	80	98	355	490	43

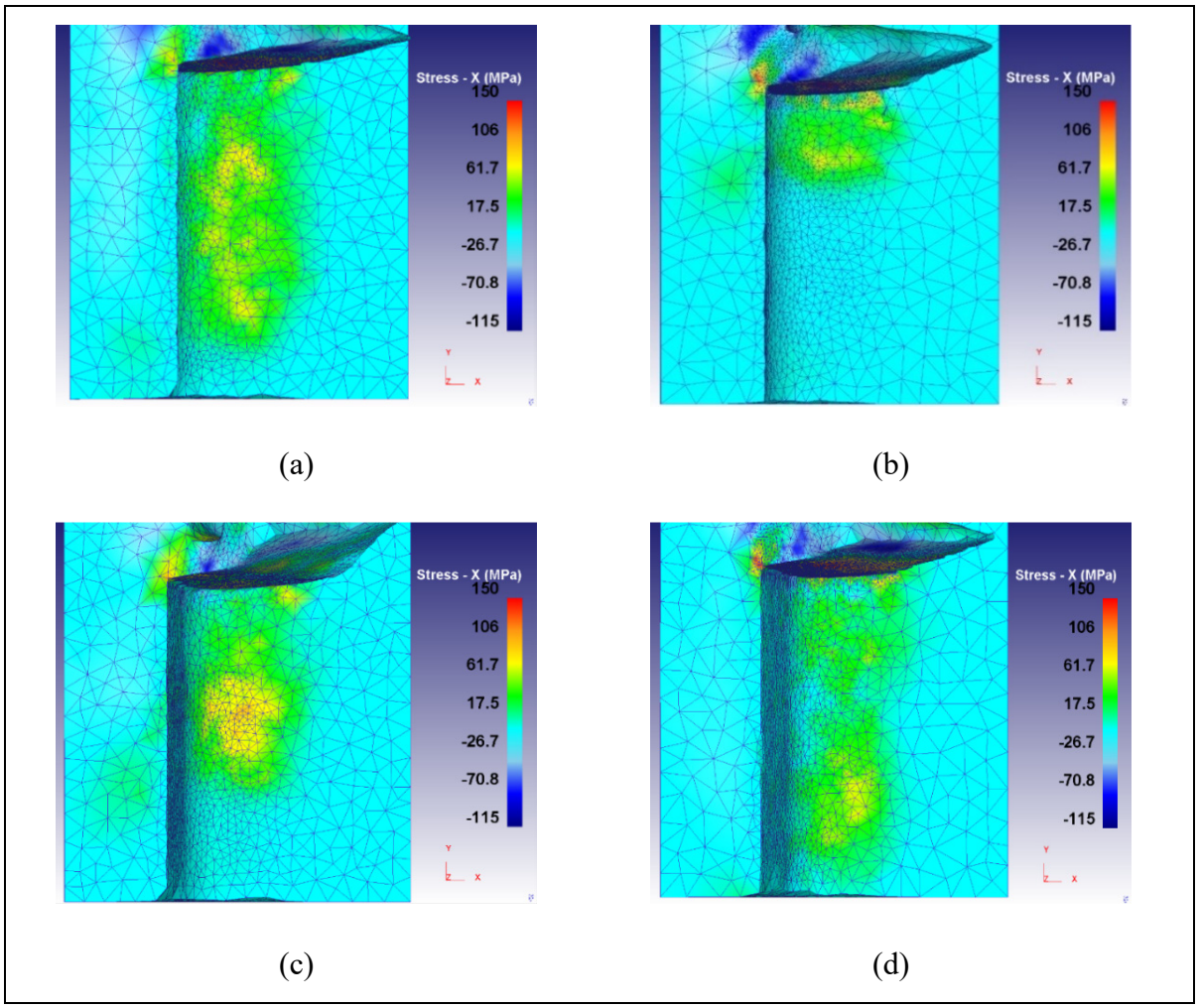

Figure 6.17 The distribution of simulated ASRS in the machined surface for Test No. 1 for the SCEA of (a) -5°, (b) 0°, (c) 10°, and (d) 15°

The FE predicted MT for the SCEA of 0° is shown in Figure 6.18. The deviation of SCEA from 0° to positive or negative values raised tool-chip contact length, frictional heat, and MT, and consequently, caused higher tensile ASRS (Umbert, 2018). It needs mentioning that MFs remained almost the same with the variation of SCEA.

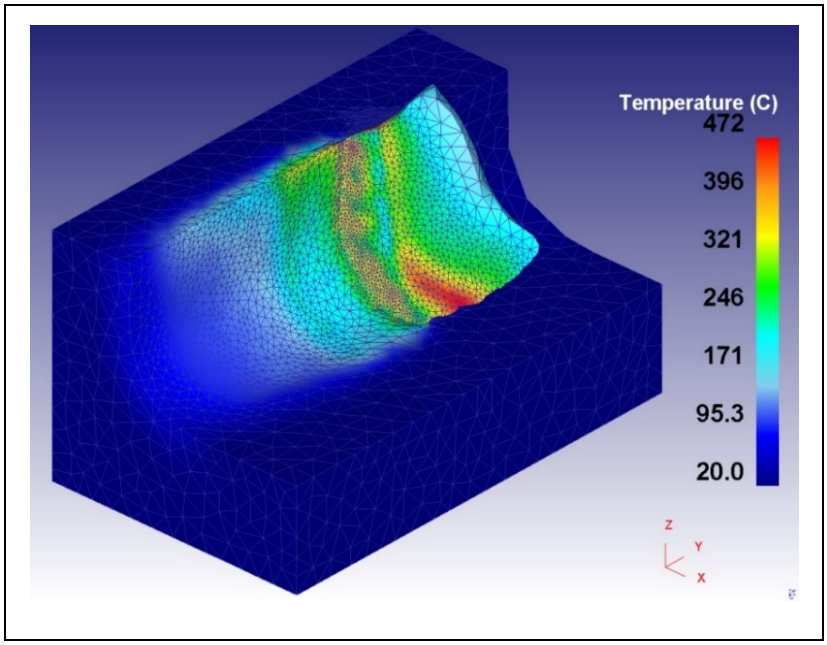

Figure 6.18 The FE predicted MT for the SCEA of 0º

6.5.3.3 Influence of back rake angle

The impact of BRA including 0º, -5º, -9º, and -15º on MFs, MT and ASRS was analyzed for Test No. 1. The different BRAs and the FE simulated ASRS are displayed in Figure 6.19 and Figure 6.20, respectively. In addition, the predicted values of MFs, MT and ASRS are given in Table 6.8. As observed in Table 6.8, the predicted ASRS increased with decreasing BRA from 0º to -15º.

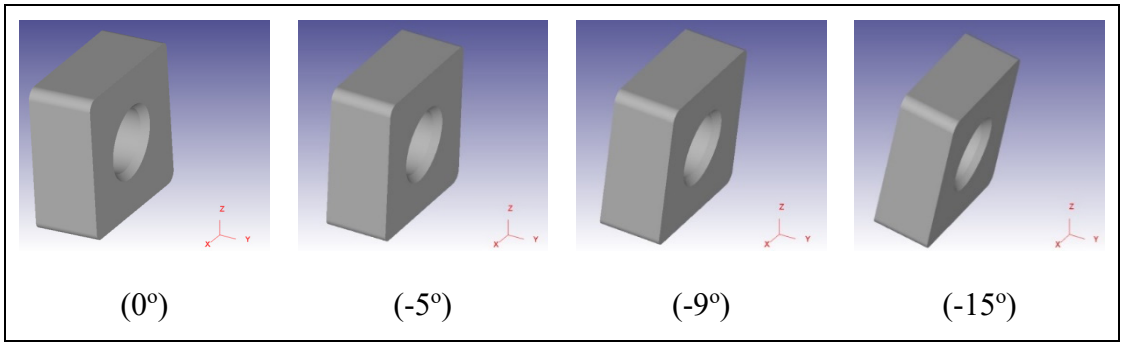

Figure 6.19 Different back rake angles

Table 6.8 The FE predicted MFs, MT, and ASRS for different BRAs

BRA $[deg]$	F_r $[N]$	F_f $[N]$	F_c $[N]$	T [°C]	ASRS $[MPa]$
0	70	85	403	446	54
-5	61	100	360	505	83
-9	93	115	386	507	90
-15	134	118	405	531	129

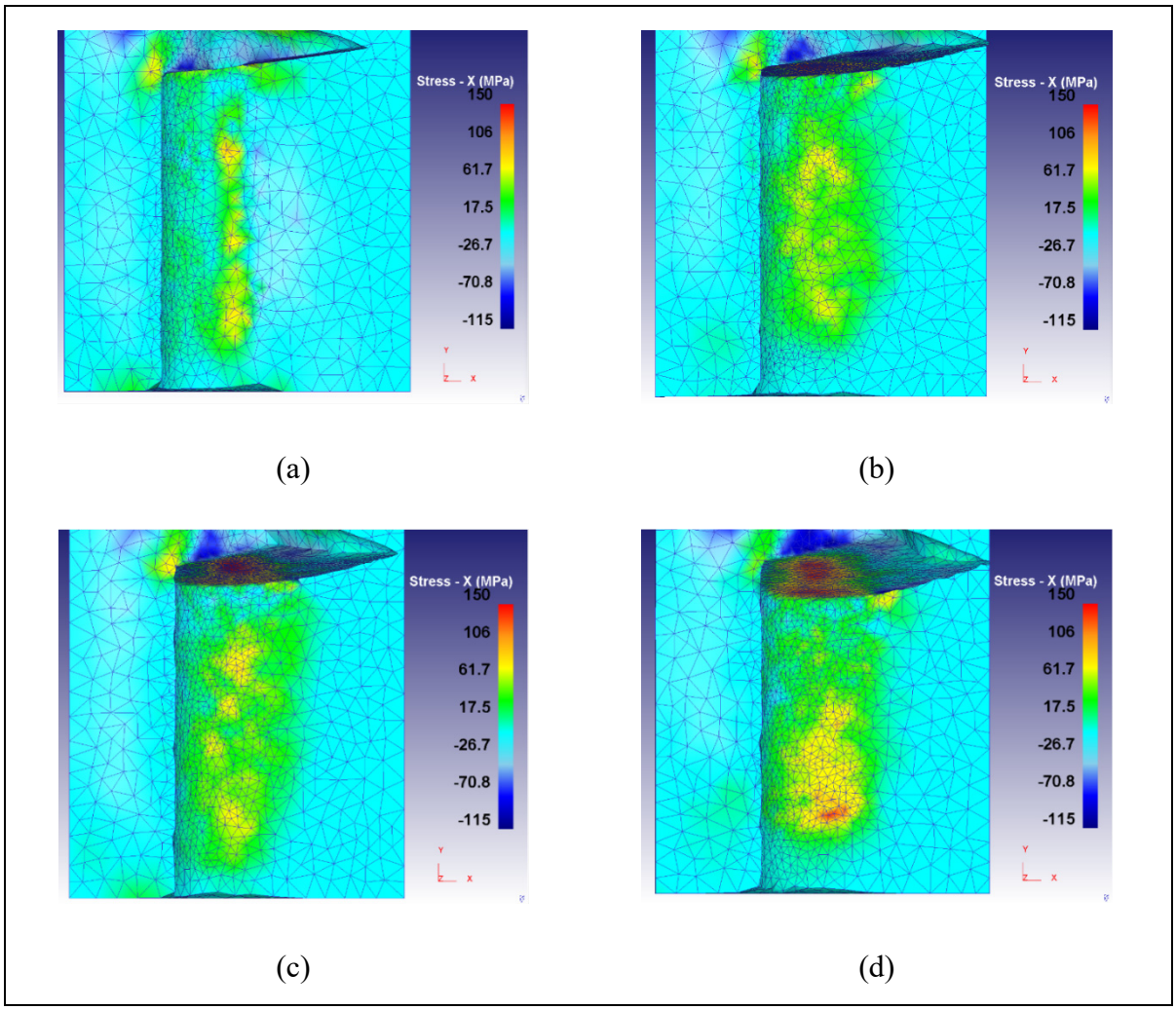

Figure 6.20 The distribution of simulated ASRS in the machined surface for Test No. 1 for the BRA of (a) 0º, (b) -5º, (c) -9º, and (d) -15º

The smallest value of ASRS was obtained for the BRA of 0º, where MT had the lowest magnitude and the resultant of MFs had a medium value. In contrast, the BRA of -15º provided the highest magnitude of ASRS, where both the resultant of MFs and MT had the largest magnitudes. Accordingly, the BRA of 0º is suggested. The distribution of FE simulated MT for the BRA of 0º is illustrated in Figure 6.21. It is known that a high negative rake angle causes high tool-chip contact pressure and friction, producing high frictional heat, large MT (Sadeghifar *et al.*, 2020; Daoud *et al.*, 2017) and ASRS. This is confirmed by (Giang *et al.*, 2016; Choi, 2017), where residual stresses increased with decreasing the rake angle in the negative direction.

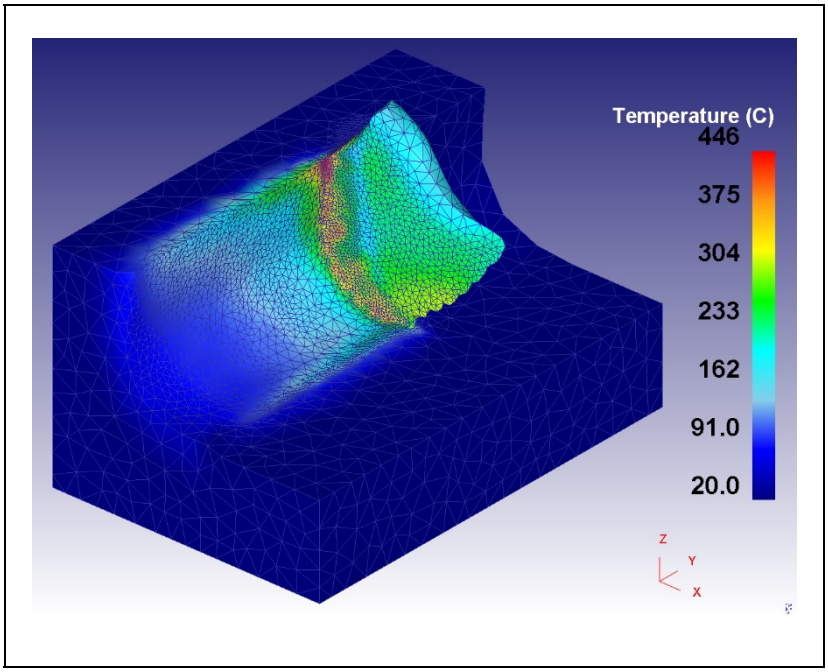

Figure 6.21 The FE predicted MT for the BRA of 0º

6.6 Summary and conclusion

In the present research work, the effects of turning environments and parameters on machining temperature, machining forces and axial surface residual stress induced by turning of AA6061-T6 were investigated. Turning environments include DRY, MQL, and WET modes, and turning parameters consist of both cutting conditions and tool geometry. The influences of

cutting speed, feed rate, depth of cut on ASRS and MFs were experimentally investigated, whereas the effects of tool nose radius, side cutting edge angle and back rake angle on MT, MFs and ASRS were analyzed using finite element modeling. The results demonstrated that ASRS increased with feed rate. For DRY, MQL, and WET modes, ASRS first remained almost unaffected between the depth of cut of 0.66 and 1.5 mm and then decreased from the depth of cut of 1.5 to 2.34 mm. ASRS increased with cutting speed in the range of 145 to 650 m/min for all the environments. For cutting speed between 650 to 1155 m/min, ASRS showed different variations for various environments. It was also found that turning using tools with the nose radius of 0.4 mm provided smaller ASRS. In addition, the change in SCEA from 0^o to positive or negative values led to higher tensile ASRS. Reducing BRA from 0^o to -15^o increased ASRS. Accordingly, SCEA and BRA equal to 0^o were suggested. The variation of ASRS was more sensitive to thermal effects than to mechanical effects.

CONTRIBUTIONS

The main contributions accomplished by the current research work can be summarized as follows:

- A 2D finite element model for the orthogonal turning of AA6061-T6 was developed to investigate the effect of tool edge radius and its interactions with cutting speed, feed rate, and rake angle on machining forces, temperature, and chip thickness.

- Surface integrity characteristics including residual stresses and surface roughness were measured to predict regression models and optimize the overall residual stresses and surface roughness parameters for DRY, MQL, and WET modes in turning of AA6061-T6.

- The most effective parameters consisting of cutting speed, feed rate, and depth of cut were identified for each turning environment and the best environment was proposed.

The effect of cutting conditions including cutting speed, feed rate, depth of cut on axial residual stress was experimentally investigated for three turning environments and the impact of tool geometry consisting of tool nose radius, side cutting edge angle, and back rake angle was numerically analyzed using developed 3D finite element model of WET turning.

CONCLUSION

The present research project was aimed at studying the effects of turning environment, cutting conditions, and tool geometry on machining characteristics and surface integrity. The turning environment includes DRY, minimum quantity lubrication (MQL), and WET modes, the cutting conditions consist of cutting speed, feed rate, and depth of cut, and tool geometry contain cutting edge and nose radii, back and side rake angles, and side cutting edge angle. In addition, machining characteristics include machining temperature, forces, and chip shape, and surface integrity consists of surface roughness and residual stresses.

In the first article, interactions between the cutting edge radius and cutting speed, feed rate, and rake angle were investigated and the influences of the aforementioned tool geometry and cutting conditions on machining characteristics in orthogonal cutting of AA6061-T6 were studied. A 2D FE model was developed to simulate the above interactions and was experimentally validated.

In the second article, the impacts of turning environments and parameters on surface integrity induced by turning of AA6061-T6 were investigated. The changes in surface roughness and residual stresses were captured for different turning parameters of cutting speed, feed rate, and depth of cut under DRY, MQL, and WET environments. Machining tests were carried out using a DoE based on CCD under the three turning environments. The most influential turning parameters were identified for each environment using ANOVA. RSM was used to predict effective regression models for each turning environment for the average arithmetic surface roughness, the height peak from the valley, the axial surface residual stress, and the hoop surface residual stress. Then, a multi-objective optimization study was performed to determine optimal turning parameters to improve surface integrity.

In the third article, the influences of turning environments and parameters on machining temperature, machining forces, and axial surface residual stresses induced by turning operation of AA6061-T6 were studied. Turning parameters consisted of cutting speed, feed rate, depth

of cut, tool nose radius, side cutting edge angle, and back rake angle. A 3D finite element model was developed and experimentally validated to simulate and predict MT, MFs, and ASRS for different turning environments and parameters.

In the light of the results obtained, the major conclusions are summarized as follows:

- The DRY orthogonal turning results showed that both cutting and feed forces were more sensitive to the cutting edge radius at low cutting speeds and a negative rake angle.

- It was found that the maximum cutting temperatures remained nearly constant with increasing the tool edge radius, while the average temperatures of the tool tip clearly increased.

- For various cutting speeds, rake angles, and feed rates, the variation of the chip thickness with the cutting edge radius was small.

- For DRY, MQL, and WET turning of AA6061-T6, the ANOVA results showed that feed rate and cutting speed were the most influential parameters on the surface integrity characteristics.

- Based on the ANOVA and multi-criteria optimization, DRY and MQL modes provided smaller surface roughness characteristics, while MQL and WET modes resulted in lower surface residual stresses and higher MRR.

- In terms of overall surface integrity characteristics and MRR in turning of AA6061-T6, MQL turning environment is proposed.

- Increasing feed rate caused a higher tensile ASRS while using tools with a nose radius of 0.4 mm led to lower ASRS.

- The deviation of SCEA from 0º to positive or negative values resulted in higher tensile ASRS. Moreover, ASRS increased with decreasing BRA from 0º to -15º.

RECOMMENDATIONS

Future research work related to this study will concentrate on the following aspects:

- 2D/3D Finite element modeling of both cutting process and residual stress steps can be carried out for other machining processes consisting of milling and drilling of other aluminum alloys

- Unconstrained and constrained multi-objective optimizations of residual stresses, surface roughness, cutting temperature, machining forces, and material removal rate can be conducted for milling, drilling, or micro-cutting of aluminum alloys.

- An experimental study may be conducted to measure machining forces for various cutting conditions so as to determine a more accurate frictional model to improve the frictional behavior at the tool-chip-workpiece interfaces.

- Residual stresses induced by milling and drilling processes under various environments including dry, MQL, wet, and cryogenic modes can be experimentally and numerically analyzed and modeled.

LIST OF REFERENCES

Abboud, E., Shi, B., Attia, H., Thomson, V., & Mebrahtu, Y. (2013). Finite element-based modeling of machining-induced residual stresses in Ti-6Al-4 V under finish turning conditions. Procedia Cirp, 8, 63-68.

Ajaja, J., Jomaa, W., Bocher, P., Chromik, R. R., Songmene, V., & Brochu, M. (2019). Hard turning multi-performance optimization for improving the surface integrity of 300M ultra-high strength steel. The International Journal of Advanced Manufacturing Technology, 104(1-4), 141-157.

Akram, S., Imran, H., Khan, M., Mubashar, A., Warsi, S., & Riaz, U. (2016, April). A numerical investigation and experimental validation on chip morphology of aluminum alloy 6061 during orthogonal machining. In 2016 Moratuwa Engineering Research Conference (MERCon) (pp. 331-336). IEEE.

Al-Zkeri, I., Rech, J., Altan, T., Hamdi, H., & Valiorgue, F. (2009). Optimization of the cutting edge geometry of coated carbide tools in dry turning of steels using a finite element analysis. Machining science and technology, 13(1), 36-51.

Arora, J. S. (2004). Introduction to optimum design. Elsevier.

Arrazola, P. J., & Ozel, T. (2008). Numerical modelling of 3D hard turning using arbitrary Lagrangian Eulerian finite element method. International Journal of Machining and Machinability of Materials, 4(1), 14-25.

Arunachalam, R. M., Mannan, M. A., & Spowage, A. C. (2004). Residual stress and surface roughness when facing age hardened Inconel 718 with CBN and ceramic cutting tools. International Journal of Machine Tools and Manufacture, 44(9), 879-887.

Attanasio, A., Ceretti, E., & Giardini, C. (2009). 3D FE modelling of superficial residual stresses in turning operations. Machining science and technology, 13(3), 317-337.

Barth, N. (2007). X-Ray Diffraction, University of California, Santa Barbara.

Deepak, D., & Rajendra, B. (2016). Optimization of Machining Parameters for Turning of Al6061 using Robust Design Principle to minimize the surface roughness. Procedia Technology, 24, 372-378.

Boulahmi, S. (2015). Étude expérimentale des effets de l'outil de coupe, des conditions d'usinage et de lubrification sur la qualité de surface et le comportement en traction des pièces en alliages d'alluminium, École de Technologie Supérieure, Canada, Master Dissertation.

Çakır, A., Yağmur, S., Kavak, N., Küçüktürk, G., & Şeker, U. (2016). The effect of minimum quantity lubrication under different parameters in the turning of AA7075 and AA2024 aluminium alloys. The International Journal of Advanced Manufacturing Technology, 84(9-12), 2515-2521.

Camposeco-Negrete, C. (2015). Optimization of cutting parameters using Response Surface Method for minimizing energy consumption and maximizing cutting quality in turning of AISI 6061 T6 aluminum. Journal of cleaner production, 91, 109-117.

Capello, E. (2005). Residual stresses in turning: Part I: Influence of process parameters. Journal of materials processing technology, 160(2), 221-228.

Capello, E. (2006). Residual stresses in turning: Part II. Influence of the machined material. Journal of Materials Processing Technology, 172(3), 319-326.

Chen, Y., Li, H., & Wang, J. (2015). Analytical modelling of cutting forces in near-orthogonal cutting of titanium alloy Ti6Al4V. Proceedings of the Institution of Mechanical Engineers, Part C: Journal of Mechanical Engineering Science, 229(6), 1122-1133.

Cheng, X., Zha, X., & Jiang, F. (2016). Optimizing the geometric parameters of cutting edge for rough machining Fe-Cr-Ni stainless steel. The International Journal of Advanced Manufacturing Technology, 85(1-4), 683-693.

Choi, Y. (2017). Influence of rake angle on surface integrity and fatigue performance of machined surfaces. International Journal of Fatigue, 94, 81-88.

Daoud, M. (2016). On the characterization of Johnson-Cook constants: Numerical and experimental study of high speed machining aerospace alloys. École de technologie supérieure, Canada, PhD Dissertation.

Daoud, M., Chatelain, J. F., & Bouzid, A. (2015a). Effect of rake angle on Johnson-Cook material constants and their impact on cutting process parameters of Al2024-T3 alloy machining simulation. The International Journal of Advanced Manufacturing Technology, 81(9-12), 1987-1997.

Daoud, M., Chatelain, J. F., & Bouzid, A. (2017). Effect of rake angle-based Johnson-Cook material constants on the prediction of residual stresses and temperatures induced in Al2024-T3 machining. International Journal of Mechanical Sciences, 122, 392-404.

Daoud, M., Jomaa, W., Chatelain, J. F., & Bouzid, A. (2015b). A machining-based methodology to identify material constitutive law for finite element simulation. The International Journal of Advanced Manufacturing Technology, 77(9-12), 2019-2033.

Daoud, M., Jomaa, W., Chatelain, J. F., Bouzid, A., & Songmene, V. (2014). Identification of material constitutive law constants using machining tests: a response surface

methodology based approach. WIT Transactions on The Built Environment, 137, 25-36.

Davim, J. P., Sreejith, P. S., & Silva, J. (2007). Turning of brasses using minimum quantity of lubricant (MQL) and flooded lubricant conditions. Materials and Manufacturing Processes, 22(1), 45-50.

Davoudinejad, A., Chiappini, E., Tirelli, S., Annoni, M., & Strano, M. (2015). Finite element simulation and validation of chip formation and cutting forces in dry and cryogenic cutting of Ti–6Al–4V. Procedia manufacturing, 1, 728-739.

DEFORM™ Software, Version 11.2, 2017.

Design-Expert User's Manual, Version 12, 2019.

Elsheikh, A. H., Ashham, M., Ali, M. K. A., Rashad, M., & Haiou, Z. (2019). Effect of cutting parameters on surface residual stresses in dry turning of AISI 1035 alloy. Journal of the Brazilian Society of Mechanical Sciences and Engineering, 41(8), 349.

Emamian, A. (2018). The effect of tool edge radius on cutting conditions based on updated Lagrangian formulation in finite element method. McMaster University, USA, Master Dissertation.

Filice, L., Micari, F., Rizzuti, S., & Umbrello, D. (2007). A critical analysis on the friction modelling in orthogonal machining. International Journal of Machine Tools and Manufacture, 47(3-4), 709-714.

Filice, L., Umbrello, D., Beccari, S., & Micari, F. (2006). On the FE codes capability for tool temperature calculation in machining processes. Journal of materials processing technology, 174(1-3), 286-292.

Garcia, R. F., Feix, E. C., Mendel, H. T., Gonzalez, A. R., & Souza, A. J. (2019). Optimization of cutting parameters for finish turning of 6082-T6 aluminum alloy under dry and RQL conditions. Journal of the Brazilian Society of Mechanical Sciences and Engineering, 41(8), 317.

Gianchandani, Y. B., & Crary, S. B. (1998). Parametric modeling of a microaccelerometer: comparing I-and D-optimal design of experiments for finite-element analysis. Journal of Microelectromechanical Systems, 7(2), 274-282.

Giang, L. H., Da, M. D., & Duc, P. M. (2016). Investigation of effects of tool geometry parameters on cutting forces, temperature and tool wear in turning using finite element method and Taguchi's technique. International Journal of Mechanical Engineering and Applications, 4(3), 109-114.

Guo, Y. B., & Liu, C. R. (2002). FEM analysis of mechanical state on sequentially machined surfaces.

Haddag, B., Atlati, S., Nouari, M., & Zenasni, M. (2015). Analysis of the heat transfer at the tool–workpiece interface in machining: determination of heat generation and heat transfer coefficients. Heat And Mass Transfer, 51(10), 1355-1370.

Horváth, R., & Drégelyi-Kiss, Á. (2015). Analysis of surface roughness of aluminum alloys fine turned: United phenomenological models and multi-performance optimization. Measurement, 65, 181-192.

Hua, J., Shivpuri, R., Cheng, X., Bedekar, V., Matsumoto, Y., Hashimoto, F., & Watkins, T. R. (2005). Effect of feed rate, workpiece hardness and cutting edge on subsurface residual stress in the hard turning of bearing steel using chamfer+ hone cutting edge geometry. Materials Science and Engineering: A, 394(1-2), 238-248.

Jafarian, F. (2019). 3D modeling of recrystallized layer depth and residual stress in dry machining of nickel-based alloy. Journal of the Brazilian Society of Mechanical Sciences and Engineering, 41(4), 198.

Jafarian, F., Amirabadi, H., & Sadri, J. (2015). Experimental measurement and optimization of tensile residual stress in turning process of Inconel718 superalloy. Measurement, 63, 1-10.

Jalali, A. (2013). Performance of Minimum Quantity Cooling (MQC) when turning aluminum alloy 6061-T6: surface roughness, tool temperature and aerosol emission. École de technologie supérieure, Canada, Master Dissertation.

Jamaludin, A. S. b. (2017). Studies on Minimum Quantity Lubrication in turning process-simplified and practical evaluation of lubricating and cooling effects of oil mist by means of Finite Element Method, Kanazawa University, Japan, PhD Dissertation.

Javidi, A., Rieger, U., & Eichlseder, W. (2008). The effect of machining on the surface integrity and fatigue life. International Journal of fatigue, 30(10-11), 2050-2055.

Javidikia, M., Sadeghifar, M., Songmene, V., & Jahazi, M. (2020a). Effect of turning environments and parameters on surface integrity of AA6061-T6: Experimental Analysis, Predictive Modelling and Multi-Criteria Optimization. The International Journal of Advanced Manufacturing Technology, 110(9), 2669-2683.

Javidikia, M., Sadeghifar, M., Songmene, V., & Jahazi, M. (2020b). On the impacts of tool geometry and cutting conditions in straight turning of aluminum alloys 6061-T6: an experimentally validated numerical study. The International Journal of Advanced Manufacturing Technology, 106(9), 4547-4565.

Jawahir, I. S., Brinksmeier, E., M'saoubi, R., Aspinwall, D. K., Outeiro, J. C., Meyer, D., & Jayal, A. D. (2011). Surface integrity in material removal processes: Recent advances. CIRP annals, 60(2), 603-626.

Jayaraman, P. (2014). Multi-response optimization of machining parameters of turning AA6063 T6 aluminium alloy using grey relational analysis in Taguchi method. Procedia Engineering, 97, 197-204.

Ji, X., Li, B., Zhang, X., & Liang, S. Y. (2014). The effects of minimum quantity lubrication (MQL) on machining force, temperature, and residual stress. International journal of precision engineering and manufacturing, 15(11), 2443-2451.

Jiang, H., He, L., Ren, Z., Shao, F., & Yuan, S. (2020). Prediction of residual stress in the process of turning high strength alloy steel by innovative coated carbide microgroove tools. The International Journal of Advanced Manufacturing Technology, 106(11), 4693-4705.

Jiang, L., & Wang, D. (2019). Finite-element-analysis of the effect of different wiper tool edge geometries during the hard turning of AISI 4340 steel. Simulation Modelling Practice and Theory, 94, 250-263.

Jomaa, W. (2015). Contributions to understanding the high speed machining effects on aeronautic part surface integrity. École de technologie supérieure, Canada, Doctoral Dissertation.

Jomaa, W., Mechri, O., Lévesque, J., Songmene, V., Bocher, P., & Gakwaya, A. (2017). Finite element simulation and analysis of serrated chip formation during high–speed machining of AA7075–T651 alloy. Journal of Manufacturing Processes, 26, 446-458.

Jomaa, W., Songmene, V., & Bocher, P. (2016). An hybrid approach based on machining and dynamic tests data for the identification of material constitutive equations. Journal of Materials Engineering and Performance, 25(3), 1010-1027.

Jumare, A. I., Abou-El-Hossein, K., Abdulkadir, L. N., & Liman, M. M. (2019). Predictive modeling and multiobjective optimization of diamond turning process of single-crystal silicon using RSM and desirability function approach. The International Journal of Advanced Manufacturing Technology, 103(9-12), 4205-4220.

Kamata, Y., & Obikawa, T. (2007). High speed MQL finish-turning of Inconel 718 with different coated tools. Journal of Materials Processing Technology, 192, 281-286.

Khan, A. R., Nisar, S., Shah, A., Khan, M. A., Khan, S., & Sheikh, M. (2017). Reducing residual stresses for optimal machining of Al-6061 (T-6) alloy through re-heating technique. Materials Science and Technology, 33(6), 731-737.

Khan, M. M. A., Mithu, M. A. H., & Dhar, N. R. (2009). Effects of minimum quantity lubrication on turning AISI 9310 alloy steel using vegetable oil-based cutting fluid. Journal of materials processing Technology, 209(15-16), 5573-5583.

Kirby, E. D., Zhang, Z., Chen, J. C., & Chen, J. (2006). Optimizing surface finish in a turning operation using the Taguchi parameter design method. The International Journal of

Korkmaz, M. E., & Günay, M. (2018). Finite element modelling of cutting forces and power consumption in turning of AISI 420 martensitic stainless steel. Arabian Journal for Science and Engineering, 43(9), 4863-4870.

Kosaraju, S., & Anne, V. G. (2013). Optimal machining conditions for turning Ti-6Al-4V using response surface methodology. Advances in Manufacturing, 1(4), 329-339.

Kouam, J., Songmene, V., Balazinski, M., & Hendrick, P. (2015). Effects of minimum quantity lubricating (MQL) conditions on machining of 7075-T6 aluminum alloy. The International Journal of Advanced Manufacturing Technology, 79(5-8), 1325-1334.

Leppert, T. (2011). Effect of cooling and lubrication conditions on surface topography and turning process of C45 steel. International Journal of Machine Tools and Manufacture, 51(2), 120-126.

Leppert, T., & Peng, R. L. (2012). Residual stresses in surface layer after dry and MQL turning of AISI 316L steel. Production Engineering, 6(4-5), 367-374.

Liu, L., Wu, M., Li, L., & Cheng, Y. (2020). FEM Simulation and Experiment of High-Pressure Cooling Effect on Cutting Force and Machined Surface Quality During Turning Inconel 718. Integrated Ferroelectrics, 206(1), 160-172.

Mabrouki, T., Girardin, F., Asad, M., & Rigal, J. F. (2008). Numerical and experimental study of dry cutting for an aeronautic aluminium alloy (A2024-T351). International Journal of Machine Tools and Manufacture, 48(11), 1187-1197.

Mali, R. A., Agrahari, M. D., & Gupta, T. V. K. (2019). FE based simulation and experimental validation of forces in dry turning of aluminium 7075. Materials Today: Proceedings.

Markopoulos, A. P. (2012). Finite element method in machining processes. Springer Science & Business Media.

Menezes, P. L., Avdeev, I. V., Lovell, M. R., & Higgs, C. F. (2014). An explicit finite element model to study the influence of rake angle and friction during orthogonal metal cutting. The International Journal of Advanced Manufacturing Technology, 73(5-8), 875-885.

Miguélez, M. H., Soldani, X., & Molinari, A. (2013). Analysis of adiabatic shear banding in orthogonal cutting of Ti alloy. International journal of mechanical sciences, 75, 212-222.

Mir, A., Luo, X., Cheng, K., & Cox, A. (2018). Investigation of influence of tool rake angle in single point diamond turning of silicon. The International Journal of Advanced Manufacturing Technology, 94(5-8), 2343-2355.

Montgomery, DC. (2006). Design and analysis of experiments. London: Wiley.

Moussa, N. B., Sidhom, H., & Braham, C. (2012). Numerical and experimental analysis of residual stress and plastic strain distributions in machined stainless steel. International Journal of Mechanical Sciences, 64(1), 82-93.

Navas, V. G., Gonzalo, O., & Bengoetxea, I. (2012). Effect of cutting parameters in the surface residual stresses generated by turning in AISI 4340 steel. International Journal of Machine Tools and Manufacture, 61, 48-57.

Outeiro, J. C., Pina, J. C., M'saoubi, R., Pusavec, F., & Jawahir, I. S. (2008). Analysis of residual stresses induced by dry turning of difficult-to-machine materials. CIRP annals, 57(1), 77-80.

Outeiro, J. C., Umbrello, D., & M'saoubi, R. (2006). Experimental and numerical modelling of the residual stresses induced in orthogonal cutting of AISI 316L steel. International Journal of Machine Tools and Manufacture, 46(14), 1786-1794.

Özel, T. (2009, January). Experimental and finite element investigations on the influence of tool edge radius in machining nickel-based alloy. In International Manufacturing Science and Engineering Conference (Vol. 43611, pp. 493-498).

Özel, T., & Ulutan, D. (2012). Prediction of machining induced residual stresses in turning of titanium and nickel based alloys with experiments and finite element simulations. CIRP annals, 61(1), 547-550.

Özel, T., & Zeren, E. (2007). Finite element modeling the influence of edge roundness on the stress and temperature fields induced by high-speed machining. The International Journal of Advanced Manufacturing Technology, 35(3-4), 255-267.

Patel, JP. (2018). Finite element studies of orthogonal machining of aluminum alloy AA2024-T351. The University of North Carolina at Charlotte, USA, Master Dissertation.

Pawade, R. S., Joshi, S. S., & Brahmankar, P. K. (2008). Effect of machining parameters and cutting edge geometry on surface integrity of high-speed turned Inconel 718. International Journal of Machine Tools and Manufacture, 48(1), 15-28.

Prevey, P. S. (1986). X-ray diffraction residual stress techniques. ASM International, ASM Handbook., 10, 380-392.

Priyadarshi, D., & Sharma, R. K. (2016). Optimization for turning of Al-6061-SiC-Gr hybrid nanocomposites using response surface methodologies. Materials and Manufacturing Processes, 31(10), 1342-1350.

Reddy, M. M., Kumar, M., & Shanmugam, K. (2018). Finite element analysis and modeling of temperature distribution in turning of titanium alloys. Metallurgical and Materials Engineering, 24(1), 59-69.

Roy, P., Sarangi, S. K., Ghosh, A., & Chattopadhyay, A. K. (2009). Machinability study of pure aluminium and Al–12% Si alloys against uncoated and coated carbide inserts. International Journal of Refractory Metals and Hard Materials, 27(3), 535-544.

Sadeghifar, M. (2017). Development of the analysis and optimization strategies for prediction of residual stresses induced by turning processes, Concordia University, Canada, PhD Dissertation.

Sadeghifar, M., Javidikia, M., Songmene, V., & Jahazi, M. (2020). Finite element simulation-based predictive regression modeling and optimum solution for grain size in machining of Ti6Al4V alloy: Influence of tool geometry and cutting conditions. Simulation Modelling Practice and Theory, 102141.

Sadeghifar, M., Sedaghati, R., Jomaa, W., & Songmene, V. (2018a). A comprehensive review of finite element modeling of orthogonal machining process: chip formation and surface integrity predictions. The International Journal of Advanced Manufacturing Technology, 96(9-12), 3747-3791.

Sadeghifar, M., Sedaghati, R., Jomaa, W., & Songmene, V. (2018b). Finite element analysis and response surface method for robust multi-performance optimization of radial turning of hard 300M steel. The International Journal of Advanced Manufacturing Technology, 94(5-8), 2457-2474.

Saravanakumar, A., Karthikeyan, S. C., & Dhamotharan, B. (2018). Optimization of CNC Turning Parameters on Aluminum Alloy 6063 using TaguchiRobust Design. Materials Today: Proceedings, 5(2), 8290-8298.

Sateesh, N., Satyanarayana, K., & Karthikeyan, R. (2018). Optimization of machining parameters in turning of Al6063A-T6 using Taguchi-Grey analysis. Materials Today: Proceedings, 5(9), 19374-19379.

Senevirathne, S. W. M. A. I., & Punchihewa, H. K. G. (2018). Reducing surface roughness by varying aerosol temperature with minimum quantity lubrication in machining AISI P20

and D2 steels. The International Journal of Advanced Manufacturing Technology, 94(1-4), 1009-1019.

Sreejith, P. S. (2008). Machining of 6061 aluminium alloy with MQL, dry and flooded lubricant conditions. Materials letters, 62(2), 276-278.

Suraratchai, M., Limido, J., Mabru, C., & Chieragatti, R. (2008). Modelling the influence of machined surface roughness on the fatigue life of aluminium alloy. International Journal of fatigue, 30(12), 2119-2126.

Swift, K. G., & Booker, J. D. (2013). Manufacturing process selection handbook. Butterworth-Heinemann.

Thakur, A., & Gangopadhyay, S. (2016). State-of-the-art in surface integrity in machining of nickel-based super alloys. International Journal of Machine Tools and Manufacture, 100, 25-54.

Touazine, H., Akab, J., Jahazi, M., Tahan, A., Jomaa, W., & Bocher, P. (2017). Modeling of the microstructure alteration induced by hard turning of Inconel 718. The International Journal of Advanced Manufacturing Technology, 93(9-12), 3705-3712.

Touazine, H., Chadha, K., Jahazi, M., & Bocher, P. (2019). Characterization of subsurface microstructural alterations induced by hard turning of Inconel 718. Journal of Materials Engineering and Performance, 28(11), 7016-7024.

Touazine, H., Jahazi, M., & Bocher, P. (2014, November). Influence of hard turning on microstructure evolution in the subsurface layers of Inconel 718. In ASME International Mechanical Engineering Congress and Exposition (Vol. 46438, p. V02AT02A018). American Society of Mechanical Engineers.

Ucun, İ., & Aslantas, K. (2011). Numerical simulation of orthogonal machining process using multilayer and single-layer coated tools. The International Journal of Advanced Manufacturing Technology, 54(9-12), 899-910.

Umbert, SM. (2018). Cutting forces in turning operations, Universitat Politècnica de Catalunya, Spain, Bachelor Dissertation.

Umbrello, D. (2008). Finite element simulation of conventional and high speed machining of Ti6Al4V alloy. Journal of materials processing technology, 196(1-3), 79-87.

Warsi, S. S., Agha, M. H., Ahmad, R., Jaffery, S. H. I., & Khan, M. (2019). Sustainable turning using multi-objective optimization: a study of Al 6061 T6 at high cutting speeds. The International Journal of Advanced Manufacturing Technology, 100(1-4), 843-855.

Wyen, C. F., & Wegener, K. (2010). Influence of cutting edge radius on cutting forces in machining titanium. CIRP annals, 59(1), 93-96.

Yen, Y. C., Jain, A., & Altan, T. (2004). A finite element analysis of orthogonal machining using different tool edge geometries. Journal of materials processing technology, 146(1), 72-81.

Zhuang, K., Weng, J., Zhu, D., & Ding, H. (2018). Analytical modeling and experimental validation of cutting forces considering edge effects and size effects with round chamfered ceramic tools. Journal of Manufacturing Science and Engineering, 140(8).